AN EVOLUTIONARY FUEL ASSEMBLY DESIGN FOR HIGH POWER DENSITY BWRs

by

Aydın Karahan

B.S. Nuclear Engineering
M.S. Nuclear Engineering
Hacettepe University, 2005

Submitted to the Department of Nuclear Science and Engineering
in partial fulfillment of the requirements for the degree of

MASTER OF SCIENCE IN NUCLEAR SCIENCE AND ENGINEERING

at the

MASSACHUSETTS INSTITUTE OF TECHNOLOGY

December 2006
[February 2007]

Author...
Department of Nuclear Science and Engineering
December 22, 2006

Certified by...
Jacopo Buongiorno
Assistant Professor of Nuclear Science and Engineering
Thesis Supervisor

Certified by...
Mujid S. Kazimi
Professor of Nuclear Engineering

Accepted by...
Jeffrey Coderre
Associate Professor of Nuclear Science and Engineering
Chairman, Committee for Graduate Studies

"Anybody who can't give an account of the past 3,000 years of intellectual history shouldn't be allowed to speak"

Johann Wolfgang von Goethe

AN EVOLUTIONARY FUEL ASSEMBLY DESIGN FOR HIGH POWER DENSITY BWRs

by
Aydın Karahan

Submitted to the Department of Nuclear Science and Engineering
on December 22, 2006 in partial fulfillment of the
requirements for the degree of
MASTER OF SCIENCE IN NUCLEAR SCIENCE AND ENGINEERING

ABSTRACT

An evolutionary BWR fuel assembly design was studied as a means to increase the power density of current and future BWR cores. The new assembly concept is based on replacing four traditional assemblies and large water gap regions with a single large assembly. The traditional BWR cylindrical UO_2-fuelled Zr-clad fuel pin design is retained, but the pins are arranged on a 22×22 square lattice. There are 384 fuel pins with 9.6 mm diameter within a large assembly. Twenty-five water rods with 27 mm diameter maintain the moderating power and accommodate as many finger-type control rods. The total number and positions of the control rod drive mechanisms are not changed, so existing BWRs can be retrofitted with the new fuel assembly. The technical characteristics of the large fuel assembly were evaluated through a systematic comparison with a traditional 9×9 fuel assembly. The pressure, inlet subcooling and average exit quality of the new core were kept equal to the reference values. Thus the power uprate is accommodated by an increase of the core mass flow rate. The findings are as follows:

- VIPRE subchannel analysis suggests that, due to its higher fuel to coolant heat transfer area and coolant flow area, the large assembly can operate at a power density 20% higher than the traditional assembly while maintaining the same margin to dryout.
- CASMO 2D neutronic analysis indicates that the large assembly can sustain an 18-month irradiation cycle (at uprated power) with 3-batch refueling, <5wt% enrichment with <60 MWD/kg average discharge burnup. Also, the void and fuel temperature reactivity coefficients are both negative and close to those of the traditional BWR core.
- The susceptibility of the large assembly core to thermalhydraulic/neutronic oscillations of the density-wave type was explored with an in-house code. It was found that, while

well within regulatory limits, the flow oscillation decay ratio of the large assembly core is higher than that of the traditional assembly core. The higher core wide decay ratio of the large assembly core is due to its somewhat higher (more negative) void reactivity coefficient.

- The pressure drop in the uprated core is 17 % higher than in the reference core, and the flow is 20% higher; therefore, larger pumps will be needed.
- FRAPCON analysis suggests that the thermo-mechanical performance (e.g., fuel temperature, fission gas release, hoop stress and strain, clad oxidation) of the fuel pins in the large assembly is similar to that of the reference assembly fuel pins.
- A conceptual mechanical design of the large fuel assembly and its supporting structure was developed. It was found that the water rods and lower tie plate can be used as the main structural element of the assembly, with horizontal support being provided by the top fuel guide plate and core plate assembly, and vertical support being provided by the fuel support duct, which also supports the finger-type control rods.

Thesis Supervisor: Jacopo Buongiorno
Title : Assistant Professor of Nuclear Science and Engineering
Thesis Reader : Mujid S. Kazimi
Title : TEPCO Professor of Nuclear Engineering

ACKNOWLEDGEMENTS

This work was supported by the Tokyo Electric Power Company.

I would first like to thank my advisor, Professor Jacopo Buongiorno, for his constant encouragement, guidance and numerous discussions.

It is author's great pleasure to thank Professor Mujid S. Kazimi and Dr. Pavel Hejzlar for valuable suggestions in every step of this work.

Special thanks to Professor Neil. E. Todreas, Dr. Edward E. Pilat and Dr. Shih-Ping Kao for their comments on this work.

Finally, I dedicate this work to my parents, Ali and Zekiye Karahan, for their guidance and moral support in every step of my life.

CONTENTS

LIST OF FIGURES

LIST OF TABLES

1. INTRODUCTION

1.1. BACKGROUND

Boiling water reactors (BWRs) in the United States have evolved from using 7×7 and 8×8 fuel arrays and 12-month cycles with batch average burnup of 30 GWd/ton Uranium, in the 1970s; to 9×9 fuel, up to 18-month cycle, batch average burnup of 45 GWd/ton Uranium in the 1980s; to 10×10 fuel, 18- to 24-month cycles, batch average burnup of 50 GWd/ton Uranium, in the 1990s. Table-1.1 shows the historical trend of commercial BWR fuel following its beginning at Big Rock Point and Humbolt Bay starting in 1963. In the 1980s and into the 1990s operating in a regulated power market with oversupply, utilities realized that to survive they had to reduce costs [1].

Table-1.1 Historical Trend of Commercial BWR Fuel in USA [1]

BWR Firsts	Start of Commercial Operation	Reactor	Fuel Load Date			Current Fuel	Cycle Energy (months)
			8 × 8	9 × 9	10 × 10		
First BWR/3 First large core	June 1970	Dresden 2	May 1975	April 1983	December 2001	10 × 10	24
First BWR/4	November 1972	Vermont Yankee	November 1974	May 1998	October 2002	10 × 10	18
First large core BWR/4	July 1974	Peach Bottom 2	May 1976	December 1992	October 2000	10 × 10	24
First C-Lattice BWR	June 1983	Susquehanna 1	June 1983	December 1987	October 1996	10 × 10	24
First BWR/5	January 1984	LaSalle 1	January 1984	November 1999	February 2002	10 × 10	24
Second BWR/5	December 1984	Columbia Generating Station	December 1984	June 1989	June 1996	10 × 10	24
First BWR/6	July 1985	Grand Gulf	July 1985	April 1989	May 2001	10 × 10	18

Increasing the power density of operating and/or future BWRs is an effective approach to improving their economic attractiveness. Because the capital cost of a typical BWR is of the order of 65 % of the total power cost, extracting more energy from an existing reactor or reducing the physical size of future BWRs may reduce total cost of nuclear power considerably. The key feature of the approach developed by GE for recent large (up to 20%) uprates at BWR stations is an increase of the average fuel assembly power with no increase in limiting fuel assembly power [2]. This is affected by advanced refueling patterns so as to operate with more fuel assemblies at high powers, but again without raising the limiting fuel assembly power. However, in this study we will explore modifications to the fuel assembly design that would allow for operation of the limiting fuel assembly at higher power. Clearly a combination of our approach and GE's could result in even higher power uprates.

In general there are several limitations on power density uprate of a BWR. The first constraint is set by the coolant dryout mechanism at the fuel surface. A long part of the two phase region of a typical BWR fuel operates in the annular flow regime. Dryout of the liquid film on any fuel rod will deteriorate heat transfer significantly. Therefore, the margin to dryout during steady state and anticipated transients should be preserved while uprating the power density.

The second constraint is set by thermalhydraulic instabilities. Among the different instability modes, density wave oscillation gains importance for BWR conditions. This instability mode is due to the interaction between the pressure drop-flow relations at the ends of a channel of a compressible fluid and is caused by the lag introduced due to the finite speed of propagation of kinematic density waves [3]. Flow oscillations are undesirable in two phase flow devices for several reasons. First, sustained flow oscillations may cause undesirable forced mechanical vibration of components. Second, flow oscillation may cause system control problems. This becomes of particular importance in BWRs where the coolant also acts as the moderator. Third, flow oscillations affect the local heat transfer characteristics and can cause a premature boiling crisis. The critical heat flux was thus found by Ruddick [4] to be reduced by 40 % when the flow was oscillating. Thus, new uprated designs need to be proven non-susceptible to such occurrence.

The third constraint is set by the neutronic performance of the fuel assembly. In order to maintain acceptable fuel utilization and fuel cycle economics, the power peaking factors and the refueling scheme should be close to current practices. Also, the reactivity coefficients, which depend on the enrichment and burnable poison distributions of a new fuel assembly, the number and position of the control rods, the axial variation of the coolant density and the fuel temperature play a critical role in the safety of a nuclear reactor and thus for a new BWR fuel assembly should not deviate dramatically from current BWR values.

1.2. OBJECTIVES

The overall objective of this work is to study the feasibility of increasing the core power density of existing and future Boiling Water Reactor designs by at least 20%, while maintaining the accepted safety margins for BWRs. This objective is pursued by re-arranging the geometry of the fuel assembly, but maintaining the traditional BWR cylindrical UO_2-fuelled Zr-clad fuel pin design.

1.3. THE LARGE ASSEMBLY CONCEPT

The occurrence of the boiling crisis (dryout) in the BWR fuel assembly can be delayed if the average heat flux to the coolant and/or coolant mass flux are decreased. Therefore, to “create” margin and enable higher power densities, it is necessary to increase the heat transfer area and decrease the mass flux. The first requirement drives the design towards smaller fuel pins, while the second drives it towards higher pitch-to-diameter ratios. Adjustment of fuel rod-to-duct and fuel rod-to-water rod clearances can also improve flow distribution and maximize dryout margin. Having performed a preliminary study of various fuel assembly geometries (also including hexagonal lattices), it has been shown that >20% power density uprate is achievable by using large square assemblies (see Appendix-E). The large assembly concept is based on replacing four traditional (e.g., 9×9) assemblies and large water gap regions with a single large assembly. Water rods within the assembly maintain the moderating power and accommodate finger type control rods (Figure-1.1). The total number and position of the control rod mechanisms are not changed, so existing BWRs can be retrofitted with this new fuel assembly concept. The geometry of the most promising large fuel assembly is summarized in Table-13.1.

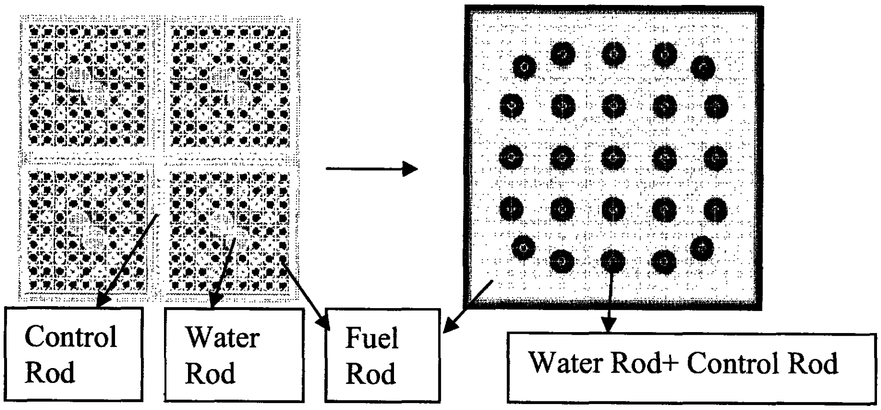

Figure 1.1: The Large Assembly Concept

1.4. SCOPE

Evaluation of the large assembly concept is conducted by systematic comparison of its thermalhydraulic and neutronic characteristics with those of a typical 9x9 fuel assembly design. The 9x9 assembly was selected as reference because of the availability of detailed technical information on its design.

Of great importance in the analysis is the selection of a suitable critical heat flux correlation that estimates the dryout margin with reasonable conservatism. A benchmark study against available dryout data has been performed and the EPRI-Columbia correlation was selected (Appendix A).

First, a subchannel analysis, including only the hot channel, coupled with 2D neutronics is performed to calculate the margin to dryout and determine the fuel composition (enrichment and burnable poison distribution), as a range of parameters (e.g., fuel pin diameter, pin pitch, inter-assembly gap) is explored. The outcome of this calculation is a set of values for such parameters that maximize the dryout margin; while evaluating the achievable discharge burnup and selecting a suitable refueling scheme.

Second, the susceptibility to mechanical vibrations of the reference and the most promising large assembly is assessed.

Third, a 3D neutronic-thermalhydraulic coupled model is used to assess the core void and fuel temperature reactivity coefficients.

Fourth, thermalhydraulic stability analyses are performed for single channel and in-phase stability. The single channel analysis is performed only for the hot channel of the reference and the new designed cores. On the other hand, in-phase stability analyses include the whole core, together with neutronic feedback. The calculated reactivity coefficients are used in the in-phase stability code to quantify the margin to coupled neutronic/thermalhydraulic oscillations at various operating conditions.

Next, the thermo-mechanical performance of the reference fuel rod and the large assembly fuel rod has been examined with FRAPCON-3.

Moreover, the conceptual mechanical design of the large fuel assembly is developed.

Finally, a comparison between the large fuel assembly and the Advance Boiling Water Reactor-2 assembly, which can accommodate 15 % higher power density with respect to a typical 9×9 assembly, is performed.

2. COMPUTATIONAL TOOLS

2.1. THERMALHYDRAULICS

2.1.1. VIPRE-01

VIPRE-01 [5] is a subchannel analysis code developed for general-purpose thermal-hydraulic analysis of LWR cores under normal operating conditions, operational transients, and accidents of moderate severity. The code predicts the three dimensional velocity, pressure, enthalpy and fuel temperature distributions for single and two phase flow in pressurized water reactor (PWR) and BWR cores. It solves the finite difference mixture equations for mass, energy and momentum conservation for an interconnected array of channels, assuming incompressible thermally expandable flow. Although the formulation is based on the mixture equations, empirical models are included for subcooled boiling and vapor/liquid slip in two phase flow.

The main purpose of using VIPRE-01 in this study is to calculate the dryout margin for the large and traditional fuel assemblies. Because VIPRE-01 is not suitable for multiple automatic runs with change of geometry, a script file, written in FORTRAN, automatically prepares the geometry section of the VIPRE input file, which greatly expedites the analysis of a large number of configurations.

2.1.2. STABILITY CODE

A code [6] developed at MIT estimates the susceptibility of BWRs to two-phase flow oscillations of the density wave type. The code is programmed in MATLAB. It is based on the linearization and Laplace-transformation of the mass, momentum and energy equations, along with the constitutive relations, and their analysis in the frequency domain. The main output of the code is the Decay Ratio (DR) for a perturbation, which indicates whether the oscillations grow in time (DR>1) or are dampened (DR<1). The code has the capabilities to model in-phase and out-of-phase oscillations in a single channel, whole core or different regions of the core with or without the neutronic feedback.

2.2. NEUTRONICS

2.2.1. CASMO-4

CASMO-4 [7] is a multi-group two dimensional transport code written in FORTRAN 77. As a deterministic lattice physics code, it is used for burnup calculations of light water reactor assemblies or pin cells. The code can represent geometries consisting of cylindrical fuel rods of varying compositions in a square or hexagonal lattice. Version 4 of CASMO uses the iterative, two dimensional characteristic solution KRAM, which solves the two dimensional Boltzmann transport equation in the fully heterogeneous lattice to give the neutron flux distribution.

2.2.2. MCNP-4C

MCNP [8] is a general purpose, generalized-geometry, continuous-energy, coupled neutron/photon/electron Monte Carlo N-Particle transport code developed at the Los Alamos National Laboratory (LANL). The model is very realistic (a theoretical experiment) as the spatial and energy treatments are in principle exact. Therefore, given sufficient neutron histories and appropriate cross-section libraries, MCNP can determine the neutron flux distribution very accurately.

The main disadvantage of MCNP compared to the deterministic codes is its demanding CPU requirements. For example, in order to obtain acceptable statistical errors, hours of MCNP calculations are usually needed whereas CASMO-4 takes only seconds.

2.2.3. ORIGEN-2

ORIGEN2.1 [9] is a one-group, point depletion and radioactive decay code developed at the Oak Ridge National Laboratory (ORNL). The code uses one-group cross-sections to calculate the time-dependent isotopic composition of the nuclear fuel. Typically, a total of 1700 nuclides are considered including 130 actinides, 850 fission products and 720 activation products. For accurate burnup calculations it is necessary to couple ORIGEN with an advanced physics code that adjusts the effective one-group cross-section library as the neutron spectrum changes with burnup.

2.2.4. MCODE

The MCNP-ORIGEN DEpletion Program (MCODE) was developed at MIT [10] and couples the continuous-energy Monte Carlo code, MCNP-4C, with the one group depletion code, ORIGEN2.1, to perform burnup calculations. MCNP provides the neutron flux and effective one-group cross-sections for different MCNP-defined regions. ORIGEN, in turn, undertakes multi-nuclide depletion calculations for each region and provides the material compositions to be used in the next MCNP step. The console program is written in ANSI C.

2.3. THERMO-MECHANICAL ANALYSIS OF THE FUEL

2.3.1. FRAPCON-3

FRAPCON steady state fuel rod modeling code was developed by the Pacific Northwest National Laboratory for use by the Nuclear Regulatory Commission in evaluation of Light Water Reactor (LWR) fuel rod behavior up to a burnup of 65 MWd/kg. The code models the fuel and cladding of a single fuel rod, and calculates temperature distributions, stress and strain, fission gas release, cladding oxidation, and other physical behavior as a function of an input power history and core conditions [11].

FRAPCON is a deterministic code that relies on a combination of theoretical and empirical constitutive relations to determine the properties of the fuel rod only at discrete time steps, where the step interval is generally days to weeks. The code's predictions have been benchmarked against experimental irradiation data, and it is expected to provide characteristic results for limited variations on traditional fuel rod design and operating conditions [12].

3. DESCRIPTION OF THE REFERENCE CORE

Establishment of a proper reference core design is necessary if the performance of the new design is to be evaluated. The reference core modeled in this research adopts its operating parameters from the General Electric BWR5 of Nine-Mile-Point Unit 2 (NMP2) [13], and the fuel assembly dimensions from a traditional 9×9 fuel assembly design. The 9x9 (vs. 10x10) assembly was selected as reference because of the availability of detailed technical information on its design. The plant parameters such as the core power, coolant flow rate, number of bundles, and system pressure are reported in Table-3.1, while the fuel assembly geometry and dimensions are displayed in Figure 3.1 and Table-3.2.

Table-3.1 Design Parameters of the Reference Core

System pressure, MPa	7.136
Core shroud radius, m	2.605
Number of fuel assemblies	764
Core mass flow rate, kg/s	13701.7
Core inlet temperature, °C	278.3
Core outlet temperature, °C	287.2
Core exit quality (%)	13.1
Core thermal power, MW_{th}	3323
Hot assembly power, kW_{th}	6304.5
Hot assembly exit quality (%)*	24.5
Hot assembly power peaking factor	1.45
Core flow bypass	14 %

* Hot channel exit quality obtained from a previous MIT full core simulation [14].

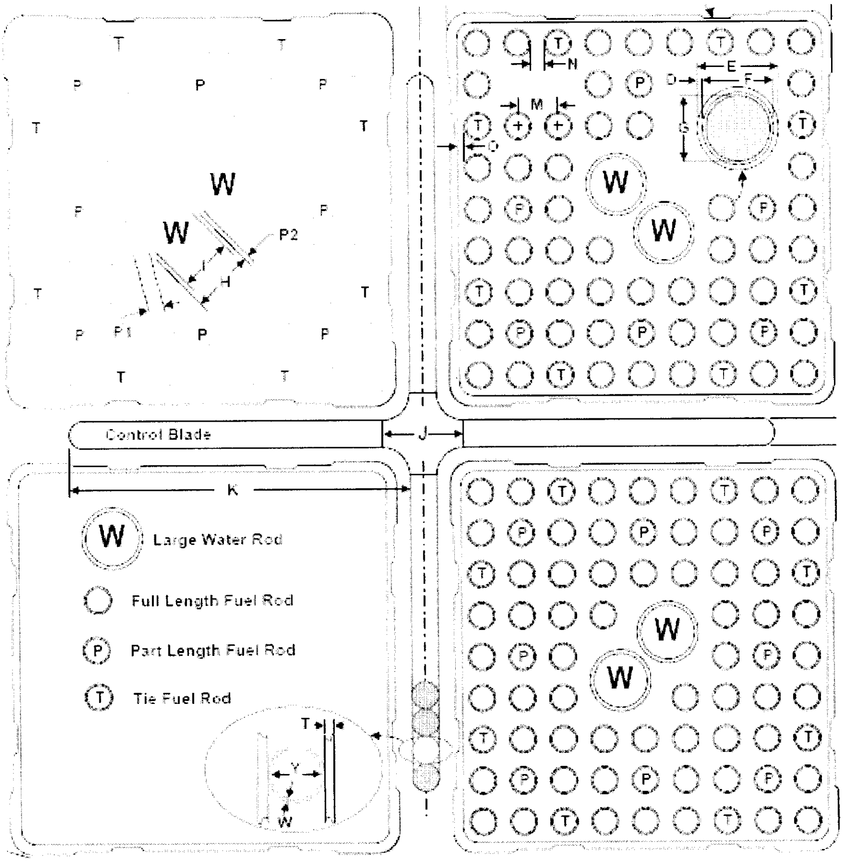

Figure 3.1: The Reference Assembly (Dimensions given in Table-3.2)

Table-3.2 Dimensions of the Reference Assembly shown in Figure-3.1

Parameters	**9×9 Assembly**
G (mm)	9.55
F (mm)	9.754
E (mm)	11.18
D (mm)	0.71
M (mm)	14.27
O (mm)	3.53
N (mm)	3.20
I (mm)	23.37
H (mm)	24.89
P1 (mm)	1.79
P2 (mm)	1.55
Y (mm)	4.78
W (mm)	0.64
T (mm)	0.76
J (mm)	40.13
K (mm)	131.29
Active Fuel rod height (mm)	3707.9
Total Fuel Rod height (mm)	4178.7
Part Length Rod Height (mm)	2436
Fuel Pins / Water Rods per Fuel Assembly	74/2
Number of Part Length Rods	8
Duct Thickness (mm)	2.54
Assembly Outer Dimension (mm)	137.54
Inter-Assembly Gap (mm)	14.86
Average Linear Power (kW/m)	16.46
Average Core Power Density (kW/L)	50.5
Approximate Assembly Weight (kg)	281

3.1. Pressure Loss Coefficients

The reference core inlet, exit and grid pressure loss coefficients [14] are given in Table-3.3. Also, these are equal for all assemblies. Two different orificing coefficients are used, consistent with the current BWR practice. All assemblies in the inner region of the core, which includes the hot channel and the nominal average channels, have the same orificing coefficient. On the other hand the peripheral channels have a higher orificing coefficient than the inner channels by an order of magnitude. As a result, more flow is diverted to the channels that generate more power.

Table-3.3 Pressure Loss Coefficients

Hot channel inlet orifice	21.089
Average power channel inlet orifice	21.089
Low power channel inlet orifice	182.049
Lower tie plate	9.4609
Upper tie plate	0.3751
Spacer loss coefficient/# of spacers	1.203/7

3.2. Power Profile

3.2.1. Assembly Power Peaking Factors

The VIPRE full core model includes four different assembly power peaking factors, as given in Table-3.4. Four assemblies have the maximum power peaking factor. The low power channels represent peripheral assemblies. Most assemblies have power peaking factor of unity, thus representing the average assemblies.

Table-3.4 Assembly Power Peaking Factors

Assembly Type	PPF	# of Assemblies
1	1.45	4
2	1.30	144
3	1.00	500
4	0.60	116

3.2.2. Reference Axial Power Profile:

The Beginning-Of-Life axial power distribution of Nine Mile Point Unit 2 [14] is used for all analyses in this research (except for the FRAPCON analysis) and is shown in Figure-3.2. This axial power profile is used to describe the full length rods. However, the fuel assemblies also have eight part-length rods, whose axial profile is shown in Figure-3.3. Partial length rods are also modeled with the reference power profile. However, beyond the active length, the power vanishes, as shown in Figure-3.3.

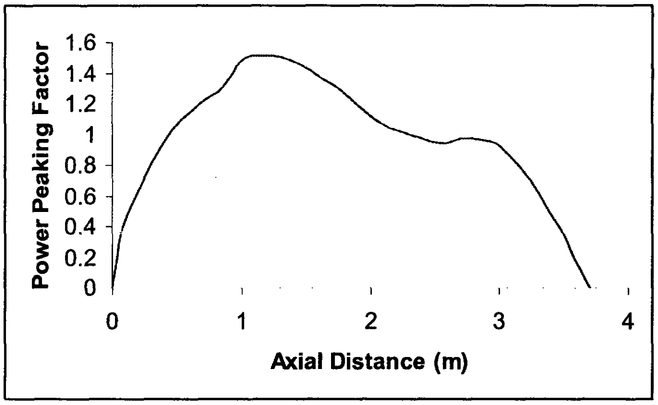

Figure-3.2: Reference Power Profile for Full Length Fuel Rods

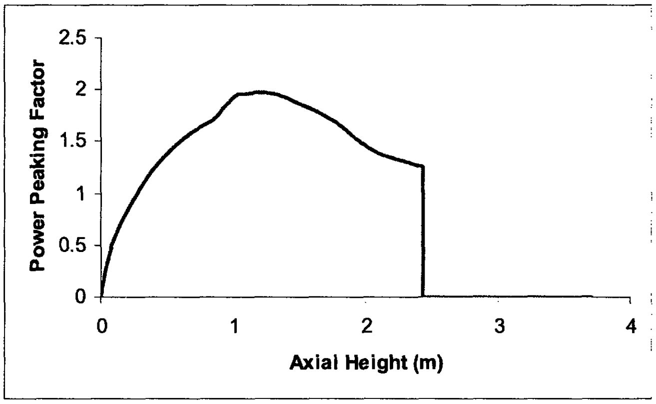

Figure-3.3: Reference Power Profile for Partial Length Fuel Rods (Normalization is performed over the full length)

3.2.3. Local Power Peaking Factors

Local Power Peaking Factors calculated by Fratoni at al. [15] are adopted as reference and shown in Figures 3.4 and 3.6 for the fresh fuel and the once-burned fuel, respectively. In Fratoni et al.'s work the power peaking factors are not normalized to the total rod number due to presence of eight part length rods. Because VIPRE-01 modeling requires normalization to the total rod number, renormalization is performed such that the sum of the power peaking factors is 74. The re-normalized power peaking factors are given in Figures 3.5 and 3.7. They are used in subchannel analysis of the reference assembly via VIPRE-01.

1.11	1.22	1.21	1.18	1.17	1.18	1.21	1.22	1.12
1.22	0.94	0.98	0.43	0.73	0.43	0.98	0.95	1.22
1.22	0.98	0.41	0.84	0.97	0.89	0.42	0.99	1.22
1.18	0.43	0.84	1.10			0.90	0.44	1.18
1.17	0.73	0.97				0.96	0.73	1.16
1.19	0.44	0.91			1.08	0.82	0.43	1.17
1.23	0.98	0.42	0.90	0.97	0.84	0.42	0.97	1.20
1.21	0.95	0.98	0.43	0.74	0.43	0.97	0.94	1.22
1.10	1.21	1.21	1.19	1.17	1.18	1.21	1.20	1.11

Figure 3.4: Original Fresh Assembly Power Peaking Factors

1.163	1.278	1.267	1.236	1.225	1.236	1.267	1.278	1.173
1.278	**0.985**	1.026	0.450	**0.765**	0.450	1.026	**0.995**	1.278
1.278	1.026	0.429	0.880	1.016	0.932	0.440	1.037	1.278
1.236	0.450	0.880	1.152	0.000	0.000	0.943	0.461	1.236
1.225	**0.761**	1.016	0.000	0.000	0.000	1.006	**0.765**	1.215
1.246	0.461	0.953	0.000	0.000	1.131	0.859	0.450	1.225
1.288	1.026	0.440	0.943	1.016	0.880	0.440	1.016	1.257
1.267	**0.995**	1.026	0.450	**0.775**	0.450	1.016	**0.985**	1.278
1.152	1.267	1.267	1.246	1.225	1.236	1.267	1.257	1.163

Figure 3.5: Fresh Assembly Power Peaking Factors Normalized to Total Rod Number (Bold PPFs represent part length rods)

0.95	1.00	1.04	1.06	1.06	1.07	1.05	1.02	0.96
1.00	0.91	0.97	0.77	0.86	0.79	0.98	0.91	1.02
1.05	0.97	0.73	0.89	0.98	0.97	0.77	0.98	1.06
1.07	0.77	0.89	1.07			0.97	0.78	1.08
1.05	0.86	0.97				0.99	0.86	1.06
1.07	0.78	0.96			1.08	0.89	0.77	1.07
1.05	0.99	0.77	0.96	0.98	0.90	0.73	0.97	1.05
1.01	0.92	0.98	0.79	0.86	0.77	0.97	0.91	1.01
0.96	1.01	1.05	1.08	1.05	1.07	1.04	1.01	0.96

Figure 3.6: Original Once Burned (9.38 MWd/kg) Assembly Power Peaking Factors

0.994	1.047	1.088	1.109	1.109	1.120	1.099	1.067	1.005
1.047	**0.952**	1.015	0.806	**0.900**	0.827	1.026	**0.952**	1.067
1.099	1.015	0.764	0.931	1.026	1.015	0.806	1.026	1.110
1.120	0.806	0.931	1.120	0.000	0.000	1.015	0.816	1.130
1.099	**0.900**	1.015	0.000	0.000	0.000	1.036	**0.900**	1.109
1.120	0.816	1.005	0.000	0.000	1.130	0.931	0.806	1.120
1.099	1.036	0.806	1.005	1.026	0.942	0.764	1.015	1.099
1.057	**0.963**	1.026	0.827	**0.900**	0.806	1.015	**0.952**	1.057
1.005	1.057	1.099	1.130	1.099	1.120	1.088	1.057	1.005

Figure 3.7: Once Burned (9.38 MWd/kg) Assembly Power Peaking Factors Normalized to Total Rod Number (Bold PPFs represents part length rods)

4. METHODOLOGY

The feasibility of power uprate in the large assembly concept is examined by using a coupled code thermalhydraulic and neutronic analysis. Thermalhydraulics include subchannel and stability analysis; whereas, neutronics include 2D and 3D transport calculations with fuel depletion. In all these analyses the system pressure, inlet subcooling, exit quality (and thus power-to-flow ratio), bypass flow fraction and heavy metal inventory in the large assembly core are fixed and are the same as in the reference core. Thus, the power uprate is accommodated by an increase in core mass flow rate.

4.1. The Description of the Algorithm

Figure-4.2 shows the flow chart of the analysis.

1- The script file generates candidate geometries, preserving heavy metal inventory of the reference core. Diameter of the fuel pin, number of water rods, clearance between fuel rods and water rods and fuel rods and assembly duct, thickness of the inter-assembly gap and number of part length rods are the main variables. For each case, the script files generate the corresponding geometry data required for VIPRE-01.

2- The corresponding assembly geometry is also modeled in CASMO-4. As a result of 2D neutronics optimization study including enrichment and burnable poison variation, the local power peaking factors (PPFs) are obtained. These are used together with the core-wide radial factor and the axial factor as needed for the thermal margin analysis.

3- Because 2D neutronics is unable to account for part-length rods, the PPFs are modified to account for part length rods according to the methodology described in Appendix-C.

4- The subchannel analysis provides the MCHFR for fresh as well as once burned states. This step requires an iterative procedure between CASMO-

4 and VIPRE-01 to obtain the optimum distribution of enrichment and poison to maximize the dryout margin.

5- If the candidate geometry does not allow for at least 20 % power uprate, it is rejected and other values of the geometric parameters are explored.

6- Having obtained a satisfactory dryout margin for fresh as well as once burned assemblies, the compositions of the once, twice and thrice burned fuel assemblies are provided by the 3D neutronic analysis with MCNP and ORIGEN. MCODE provides the coupling.

7- These compositions are used to create the MCNP core model to verify the core is critical at End of Cycle.

8- The Beginning of Cycle MCNP core model is used to select the control rod diameter that gives 1% reactivity shutdown margin at Cold Zero Power and with all control rods fully inserted.

9- The Beginning of Cycle model is also used at hot full power to obtain the fuel temperature and void reactivity coefficients.

10- The in-phase stability analysis is performed. The flow in each channel and orificing of peripheral channel are calculated with VIPRE. Using the reactivity coefficients calculated via 3D neutronics, the oscillation decay ratio is obtained.

12- The configuration with the lowest decay ratio is reported.

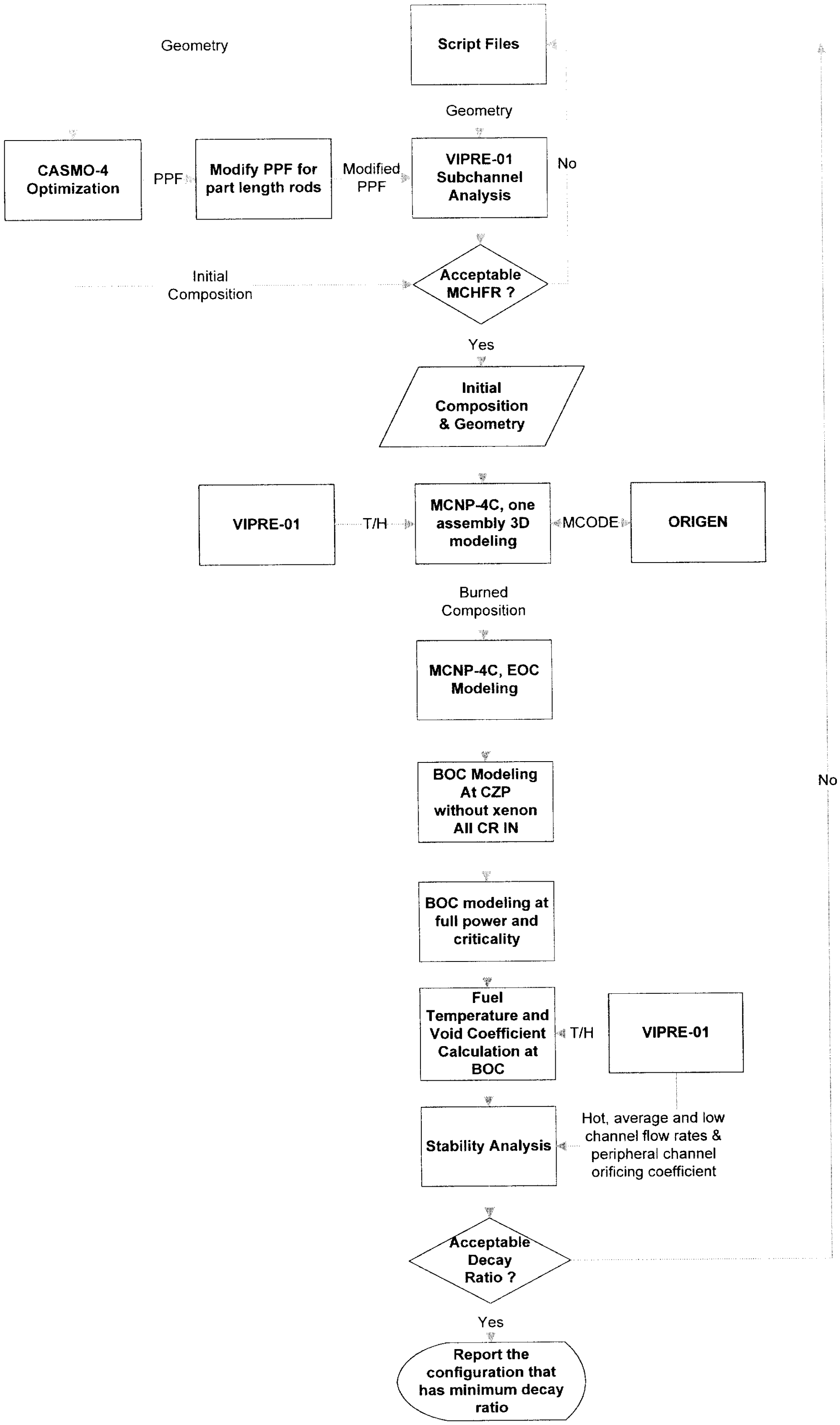

Figure-4.1: Flow Chart of the Optimization Study

5. SUBCHANNEL ANALYSIS

The main objective of the subchannel analysis is to identify a set of geometric parameters defining a large assembly design with dryout margin higher than or equal to the reference case, while operating at ≥20% higher power density.

5.1. Methodology

The subchannel analysis is the fundamental method to estimate the flow distribution within the assembly. Because the subchannel analysis requires input of the local power distribution, the local power peaking factors (PPFs) for the large assembly designs have been calculated via CASMO 2D neutronics. Having obtained the flow distribution, VIPRE-01 uses a dryout correlation to estimate the minimum critical heat flux ratio or margin to dryout. Since there are many candidate correlations, a benchmark study against available dryout data was performed, to select a proper dryout correlation (see Appendix-A). As a result, the EPRI-Columbia correlation was adopted to calculate the minimum critical heat flux ratio. A subchannel analysis with PPFs related to fresh as well as once burned fuel composition at full power is performed via VIPRE-01. Although the maximum PPF for fresh composition is far higher than the PPF in once burned composition, the reactivity (and thus power) of the once burned assembly can be considerably higher than that of the fresh assembly, due to depletion of the burnable poisons. To be conservative, the dryout margin in both situations is evaluated.

The following considerations are important in the optimization of the fuel assembly geometric parameters to maximize the dryout margin. First, inappropriate clearance between water rods and fuel rods and between assembly duct and fuel rods can divert a significant amount of flow to these regions and cause a loss of margin. Second, part length rods increase the hydraulic diameter of their corresponding subchannels in the upper part of the fuel assembly, so their use in regions of high PPFs can ensure high flow (by reducing friction) which results in lower flow quality; thus, the margin to dryout increases (a justification is given in Appendix-F). Third, an increase in the fuel rod heat transfer area provides a direct gain in dryout margin, because it lowers the heat flux. This parameter drives the design to lower pin diameters. However, there are limits to how small can the solid pins be while still maintaining enough rigidity to resist vibrations, and avoiding the penalty of corrosion of thinner cladding. In this study, designs that have pin diameters lower than a typical PWR fuel pin have been rejected. Fourth, the effect of mass flux is also considerable on dryout margin. Higher flow velocities may accelerate liquid entrainment in annular flow, thus, accelerating dryout. Achieving a power uprate while keeping the mass flux, the power to flow ratio and the inlet subcooling approximately constant, drives the design towards higher flow areas. In the large fuel assembly design the elimination of four inter-assembly gaps makes room available for increasing the flow area within the assembly. On the other hand, the higher flow area results in higher (more negative) void reactivity coefficient, which reduces the thermalhydraulic stability margin

Assumptions

1- 90 axial nodes

2- Uniform heat generation within fuel rod radially and azimuthally.

3- Part length rods are modeled by modifying their axial power profile (Figure-3.3). Moreover, the corresponding subchannel area, wetted perimeter and gap are modified in the upper section of the assembly to simulate the upper part of part length rods.

4- Adiabatic boundary condition is applied to the water rod surface and assembly duct. Thus, heat transfer into the by-pass flow channels is not modeled.

Correlations

1- Subcooled void fraction: EPRI drift flux model

2- Bulk void fraction: EPRI drift flux model

3- Two Phase friction multiplier: Columbia/EPRI correlation

4- Turbulent friction factor correlation for bundles: $f = 0.15139\,\mathrm{Re}^{-0.18}$ (Cheng and Todreas)

5- Single phase forced convection correlation: Dittus-Boelter

6- Heat transfer correlation for subcooled and saturated boiling: Chen

7- Critical Heat Flux Correlation: EPRI-Columbia (Cold Wall and spacer correction factors are accounted for; the corresponding spacer loss coefficient is 1.203. Non-uniform axial flux factor is not used as recommended in VIPRE-01 Manual [5])

8- Turbulent Mixing Flow Correlation has the following form: $W'_{ij} = \beta \times s_{ij} \times G$ (see Appendix-F)

$\beta = \dfrac{W'_{ij}}{(s_{ij} \times G)}$ $\beta \cong 0.005$ (For the Central Subchannels)

W'_{ij} : Flow per unit length between subchannel i & j.

G : Axial Mass flux

s_{ij} : Gap between fuel rods

5.2. Reference Assembly

The active flow area of the reference assembly is divided into 98 subchannels as shown in Figure-5.1.

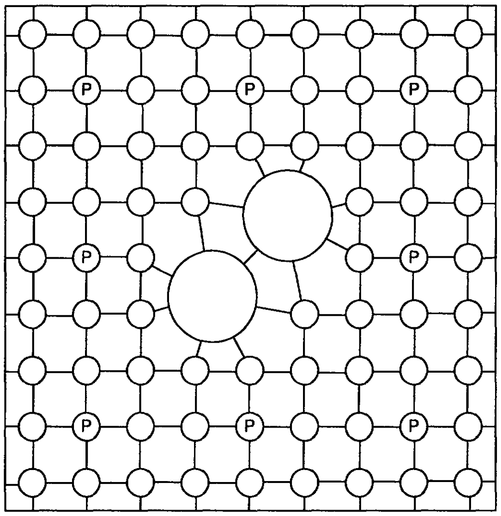

Figure-5.1: VIPRE-01 Model of the Reference Assembly (The partial length rods are denoted by "P")

The subchannel analysis for the hottest channel of the reference core is performed via VIPRE-01. The Minimum Critical Heat Flux Ratio (MCHFR) is calculated by using the reference power peaking factors for fresh (Figure-3.5) as well as once burned composition (Figure-3.7).

The MCHFR subchannel and the corresponding axial location within the heated length are given in Figure-5.2. The MCHFR values are given in Table-5.1. These values are used as constraints in the optimization study for the large assembly concept.

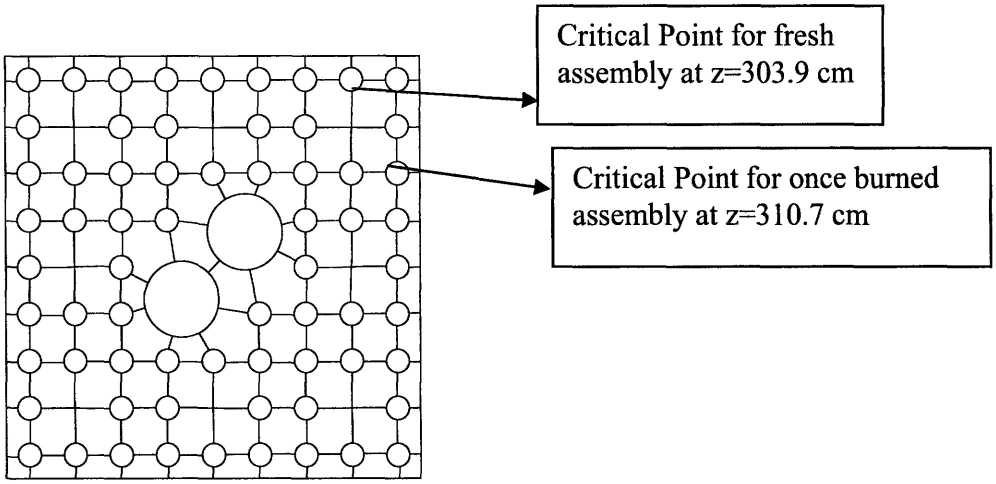

Figure-5.2: Locations that have the lowest dryout margin for fresh and once burned reference assembly

Table-5.1: Minimum Critical Heat Flux Ratio of the Fresh and Once Burned Assemblies

Assembly Type	MCHFR
Fresh Assembly	1.23
Once Burned Assembly	1.35

The dryout calculation for both states (fresh and once burned) is performed for the same assembly power, and under this assumption the fresh assembly has the lowest dryout margin. However, the neutronic calculations show that the reactivity of the once burned assembly is higher than that of the fresh assembly at the beginning of cycle. So its power should also be higher. Therefore, to be conservative, it is assumed that, when switching to the large assembly design, the dryout margin has to be maintained for both states.

5.3. Large Assembly Optimization Study

The optimization study is performed with coupled thermalhydraulics and neutronics. The following features are searched:

1- 20 % power uprate
2- Dryout margin should be greater than or equal to the reference case
3- Stability margin should be maximized

5.3.1. Generation of the Candidate Assembly Geometries

In this study, script files have been used to generate different assembly geometries efficiently. The heavy metal inventory of the reference core is preserved. The geometry parameters are varied in the ranges shown in Table 5.2. Note that the combinations resulting in a difference in H/HM between the reference and the new designs of more that ±5 % are rejected.

Table-5.2: Main Variables for the Optimization and Their Range

Variable	**Minimum**	**Maximum**
Diameter of the fuel pin (mm)	9.5	11.0
Number of water rods	16	36
Clearance between water rods & Fuel rods (mm)	1.0	4.0
Clearance between fuel rods and assembly duct (mm)	1.0	4.0
Number of partial length rods	0	48
Inter-assembly gap thickness (mm)	5	15

5.3.2. Modeling Details

Modeling is restricted only to the hottest assembly. The following parameters are held the same as in the reference case:

1- Power to flow ratio
2- Axial power profile
3- Inlet subcooling
4- Hot channel exit quality
5- Hot channel inlet orificing, tie plates and spacer loss coefficients
6- Fraction of the total flow bypassed (It is assumed that the lower and upper core plates can be designed to maintain the bypass flow at a desired value)

5.3.3. The Most Promising Large Assembly

1/8th of the most promising large assembly is divided into 72 subchannels as per Figure-5.3.

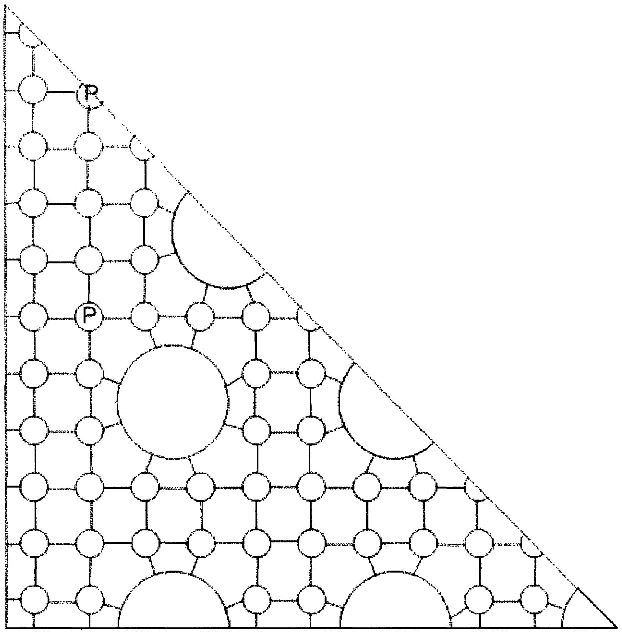

Figure-5.3: VIPRE-01 Model of the Large Assembly ("P" specifies the part length rods)

The most promising large assembly has a 22×22 array. Twenty-five water rods are included within the assembly. Moreover, twelve fuel rods are part length rods. The detailed geometry is given in Table-13.1.

The MCHFR subchannel and the corresponding axial locations within the heated length of the most promising large assembly are given in Figure-5.4.

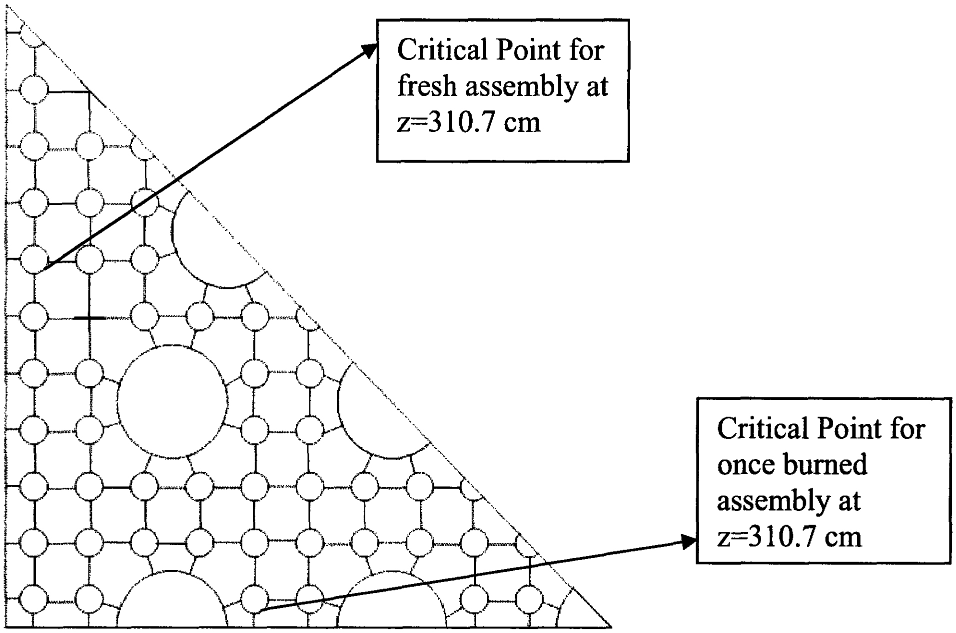

Figure-5.4: Locations that have the lowest dryout margin for fresh and once burned large assembly

Table-5.3: Minimum Critical Heat Flux Ratio of the Fresh and Once Burned Large Assembly at 20 % Power Uprate

Assembly Type	MCHFR
Fresh Assembly	1.23
Once Burned Assembly	1.35

As can be seen in Table-5.3, this large assembly configuration has dryout margins identical to those of the reference assembly. This is not a coincidence. The new design was optimized to maintain the same margins of the reference design, but at 20% higher power.

6. THERMALHYDRAULIC AND COUPLED STABILITY ANALYSIS

The single channel and core-wide in-phase stability analyses are performed for the reference and large assembly designs. The corresponding perturbation decay ratio of the reference and the most promising large assembly is reported.

6.1. Single Channel Thermalhydraulic Stability Analysis

During the single channel flow stability, only one channel oscillates while the bulk flow remains at steady state. Therefore, a constant pressure drop boundary condition can be imposed on that single channel as shown in Figure-6.1.

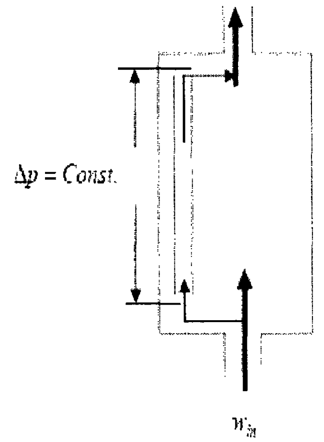

Figure-6.1 Single Channel Illustration (w_{in} : Mass flow rate)

Due to the small fraction of the single channel flow compared to that of the whole reactor core, the neutronic feedback due to the flow fluctuation of a single channel will not affect the whole core neutronic properties much. Therefore, a single channel can oscillate on its own without the neutronic feedback. Due to this reason, the single channel stability analysis has not been coupled with neutronics.

6.1.2. Correlations and Models for the Single Channel Stability Analysis

1- Bulk Void/Quality correlation: Homogeneous Equilibrium Model- Note that HEM was found to yield conservative results for the stability analysis [6]

2- Two phase Friction Multiplier is assumed to be two times Homogenous Equilibrium Model : $\phi_{lo}^{2} = 2\frac{\rho_l}{\rho_m}$

ρ_l : Water density at boiling boundary

ρ_m : Mixture density in two phase region

The factor "2" in the two phase friction multiplier is suggested by both Ishii in 1971 and Saha in1974 for high exit qualities and it is referenced in Ref. [6].

3- Single phase forced convection correlation: Dittus-Boelter

4- Heat transfer correlation for the two phase region: Thom.

The heat transfer correlations are used to calculate the fuel temperature, as the fuel thermal inertia is included in the model.

6.1.3. Main Approximations and Modifications to the Original Stability Code

1- Non-uniform power profile capability is now included (see Appendix-B)

2- Spacer, orificing, upper and lower tie plate loss coefficients are included (see Appendix-B)

3- Part length rods are treated as full length rods (this adds heat and friction near the top; thus, it is a conservative approach.)

6.1.4. Single Channel Stability Results

Single channel stability analyses are performed for the hot channel with the reference power profile (Figure-3.2). Table-6.1 shows the hot channel power, flow and decay ratio for the reference and the most promising large assembly cores. Note that power-to-flow ratio, inlet subcooling and pressure loss coefficients of the most promising large assembly are the same as the reference design. Furthermore, the pressure drop of these two designs is similar (Table-13.1). As can be seen in Table-6.1, the resulting decay ratio of the large assembly is identical to that of the reference design.

Table-6.1 Single Channel Stability Analyses for the Hot Channel

Reactor Type	Power (MWt)	Flow (kg/s)	Core Inlet Temperature (Celsius)	Decay Ratio
Reference	6.306	15.286	278.3	0.12
Large Assembly	30.27	73.374	278.3	0.12

6.2. In-phase Stability Analysis

Core wide nuclear/thermalhydraulic coupled stability analysis will be performed for the reference design and the new designs. During an in-phase oscillation, the whole core oscillates in the same phase and the fundamental mode of neutronic dynamics is excited. The density wave transits in a closed loop (Figure-6.2). The controlled boundary condition for this loop is that the sum of the pressure drop oscillations for all components along the path is zero.

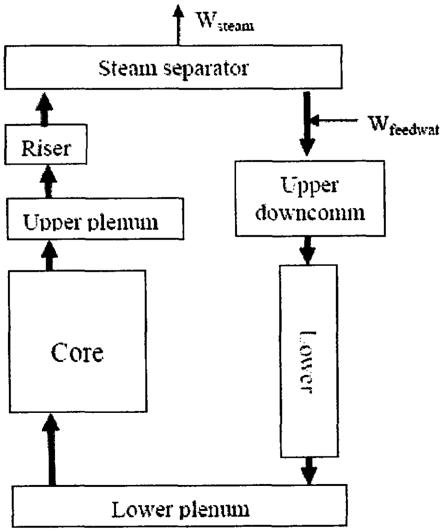

Figure-6.2: BWR Flow Path Loop for the In-phase Stability Analysis

The stability code can accommodate non-uniform power profiles as well as any pressure loss coefficients such as inlet orifice, tie plates and spacers. Models for two-phase flow and the neutronic feed back are described in this section.

The margin to instability depends on many parameters, i.e., the power to flow ratio, the inlet subcooling, the hydraulic resistances in the single and two phase regions and the nuclear feedback coefficients. In this study, the power to flow ratio, inlet subcooling and pressure loss coefficients of the reference design are held constant. Also, the new designs have mass fluxes and heat fluxes similar to those of the reference case. As a consequence, the difference in in-phase stability margin of the reference core and new designs mainly depend on the difference in the reactivity coefficients.

The main reactivity coefficients are the void and fuel temperature coefficients. It has been shown that the decay ratio is far more sensitive to the void coefficient than to the fuel temperature coefficient (see Appendix-B).

6.2.1. Core Power and Flow Distribution

The in-phase stability code implements a three-channel approach in the core. The assembly power peaking factors with the corresponding number of assemblies reported in Table-6.2 are used to model the core flow. The flow of each channel and the orificing coefficient of low power (peripheral) channel are calculated by VIPRE-01 for the candidate designs. The average and hot channel orificing coefficients are the same as the reference case.

Table-6.2: Assembly Grouping for the Stability Analysis

Assembly Type	Peaking Factor	# of Assemblies (Reference Assembly)	# of Assemblies (Large Assembly)
Hot	1.30	148	37
Average Power	1.004	500	125
Low Power	0.60	116	29

6.2.2. Calculation of the Flow of Each Channel

The unknown are the mass flow rate in the three channel regions, the core pressure drop and the orifice loss coefficient for the low power fuel assemblies. Note that the power generated in each of the three regions, the core mass flow rate and the core inlet subcooling are known. Since the exit quality in the hot channel is also fixed, the hot channel mass flow rate is immediately found from the energy equation. Then the pressure drop in the hot channel, which is equal to the pressure drop of the whole core, can be found from the momentum equation. Once the pressure drop is known, the energy and momentum equations for the average channel provide the mass flow rate and exit quality for the average channel. The mass flow rate and exit quality in the low power channel can be found from the mass equation for the whole core and the energy equation for the low power channel, respectively. Finally, the momentum equation for the low power channel provides the orifice loss coefficient for this channel.

6.2.3. Correlations and Models for the In-phase Stability Analysis

1- Bulk Void/Quality correlation: Homogeneous Equilibrium Model- Note that HEM was found to yield conservative results for the stability analysis [6]

2- Two phase Friction Multiplier is assumed to be two times Homogenous Equilibrium Model : $\phi_{lo}^2 = 2\frac{\rho_l}{\rho_m}$

ρ_l : Water density at boiling boundary

ρ_m : Mixture density in two phase region

The factor "2" in the two phase friction multiplier is suggested by both by Ishii in 1971 and Saha in 1974 for high exit qualities and it is referenced in Ref. [6].

3- Single phase forced convection correlation: Dittus-Boelter

4- Heat transfer correlation for two phase region: Thom

5- Neutronics are modeled with a Point Kinetics approach

6.2.4. Main Approximations and Modifications to the Original Stability Code

1- Non-uniform power profile capability is now included (see Appendix-B)

2- Spacer, orificing, upper and lower tie plate loss coefficients are included

3- Part length rods are treated as full length rods

6.2.5 The Geometry of Out of Core components

Tables-6.3 through Table-6.9 reports the information about the out of core components of the BWR/5 [6]. The data are included in the original code. Modeling of these components is assumed to be the same for the reference as well as large assemblies.

Table-6.3: Upper Plenum Geometry (Figure-6.2)

Upper plenum area (m^2)	17.709
Upper plenum height (m)	1.524

Table-6.4: Riser (or Steam Separator Stand Pipe) Description (Figure-6.2)

Riser area (m^2)	3.9328
Riser equivalent diameter (m)	0.15405
Riser height (m)	2.718

Table-6.5: Steam Separator Description (Figure-6.2)

Separator equivalent Diameter (m)	0.2267
Separator height (m)	2.266
Separator flow area (m^2)	8.5164
Equivalent loss coefficient of the separator	5.3232

Table-6.6: Reactor Pressure Vessel Description

Inside diameter of the RPV (m)	6.375
RPV wall thickness(m)	0.16
Density of the RPV wall(kg/m^3)	7.8E+3
Specific heat of the RPV (kJ/kg/K)	0.58

Table 6.7: Upper Downcomer Description (Figure-6.2)

Upper downcomer height (m)	2.1980
Upper downcomer flow area (m^2)	22.176
Upper downcomer equivalent diameter (m)	0.6433

Table 6.8: Lower Downcomer Description (Figure-6.2)

Lower downcomer height (m)	1.5943
Lower downcomer flow area (m^2)	8.551
Lower downcomer equivalent diameter (m)	0.8508

Table-6.9: Jet Pump Description (Figure-6.2)

Ratio of the recirculation loop	1.96
Number of the jet pumps	20
Suction flow area per jet pump (m^2)	0.04
Suction Loss Coefficient	0.35
Throat area per jet pump (m^2)	0.0354
Throat height (m)	2.5766
Throat equivalent diameter (m)	0.21224
Upper part diffuser inlet diameter (m)	0.21224
Upper part diffuser outlet diameter (m)	0.2535
Upper part diffuser height (m)	0.3053
Lower part diffuser inlet equivalent diameter (m)	0.2535
Lower part diffuser inlet equivalent diameter (m)	0.4826
Lower part diffuser height (m)	1.8865

Discharge region area per jet pump (m^2)	0.183
Discharge region height (m)	0.2432
Equivalent diameter of discharge region (m)	0.4826
Form loss coefficient of discharge region	1.0

6.2.6. Neutronic Parameters:

Neutronic parameters related to the point kinetics model used in the analysis are given in Table-6.10, Table-6.11 and Table-6.12. The mean generation time is calculated via MCNP using the Beginning of Cycle model of the Large and Reference Core developed in this study (see Section 9).

Table-6.10: Mean Generation Time

Reference Assembly	Large Assembly
2.8E-05 sec	2.3E-05 sec

Table-6.11: Six Group Delayed Neutron Fraction

β_1	2.211E-04
β_2	1.467E-03
β_3	1.313E-03
β_4	2.647E-03
β_5	7.705E-04
β_6	2.814E-04

Table-6.12: Six Group Decay Constants (sec^{-1})

λ_1	0.0124
λ_2	0.0305
λ_3	0.111
λ_4	0.301
λ_5	1.14
λ_6	3.01

6.2.7. In-phase Stability Results

The flow in each channel (calculated via VIPRE-01) and the reactivity coefficients (calculated by the 3D MCNP simulation of Chapter 9) are shown in Table-6.13 and Table-6.14. The resulting decay ratio is also shown in these tables.

Table-6.13: In-phase Stability Analysis of the Reference Core

Assembly Type	# of Assemblies (Reference Assembly)	Assembly Power (MW)	Flow per assembly (kg/s)	Orificing Coefficient	Void Coefficient (pcm/ % void)	Fuel Temperature Coefficient (pcm/K)	Decay Ratio
Hot	148	5.65	15.785	21.089	-144	-1.7	0.31
Average Power	500	4.37	16.824	21.089			
Low Power	116	2.61	8.927	182.049			

Table-6.14: In-phase Stability Analysis of the Large Assembly Core

Assembly Type	# of Assemblies (Large Assembly)	Assembly Power (MW)	Flow per assembly (kg/s)	Orificing Coefficient	Void Coefficient (pcm/ % void)	Fuel Temperature Coefficient (pcm/K)	Decay Ratio
Hot	37	27.14	75.9866	21.089	-180	-2.3	0.36
Average Power	125	20.96	81.2120	21.089			
Low Power	29	12.53	40.5914	214.0			

As a result of the core-wide stability analysis, it is found that the new design has 16 % higher decay ratio, so the margin to in-phase oscillations is reduced; though it is still far less than the recommended limit of 0.5.

Increasing the inlet orificing coefficient is very effective in improving the single channel stability, but not so for the in-phase stability (See Appendix-B). That is, a very high orificing may reduce the decay ratio back to 0.31, however, at the expense of a very high pressure drop, which would not be acceptable. Another way to restore the stability margin is to decrease the inlet subcooling (see Appendix-B). However, a lower subcooling directly reduces the dryout margin, which is unacceptable. In conclusion, it is decided to accept a modest reduction of the margin to stability in exchange for the higher power density.

7. MECHANICAL VIBRATION STUDY

The rod vibration mechanism in two-phase flow is still a relatively unexplored field [16]. The purpose of the present work is not a thorough investigation of the vibration mechanisms that occur in the core, but rather a simplified approach to obtain a conservative estimate of the large fuel assembly susceptibility to mechanical vibrations.

The parameter chosen to express the vibrations magnitude is the so-called "vibration ratio", and is defined as the ratio between the maximum peak vibration amplitude and the rod diameter (y/d). In this study, the modified Païdoussis correlation (Appendix-D) is used to calculate the vibration ratio of the reference as well as new fuel assemblies. The correction factor is selected as fifteen according to the worst mismatch with the experimental measurements [14].

Assumptions:

1- The present analysis neglects the presence of the fuel inside the rods.

2- Vibration ratio is calculated at the end of the hot channel

Both assumptions are conservative, i.e., they tend to overestimate the vibration ratio.

Vibration limit value

Reference [17] states that: "For PWR fuel rods, maximum amplitude of 0.2 to 0.25 mm is generally accepted as design criterion for vibrations". Taking conservatively the lower end of the suggested range, and using $d = 9.5$ mm as rod diameter (average value for PWR rods):

$$\frac{y}{d} = \frac{0.2}{9.5} \approx 0.021$$

Results:

Table-7.1: Vibration Ratio of the Reference and Large Assembly

	Calculated Vibration Ratio	Limiting Vibration Ratio
Reference Assembly	0.006	0.021
Large Assembly	0.013	

As can be seen in Table-7.1, the large assembly has 117 % higher vibration ratio than the reference assembly, mostly due to the lower diameter of the fuel pins; however, still far less than the limiting value. Although the design is well within the envelope, it is possible to increase number of spacers to achieve the vibration ratio identical to the reference case. It was found that adding more spacers may reduce the vibration ratio (Table-7.2). On the other hand, this approach results in a higher core pressure drop.

Table-7.2: Vibration Ratio of the Large Assembly as a Function of Number of Spacers

# of Spacers	Pressure Drop (kPa)	Vibration Ratio
7	187.3	0.013
8	194.3	0.008
9	201.6	0.006

8. 2D NEUTRONICS

The main purpose of the 2D neutronic calculation is to obtain the desired distribution of enrichment and poison rods, resulting in satisfactory PPFs and discharge burnup for a given assembly geometry.

The constraints of the neutronic analysis are as follows:

1- 18-month cycle
2- 1% reactivity shutdown margin (3D neutronics study, see Chapter-9)
3- Average discharge burnup <60 MWd/kg
4- Peak enrichment <5 %wt.

The discharge burnup roughly depends on the average enrichment of the assembly; however, a strongly non-uniform enrichment distribution is inevitable to obtain satisfactory PPFs, due to heterogeneities in moderation and the presence of burnable poison rods.

A significant amount of excess reactivity of a typical BWR is held in gadolinia rods. Since it is desired to minimize the poison concentration at the end of cycle (EOC), the poison concentration per rod is fixed by the specific power density. On the other hand, the number and position of the gadolinia rods in the fuel assembly depend on the number and reactivity of the control rods, and impact also the power peaking factors.

Void Coefficient

The void coefficient of a typical BWR characterizes the relative contribution of the coolant to the moderating power. Since the total number of hydrogen atoms is approximately fixed in the large assembly design, an increase of flow area results in an increase of coolant worth and will result in more negative void coefficient.

Poison rod concentration and distribution are parameters that affect the void coefficient. For instance, if the gadolinia rods were located at the periphery of an assembly, the thermal neutrons, well moderated by the inter-assembly gap water, would be absorbed by the poison. As a result, the relative contribution of the coolant to the total moderating power will increase. To reduce the void coefficient, one can place the gadolinia rods at relatively less thermalized positions. In this situation, the enrichment variation to reduce power peaking factors becomes challenging and the poison rods also lose some worth. Thus, a compromise is necessary.

The effect of control rods on the void coefficient is also considerable. The control rods are located within the moderator regions; thus, they can reduce the relative contribution of the moderator regions to the moderating power. Moreover, control and gadolinia rods harden the spectrum of the core. As a result of the harder spectrum, the importance of both moderator and coolant increases, causing a more negative void coefficient, which is the conservative case for the stability analysis.

Finger Type Control Rods

Finger type control rods have many superior neutronic features with respect to cruciform control rods. Cruciform control rods include many absorber rods in packed form. Since the rods are close to each other, the worth per rod is reduced. In contrast, finger type control rods are individually placed within the water rods. This feature enhances the worth of each rod considerably. For a given required shutdown margin, the total volume of control rod elements can be reduced. Because the finger type control rods replace a smaller amount of moderator, the volume of the moderator will be higher in normal operation, thus, helping to reduce the void coefficient somewhat. On the other hand, the bypass flow region, which is not heated, is reduced, and that tends to increase the void coefficient.

8.1. Modeling Details

The 2D calculations have been performed with CASMO-4 and include varying geometry and composition of the fuel pins, water rods, assembly duct and inter-assembly gap.

Assumptions:

1- Calculations are performed at core average coolant density and fuel and coolant temperature. Because the coolant density tends to be lower near hotter rods and hotter fuel rods operate at higher temperatures, resulting in power flattening. This assumption is conservative to predict dryout margin.

2- Part length rods as well as top and bottom blankets are not included. On the other hand, an approach is developed to include the effect of partial length rods to power peaking factors (Appendix-C).
3- Spacers are lumped into the coolant. This approach helps predict the reactivity loss by spacers.
4- Because the water rods are larger than two times the fuel pin pitch for the large assembly design, they are defined within a 2×2 cell with an effective equivalent moderator density. The number of water and clad material atoms is preserved.
5- ½ symmetry is used to model the reference assembly.
6- 1/8 symmetry is used in the large assembly design.
7- Approximately 3 % leakage reactivity, which is typical of LWRs [18], is assumed.
8- Maximum allowable enrichment is 5 %.
9- Maximum allowable discharge burnup is 60 GWd/t.

Main objectives of 2D Neutronics:

1- Select fuel enrichment distribution to satisfy the discharge burnup limit
2- Calculate the PPFs
3- Select the poison concentration per rod such that residual amount of poison will be less than 1.0 wt % at the end of a cycle
4- Select the number of poisoned rods necessary to manage the excess reactivity

8.2. Results

8.2.1. Reference Assembly

The optimized 2D composition of the reference assembly is necessary for 3D neutronics to calculate reactivity coefficients of the reference core. However, the power peaking factors used in the subchannel analysis of the reference assembly are those of Figures 3.5 and 3.7, not those calculated from the 2D neutronics.

Fuel Composition

The numbering of the positions within the fuel assembly assumes ½ symmetry. Each fuel pin properties are given in Table-8.1. Five enrichments are allowed. Each assembly has 12 poisoned rods with 5 wt% Gadolinia. Composition layout is given in Table-8.2.

Table-8.1: Composition Numbering of the Reference Assembly

Fuel Number	Fuel Density (g/cm^3)	Fuel Enrichment (wt %)	Gadolinia (wt %)
1	10.4	2.6	0
2	10.4	4.3	0
3	10.4	4.8	0
4	10.1	4.45	5.0
5	10.4	3.45	0

Table-8.2 Composition Layout of the Reference Assembly

1								
5	2							
2	3	4						
2	4	3	3					
2	3	3	0	0				
2	4	3	0	0	3			
2	3	4	3	3	3	4		
5	2	3	4	3	4	3	2	
1	5	2	2	2	2	2	5	1

2D Burnup Calculation

The burnup dependent calculation is performed to estimate the composition necessary for the desired cycle length. Figure-8.1 shows the time history of the infinite multiplication factor of an assembly from beginning of life to end of life at core average power. Due to gadolinia depletion by the end of the first cycle, infinite multiplication factor drops smoothly.

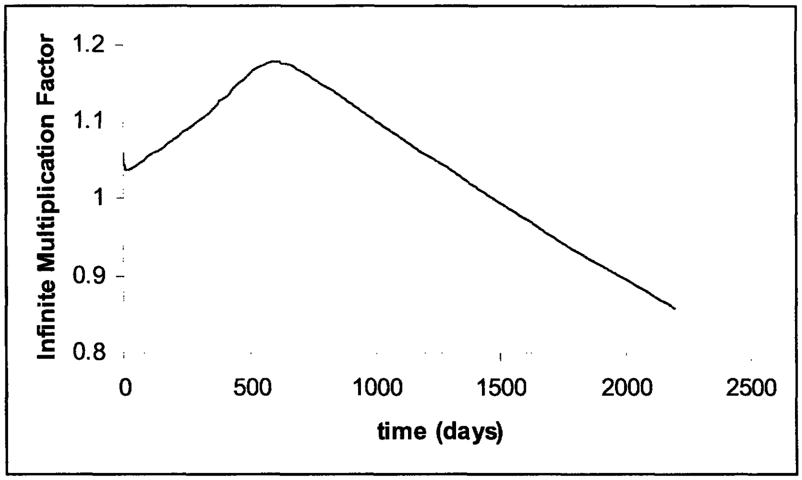

Figure-8.1: Time History of the Infinite Multiplication Factor of the Reference Assembly for 2D Calculation

As can be seen in Table-8.3, the optimized assembly composition allows 4 batch refueling and 18-month cycle and an assumed 3 % leakage.

Table-8.3: Main Results Related to 2D Neutronics of the Reference Assembly

Discharge Burnup (GWd/t)	55.84
Power Density (kW/l)	50.5
Cycle Length (months)	18
Maximum Enrichment	4.80
Average Enrichment	4.32
Number of Batches	4
Leakage Reactivity (assumed)	~3 %

8.2.2. The Large Assembly

The 2D neutronic analysis is performed coupled with the subchannel analysis. Mainly, it is performed to calculate the power peaking factors for the fresh as well as once burned composition. Furthermore, the resulting 2D composition is also used for 3D neutronics.

The numbering of the positions within the fuel assembly assumes a ⅛ symmetry. Each fuel pin properties are given in Table-8.4. Five different enrichments are allowed. The gadolinia concentration per rod is 6 % vs 5 % in the reference case. The corresponding composition layout is given in Table-8.5.

Table-8.4 Composition Numbering of the Large Assembly

Fuel Number	Fuel Density (g/cm^3)	Enrichment (wt %)	Gadolinia (wt %)
1	10.4	4.6	0
2	10.1	4.0	6.0
3	10.4	2.65	0
4	10.4	3.15	0
5	10.4	4.0	0
6	10.4	3.75	0

Table-8.5 Composition Layout of the Large Assembly

3										
4	4									
6	5	1								
5	2	5	0							
5	5	5	0	0						
6	6	5	4	6	6					
6	6	0	0	6	5	0				
6	6	0	0	5	5	0	0			
5	2	5	5	2	1	5	1	2		
5	5	2	5	1	1	2	1	1	1	
5	5	0	0	1	5	0	0	1	1	0

Burnup Calculation

The burnup calculation is performed to estimate the composition necessary for required cycle length as well as fresh and once burned power peaking factors at full power. Figure-8.2 shows the time history of the infinite multiplication factor of a large assembly from beginning of life to end of life at core average power. As in the reference case, Gadolinia is depleted by the end of the first cycle and infinite multiplication factor falls smoothly afterwards.

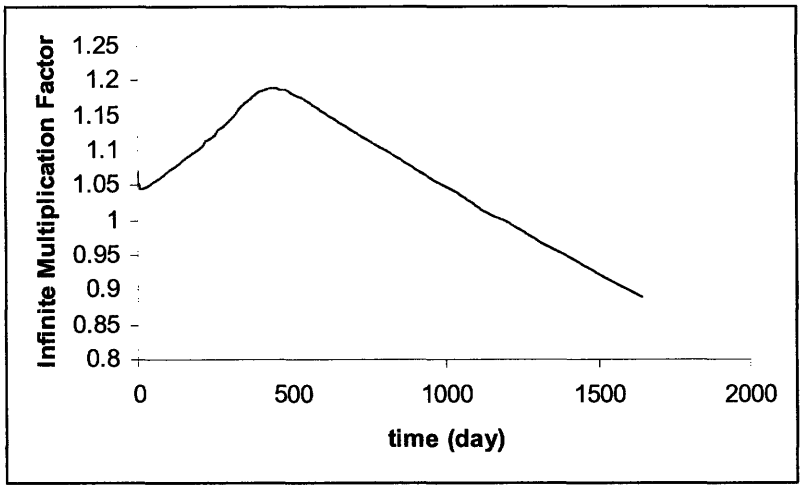

Figure-8.2: Time History of the Infinite Multiplication Factor of the Large Assembly for 2D Calculation

Unlike the reference case, the new design has a three-batch refueling scheme. Because the allowable discharge burnup is limited at 60 MWd/kg, a four-batch refueling scheme is no longer possible with 20% power uprate and the same heavy metal inventory. As a result, the discharge burnup of the new design is somewhat lower than the reference case, but the average enrichment is also somewhat lower. As can be seen in Table-8.6, the optimized assembly composition allows three batch refueling and 18 month cycle and an assumed 3 % leakage.

Table-8.6: Main Results Related to 2D Neutronics of the Large Assembly

Discharge Burnup (GWd/t)	49.75
Power Density (kW/l)	60.6
Cycle Length (Months)	18
Maximum Enrichment	4.60
Average Enrichment	4.02
Number of Batches	3
Leakage Reactivity (assumed)	~3 %

The power peaking factors of the fresh and once burned large assembly at full power, as given by CASMO-4, are given in Table-8.7 and Table-8.9, respectively. These power peaking factors are modified to account for partial length rods (see Appendix-C), and the modified PPFs are given in Table-8.8 and Table-8.10, respectively, which were used in the subchannel analyses of the large fuel assembly (Section 5).

Table-8.7 Fresh Assembly Power Peaking Factors (CASMO-4)

1.207										
1.198	**1.016**									
1.224	1.065	1.150								
1.191	0.403	1.083	0.000							
1.210	1.061	1.170	0.000	0.000						
1.183	**1.093**	1.238	1.103	1.202	1.114					
1.183	1.140	0.000	0.000	1.130	1.150	0.000				
1.134	1.051	0.000	0.000	1.053	1.054	0.000	0.000			
1.111	0.389	0.945	0.969	0.380	0.973	0.936	1.020	0.375		
1.117	0.922	0.385	0.936	0.965	0.938	0.382	1.009	0.958	1.002	
1.146	1.047	0.000	0.000	1.081	0.945	0.000	0.000	1.083	1.112	0.000

Bold PPFs are part length rods.

Table-8.8 Fresh Assembly Power Peaking Factors (Modified)

1.217										
1.208	**0.768**									
1.234	1.074	1.160								
1.201	0.406	1.092	0.000							
1.220	1.070	1.180	0.000	0.000						
1.203	**0.826**	1.248	1.112	1.212	1.123					
1.193	1.150	0.000	0.000	1.139	1.160	0.000				
1.144	1.060	0.000	0.000	1.062	1.063	0.000	0.000			
1.120	0.392	0.952	0.977	0.383	0.981	0.944	1.029	0.378		
1.126	0.930	0.388	0.943	0.973	0.946	0.385	1.017	0.966	1.010	
1.156	1.056	0.000	0.000	1.090	0.953	0.000	0.000	1.092	1.121	0.000

Bold PPFs are part length rods.

Table-8.9: Once Burned Assembly Power Peaking Factors (CASMO-4)

0.968										
0.976	**0.890**									
1.029	0.974	1.044								
1.047	0.961	1.003	0.000							
1.037	0.975	1.019	0.000	0.000						
1.006	**0.956**	1.042	0.958	1.010	0.966					
1.013	0.996	0.000	0.000	0.988	1.007	0.000				
1.014	0.998	0.000	0.000	1.003	0.991	0.000	0.000			
1.045	0.985	1.022	1.005	0.934	1.009	0.974	1.040	0.894		
1.043	0.993	1.006	0.995	1.011	1.000	0.960	1.034	0.971	0.962	
1.044	1.023	0.000	0.000	1.049	0.965	0.000	0.000	1.014	1.010	0.000

Bold PPFs are part length rods.

Table-8.10: Once Burned Assembly Power Peaking Factors (Modified)

0.975										
0.983	**0.673**									
1.037	0.981	1.052								
1.055	0.968	1.010	0.000							
1.045	0.982	1.026	0.000	0.000						
1.013	**0.723**	1.050	0.965	1.017	0.973					
1.020	1.003	0.000	0.000	0.995	1.014	0.000				
1.021	1.005	0.000	0.000	1.010	0.998	0.000	0.000			
1.053	0.992	1.030	1.012	0.941	1.016	0.981	1.048	0.901		
1.051	1.000	1.013	1.002	1.018	1.007	0.967	1.042	0.978	0.969	
1.052	1.031	0.000	0.000	1.057	0.972	0.000	0.000	1.021	1.017	0.000

Bold PPFs are part length rods.

9. 3D NEUTRONICS

The main purposes of the 3D neutronic analysis are (1) to size the control rods so that a 1% reactivity margin at cold shutdown is achieved, (2) verify that the core is critical at EOC and (3) calculate the void and fuel temperature coefficients that will be used in the stability analysis.

The reactivity coefficients show strong variation with burnup. Due to the highest amount of control rods and gadolinia, the beginning of cycle is found to have the most negative void coefficient. Therefore, for a conservative estimate of the stability margin, the beginning of cycle situation is modeled in the 3D neutronic analysis.

In normal operation, the BWR core includes control rods. Moreover, axial variation of enrichment and poison are also essential to predict the power profile. Due to limitations on computational tools, a rigorous solution is not pursued in this study.

9.1. Methodology

The first step of the 3D analysis includes burnup calculations with one assembly model with radially symmetric boundary condition. The optimized composition obtained via the 2D neutronics is the input for the 3D model. This model does not include control rods and Gadolinium-155 and Gadolinium-157 in the poison rods. Inclusion of the control rods in a one-assembly burnup calculation would cause top peaked power profile. Gadolinia would burn faster in the lower half of the assembly due to the higher thermal flux, which would result in accelerated poison depletion in this region. On the other hand, poison in the upper half could not be burned properly before the end of cycle. As a consequence, including control rods and/or gadolinia may cause highly unrealistic power profiles during burnup of one assembly. To estimate the composition of the fresh assembly at full power, the fresh assembly is burned up to 0.1 MWd/kg, including Gadolinium-155 and Gadolinium-157. The thermalhydraulic feedback is provided via the reference axial power profile (Figure-3.2) and is not updated as a function of burnup. The objective of this step is to obtain an approximate composition of fresh, once, twice, thrice and fourth burned assemblies at full power.

The second step of the 3D analysis is the modeling of beginning of cycle (BOC) and end of cycle (EOC) states. Inserting the fresh, once, twice, thrice and fourth burned assembly composition into an n×n matrix, the approximate core configurations for BOC and EOC are obtained with a periodic boundary condition in x-y direction. Again the reference axial power profile is maintained for the thermalhydraulic feedback. First the EOC case is analyzed to check that the core is critical at the end of the irradiation cycle. Then, BOC modeling at hot full power as well as cold zero power is performed. BOC at cold zero power is modeled to select the control rod diameter necessary to satisfy the 1% shutdown margin criterion. BOC at hot full power including control rods inserted to obtain an exactly critical core is the desired configuration for the calculation of reactivity coefficients. The final step is to actually calculate the void and fuel temperature coefficients using the BOC neutronic model coupled with VIPRE-01. Reducing and increasing the power around its nominal value changes the fuel temperature and void fraction about their nominal value, and taking the derivative gives the reactivity coefficients.

9.2. Modeling Details

9.2.1. The One Assembly Model

The 3D burnup calculation with the one assembly model is performed with the MCODE, which couples MCNP and ORIGEN2.2.

One assembly is modeled including half of the inter-assembly gap, the top and bottom blankets and top and bottom reflectors. The radial symmetry boundary condition is applied; while axial leakage is allowed. The burnup model includes 12 axial nodes. The composition of the fuel cells is specified according to enrichment and poison concentration. Each different combination of enrichment and poison concentration is depleted separately.

Reference Assembly Model

Figure-9.1 shows a cross section of the reference assembly. The axial location of this plot is higher than the length of part length rods; so, those locations are occupied by water. The table on the right includes information on the axial variations within the core region.

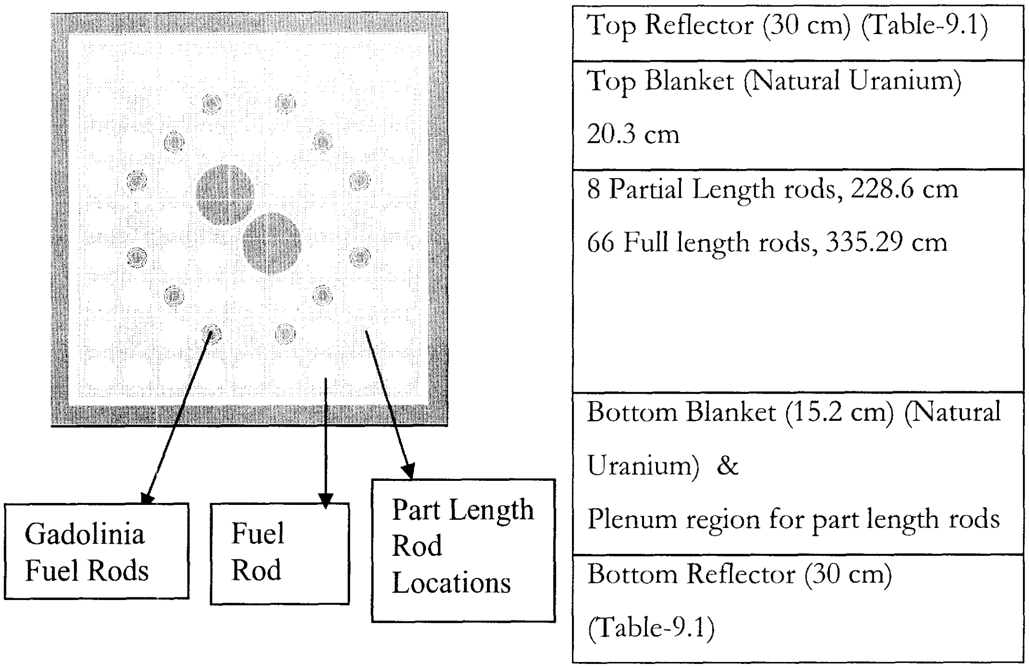

Figure-9.1: Reference Assembly MCNP Model

The top and bottom reflector compositions include the structural materials in addition to the coolant. Typical PWR top and bottom reflector materials [19] together with calculated coolant density are modeled in lumped form. The resulting compositions are given in Table-9.1

Table-9.1: Composition of Top and Bottom Reflectors

Composition	Atom Density ($\times 10^{-21}$) (atoms/ cm^3)	
	Bottom Reflector	Top Reflector
Carbon	0.15516	0.15516
Iron	29.1665	29.1665
Chromium	8.51270	8.51270
Nickel	3.57130	3.57130
Manganese	1.71614	1.71614
Hydrogen	25.2110	6.72890
Oxygen	12.6050	3.36430

Large Assembly Model

Figure-9.2 shows a cross section of the most promising large assembly. The axial location of this plot is higher than the length of part length rods; so, those locations are occupied by water. Table on the right includes information on the axial variations within core region.

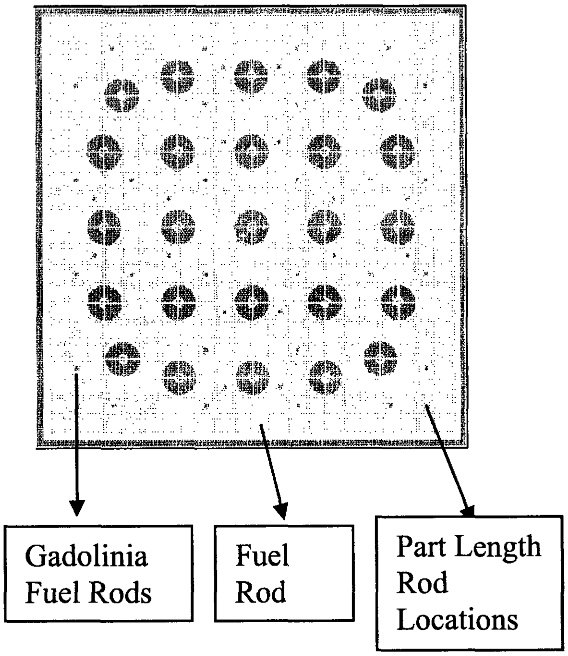

Top Reflector (30 cm) (Table-9.1)
Top Blanket 20.3 cm (Natural Uranium)
12 Partial Length rods, 228.6 cm 372 Full length rods, 335.29 cm
Bottom Blanket (15.2 cm) (Natural Uranium) & Plenum region for part length rods
Bottom Reflector (30 cm)(Table-9.1)

Figure-9.2: Large Assembly MCNP Model

Assumptions related to MCNP:

1- MCNP uses the fresh assembly composition obtained from CASMO-4, which does not include information about the axial variation of composition

2- Cross-section libraries are assigned according to the temperature of corresponding regions.

3- The S (α,β) card has been used to account for molecular binding effects in the coolant and moderator at 600K

4- The radial average coolant density is calculated with VIPRE-01 and entered at 12 axial locations.

5- The radial average fuel, gap, clad and coolant temperatures within the assembly are included in TMP card for each cell

6- 2.4 Million histories are simulated in each MCNP run

7- The spacer material is incorporated in the coolant number density.

Assumptions related to burnup calculations:

1- Control rods are not included in burnup calculations.

2- Gadolinia-155 and 157 are not included in burnup calculation to estimate once burned and twice burned and third burned composition. Inclusion of poison together with other approximations may cause highly unrealistic power profile. Therefore, an implicit assumption is stated that once burned assembly does not include any poison.

3- To estimate fresh composition at xenon equilibrium, burnup calculation is performed with Gd-155 and 157 for 0.1 MWd/kg

4- The assembly is assumed to generate a constant power throughout the irradiation cycle.

5- The initial temperature and coolant density profile (calculated for the reference power profile) is preserved throughout the irradiation cycle.

9.2.2. Equilibrium Cycle Modeling

After having obtained the burned assembly compositions from the burnup calculations, the BOC and EOC at xenon equilibrium are modeled for a cluster of burned assemblies representing the whole core.

Assumptions

1- The control rods are inserted in the twice burned assemblies at BOC

2- The periodic boundary condition is applied to radial boundaries, while axial leakage is allowed

3- All assemblies have the same coolant density and cell temperatures.

4- 6 Million histories are modeled in each run.

Reference Core

Beginning of Cycle (BOC):

BOC geometric model is shown in Figure-9.3. Fresh, once, twice and thrice burned 9×9 assemblies are inserted into a 4×4 matrix. As can be seen in Figure-8.4, four twice burned assemblies are placed in the 2×2 matrix in the upper right corner and receive the cruciform control rod to establish criticality. Because control elements may cause quite a high axial peaking factor, the fresh or once burned assemblies should not receive the control elements under normal operation.

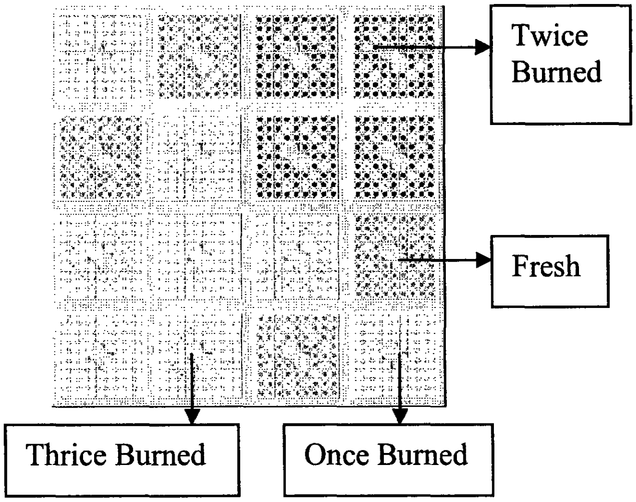

Figure-9.3: Beginning of Cycle Model of the Reference Core

End of Cycle (EOC) Model:

EOC modeling (Figure-9.4) includes once, twice, thrice and fourth burned assemblies. The fresh, once, twice and thrice assemblies at BOC become the once, twice, thrice and fourth burned assemblies at EOC. The control rods are completely withdrawn.

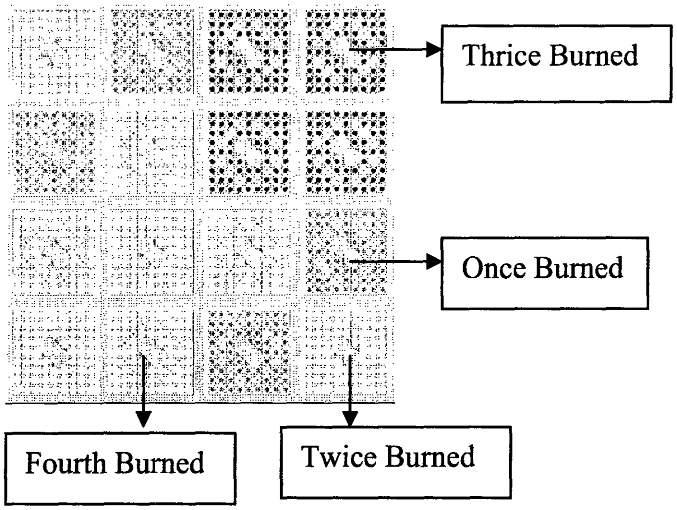

Figure-9.4 End of Cycle Model of the Reference Core

Large Assembly Core

Beginning of Cycle (BOC):

The BOC geometric model is given in Figure-9.5. Fresh, once and twice burned large assemblies are inserted into a 3×3 matrix. The twice burned assemblies receive the finger type control rods to establish criticality.

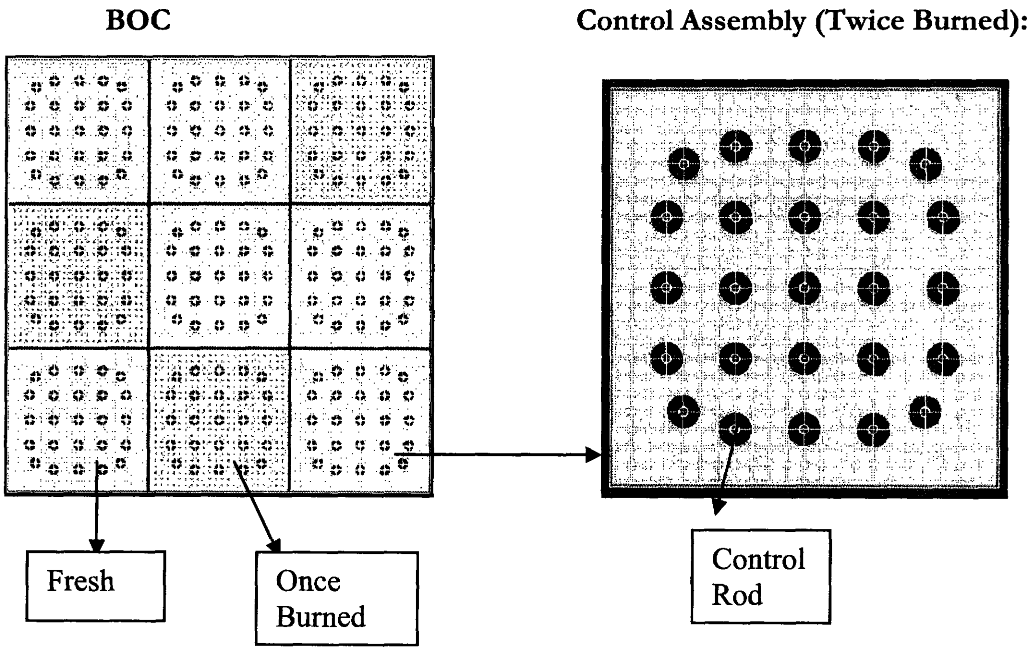

Figure-9.5: Beginning of Cycle Model of the Large Assembly Core

End of Cycle Modeling:

The EOC modeling (Figure-9.6) includes once, twice and thrice burned assemblies. The fresh, once and twice burned assemblies at BOC become the once, twice and thrice burned assemblies at EOC, respectively. The control rods are totally withdrawn.

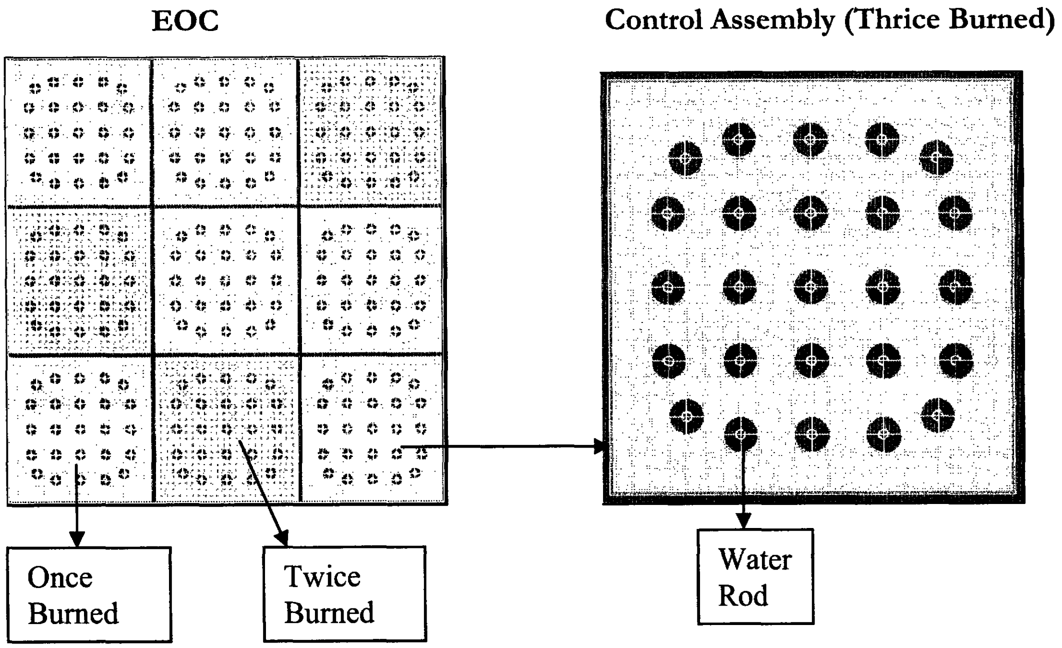
EOC

Control Assembly (Thrice Burned)

Figure-9.6: End of Cycle Model of the Large Assembly Core

9.2.3. Calculation of the Reactivity Coefficients

The void and fuel temperature coefficients are calculated with the help of VIPRE-01 at Beginning of Cycle at full power.

The following steps summarize the calculation of the void coefficient:

1- The power is reduced such that the assembly average void fraction is 10 % lower than the nominal value. MCNP is run with this axial coolant density distribution

2- The power is increased such that the assembly average void fraction is 10 % higher than the nominal value. MCNP is run with this axial coolant density distribution

3- The central derivative gives the void reactivity coefficient.

The fuel temperature coefficient depends on the resonance behavior due to Doppler broadening. The MCNP cross section libraries include data at 800K and 900K. The following steps are implemented for the calculation of the fuel temperature coefficient:

1- MCNP is run for an average fuel temperature of 800K.
2- MCNP is run for an average fuel temperature of 900K.
3- The central derivative gives the fuel temperature reactivity coefficient.

9.3. Results

9.3.1. Reference Core

One Assembly Model Burnup Calculations:

The time history of the multiplication factor of the reference assembly can be seen in Figure-9.7.

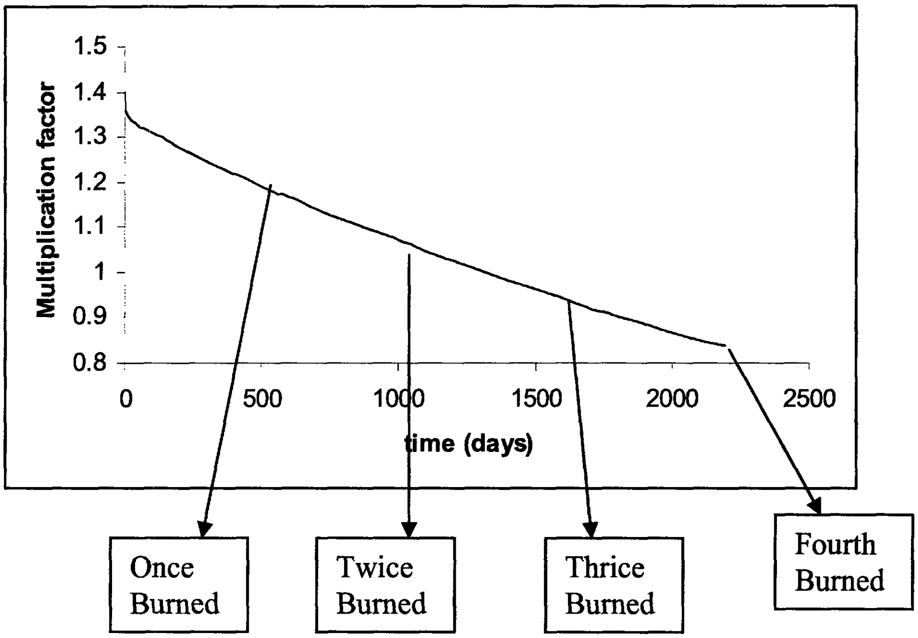

Figure-9.7: Time History of the Multiplication Factor for the Reference Assembly for 3D Calculation

To obtain fresh assembly composition at full power, fresh assembly is burned to 0.1 MWd/kg with Gadolinia 155 and 157. The multiplication factors are given in Table-9.2. Note that, fresh assembly at full power and xenon equilibrium is used to simulate the Beginning of Cycle (Table-9.4).

Table-9.2: Fresh Assembly Multiplication Factor

Burnup (GWd/t)	Multiplication Factor
0	1.05854±0.00051
0.1	1.03350 ±0.00051

The second step of the calculations includes BOC and EOC modeling. Assembly numbering and corresponding BOC and EOC configurations are given below.

Assemblies are numbered in Table-9.3 according to their burnup level.

Table-9.3: Composition Numbering of the Reference Assembly

Assembly type	Assembly Number
Fresh at full power	0
Once Burned	1
Twice Burned	2
Thrice Burned	3
Fourth Burned	4

Beginning of Cycle

Table-9.4 shows the beginning of cycle configuration.

- 79 % of the control element is inserted in twice burned assembly quadrant to establish criticality
- All assemblies are at full power and xenon equilibrium

Table-9.4: Beginning of Cycle of the Reference Core at Hot Full Power

1	**0**	**2** **CR 79 % in**	**2** **CR 79 % in**
0	**3**	**2** **CR 79 % in**	**2** **CR 79 % in**
3	**1**	**3**	**0**
1	**3**	**0**	**1**

k=1.00184±0.00028

End of Cycle

Table-9.5 shows the End of Cycle configuration.

- All Control Rods Out
- All assemblies are at full power and xenon equilibrium

Table-9.5: End of Cycle Modeling of the Reference Core at Hot Full Power

2	1	**3 CR OUT**	**3 CR OUT**
1	4	**3 CR OUT**	**3 CR OUT**
4	2	4	1
2	4	1	2

k=1.00250±0.00023

The multiplication factor for the Beginning of Cycle as well as End of Cycle is close to unity.

Calculation of the Reactivity Coefficients:

The results of the void and fuel temperature reactivity feedback calculations are shown in Table-9.6 and Table-9.7, respectively. These results are consistent with actual data from commercial BWR plants [20].

Table-9.6: Calculation of the Reference Core Void Coefficient

Assembly Power (% of the Nominal average Power)	Void Fraction (Vol. %)	Multiplication Factor	Void Coefficient (pcm/%Void)
69.5 %	36.1	1.01715 ± 0.00025	-144
148.5 %	56.1	0.98823 ± 0.00028	

Table-9.7: Calculation of the Reference Core Fuel Temperature Coefficient

Assembly Power (% of the Nominal average Power)	Average Fuel Temperature (Kelvin)	Multiplication Factor	Fuel Temperature Coefficient (pcm/K)
89.9 %	800	1.00196	-1.7
121.9 %	900	1.00023	

9.3.2 Large Assembly Core

The time history of the multiplication factor for the large assembly can be seen in Figure-9.8.

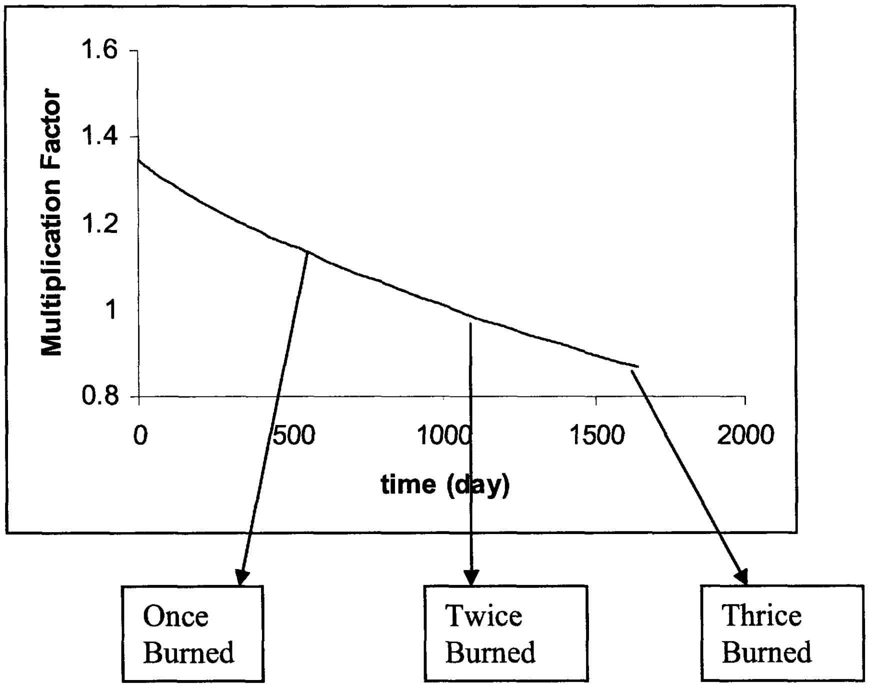

Figure-9.8: Time History of the Multiplication Factor for the Large Assembly for 3D calculation

To obtain the fresh assembly composition at full power, the fresh assembly is burned to 0.1 MWd/kg with Gadolinia 155 and 157. Table-9.8 gives the multiplication factor at beginning of life and at 0.1 MWd/kg. Note that, fresh assembly at full power and xenon equilibrium is used to simulate the Beginning of Cycle (Table-9.10 and Table-9.12).

Table-9.8: Fresh Assembly Multiplication Factor

Burnup (GWd/t)	Multiplication Factor
0	1.07747±0.00044
0.1	1.04702±0.00044

After obtaining the burned assembly compositions, the Beginning of Cycle and End of Cycle of an equilibrium core are modeled. Assemblies are numbered in Table-9.9 according to their burnup level.

Table-9.9: Assembly Numbering of the Large Assembly

Assembly type	Assembly Number
Fresh	0
Once Burned	1
Twice Burned	2
Third Burned	3

Beginning of Cycle

The BOC is modeled at cold zero power to select the control rod diameter satisfying 1% shutdown margin. The configuration is given in Table-9.10.

- All control rods in (Each water rod receives one control rod)
- System temperature is 300 K
- There is no Xenon in the system

Table-9.10: Beginning of Cycle of the Large Assembly Core at Cold Zero Power

2 CR IN	0 CR IN	1 CR IN
1 CR IN	2 CR IN	0 CR IN
0 CR IN	1 CR IN	2 CR IN

k= 0.98931±0.00021

Table-9.11: Control Rod Geometry of the Large Assembly

Control Rod diameter (Boron Carbide)	0.64 cm
Clad thickness (stainless steel)	0.05 cm

As can be seen above, approximately 1 % shutdown margin is allowed with the control rod geometry given in Table-9.11.

The BOC at Hot Full Power is simulated to calculate reactivity coefficients. The configuration is given in Table-9.12.

- Control rods are inserted into twice burned assembly to establish criticality
- Full power
- Xenon is included

Table-9.12: Beginning of Cycle of the Large Assembly Core at Hot Full Power

2 CR 84 % in	0	1
1	2 CR 84 % in	0
0	1	2 CR 84 % in

k= 1.00197±0.00019

End Of Cycle:

EOC at full power is modeled to obtain multiplication factor. The configuration is given in Figure-9.13.

- All Control Rods Out
- Xenon is included
- Hot Full Power

Table-9.13: End of Cycle of the Large Assembly Core at Hot Full Power

3 CR OUT	1	2
2	3 CR OUT	1
1	2	3 CR OUT

k= 1.00553±0.00024

The multiplication factors for the Beginning of Cycle as well as End of Cycle are close to unity.

Calculation of the Reactivity Coefficients

The results of the void and fuel temperature reactivity feedback calculations are reported in Table-9.14 and Table-9.15, respectively.

Table-9.14 Calculation of the Large Assembly Core Void Coefficient

Assembly Power (% of the Nominal average Power)	Void Fraction (Vol. %)	Multiplication Factor	Void Coefficient (pcm/%Void)
69.4 %	35.1	1.02097±0.00027	-180
148.4 %	55.1	0.98474±0.00027	

Table-9.15 Calculation of the Large Assembly Core Fuel Temperature Coefficient

Assembly Power (% of the Nominal average Power)	Average Fuel Temperature (Kelvin)	Multiplication Factor	Fuel Temperature Coefficient (pcm/K)
92.7 %	800	1.00227±0.00024	-2.3
126.3 %	900	1.00000±0.00023	

It has been shown that the resulting void coefficient of the large assembly core is 25 % more negative and fuel temperature coefficient is 35 % more negative than the reference core.

These estimates of the reactivity coefficients for the reference as well as large assembly cores are conservative, i.e., they overestimate the coefficients and thus the decay ratio for two reasons. First, the calculation has been performed at the beginning of cycle, which has the highest amount of control rods and poison and fissile nuclei. Among them, the control rods have the largest effect on the void coefficient. Second, the radially periodic boundary condition eliminates a proper modeling of radial leakage and thermalization due to radial reflector. Normally, radial leakage results in diffusion cooling, which softens the spectrum at the periphery. Furthermore, the periphery has higher moderating power due to the reflector region. Thus, a simulation without radial leakage causes a harder spectrum; which increases the reactivity worth of the coolant.

10. FUEL THERMO-MECHANICAL ANALYSIS

FRAPCON steady state thermo-mechanical fuel rod modeling code is used to examine the performance of the Zircalloy cladding of the reference and the most promising large assembly fuel rod. The required code input includes fuel and cladding geometry, fuel enrichment, primary coolant conditions, and the neutron flux, linear heat generation rate, and axial power shape at each time steps. Table-10.1 shows the main input specifications for the reference and the large assembly rods.

Table-10.1: Input Specifications for the Reference and Large Assembly Rods

	Reference Rod	**Large Assembly Rod**
Cold Plenum Length (cm)	28.5	28.5
Clad Thickness (cm)	0.0711	0.057
Gap Thickness (cm)	0.0102	0.0085
Clad Outer Diameter (cm)	1.1176	0.96
Fuel Rod Pitch (cm)	1.427	1.305
Fuel Pellet Outer Diameter (cm)	0.955	0.829
Outer Diameter of the Plenum Spring (cm)	0.973	0.843
Enrichment	4.3	4.0
Height of the Fuel Pellet (cm)	1.27	1.27
Initial Fill Gas Pressure (kPa)	300 [21]	300 [21]
Active Fuel Axial Length (cm)	370.79	370.79
Cladding surface Arithmetic Mean Roughness (cm)	7.8e-6	7.8e-6
Fuel Pellet Surface Arithmetic Mean Roughness (peak to average) (cm)	3.3e-5	3.3e-5
Number of Turns in Plenum Spring	100	100
Cladding Type	Zircaloy-2	Zircaloy-2
Coolant Pressure (MPa)	7.13	7.13
Coolant Inlet Temperature (°C)	278.3	278.3
Average Mass Flux (kg/s/m^2)	1664	1777
Linear Heat Generation Rate (kW/m)	16.46	14.82
Cycle Length (Month)	18	18
# of Batches	4	3
Average Discharge Burnup (MWd/kg)	55.8	49.8

* The analysis for the large assembly is performed for the nominal clad thickness as well as 10 % reduced clad thickness.

10.1. Power Profile

The time dependency of the linear heat generation rate and the axial power profile of the reference and large assembly rod have been specified for a comparative study.

10.1.1. Linear Heat Generation Rate

It is assumed that the power peaking factor of the linear heat generation rate linearly decreases from 1.5 (BOL) to 0.5 (EOL) for both the reference and the large assembly rod (Figure-10.1).

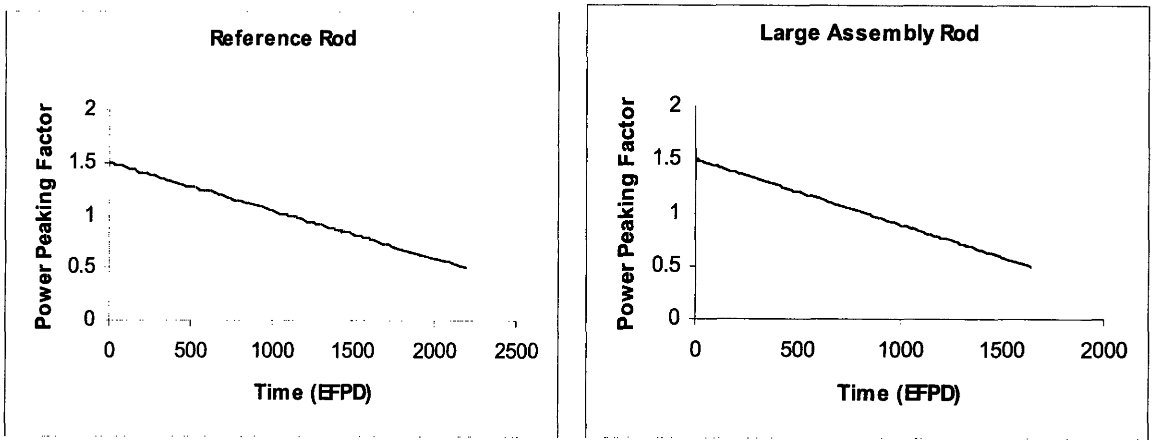

Figure-10.1: Variation of the Linear Heat Generation Rate as a Function of Time

10.1.2. Axial Power Profile

The chopped cosine power profile with a peak value at 1.1 is assigned for this calculation (Fig. 10.2). The power profile is time independent.

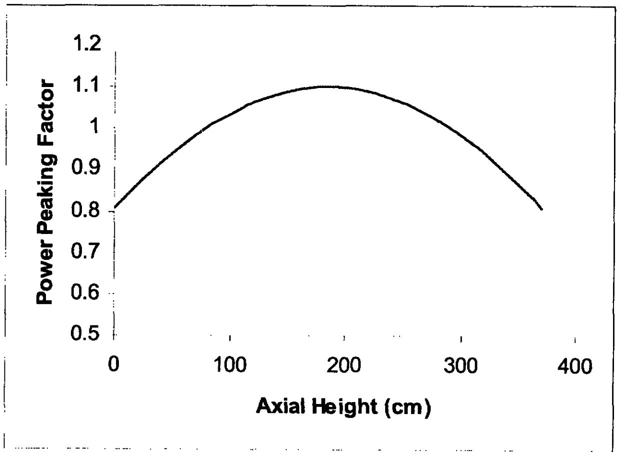

Figure-10.2: Axial Power Profile

These assumptions ensure that the correct values of the average and peak discharge burnup are obtained.

10.2. Fast Flux Factor

To model the irradiation behavior, the fast flux per unit specific power (n/(m^2s)/(W/g)) is needed. The profile given in a typical BWR input file obtained from the FRAPCON webpage [22] is used for both reference and large assembly rods (Fig. 10.3).

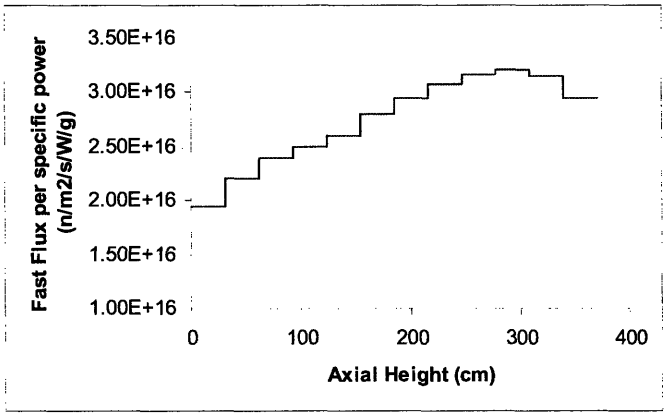

Figure-10.3: Fast Flux Factor

10.3. Results

The results are given for the reference and the large assembly fuel rod. Again note that the large assembly fuel rod is examined for the nominal as well as 10 % reduced clad thickness.

10.3.1. Peak Node Fuel Centerline Temperature

The peak node fuel centerline temperature history is shown in Figure-10.4. The centerline temperature drops smoothly, as it is roughly proportional to the linear heat generation rate. The centerline temperature in the large assembly pin is somewhat lower than in reference assembly pin, due to the lower linear heat generation rate.

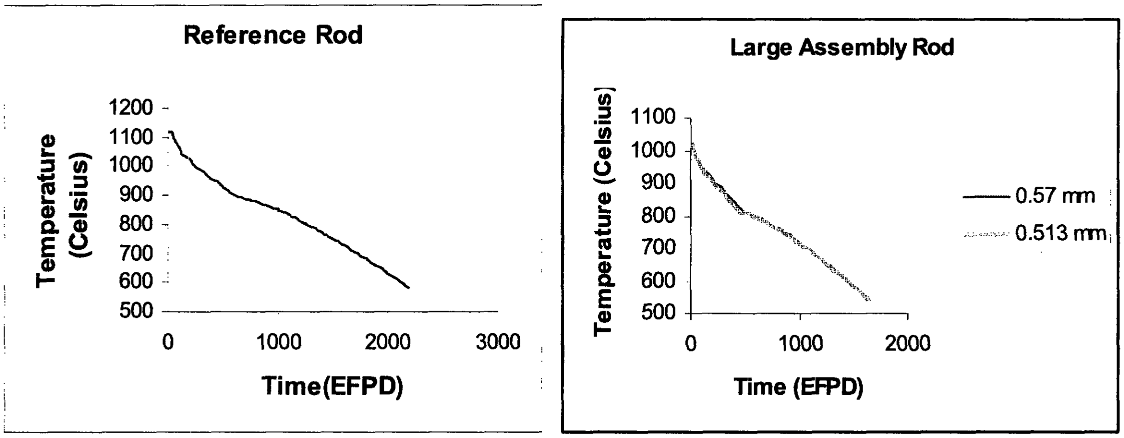

Figure-10.4: Peak Node Fuel Centerline Temperature for the Reference and Large Assembly Rods

10.3.2. Variation of the Fuel Pellet Radius for the Peak Node

The fuel pellet radius varies as a function of time due to the effect of fuel thermal expansion, densification, relocation and swelling. The overall effect tends to increase fuel pellet radius. The same trend is observed for reference (Figure-10.5) as well as the large assembly (Figure 10-6 and Figure-10.7).

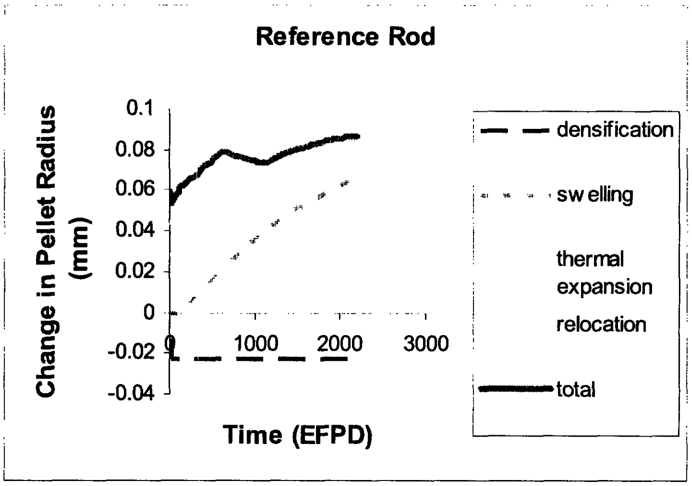

Figure-10.5: Variation of the Reference Fuel Pellet Radius as a Function of Time

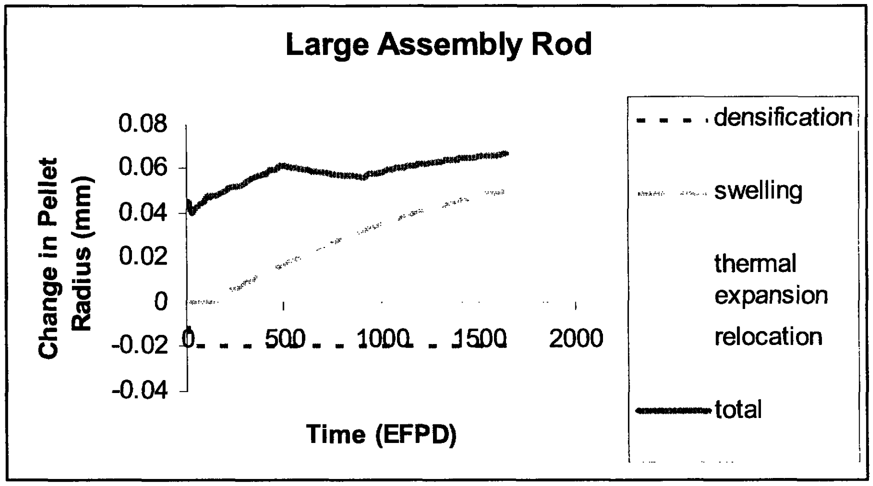

Figure-10.6: Variation of Fuel Pellet Radius of the Large Assembly as a Function of Time (Nominal Clad Thickness)

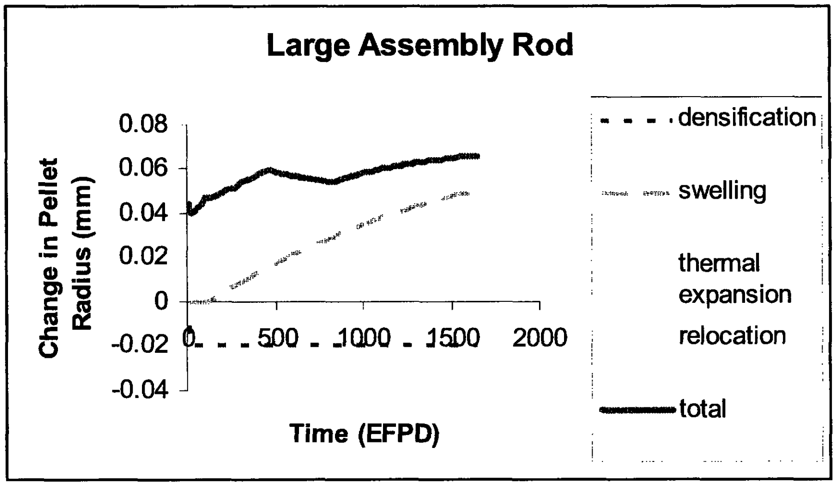

Figure-10.7: Variation of Large Assembly Fuel Pellet Radius as a Function of Time (10 % Reduced Clad Thickness)

10.3.3. Plenum Gas Pressure

The plenum pressure is 300 kPa for the fresh cold fuel at the beginning of life. Due to fuel heat up, it doubles initially and smoothly increases because of the fission gas release. Figure-10.8 shows the variation of the plenum pressure as a function of time. Due to the lower discharge burnup, the end of life pressure of the large assembly rod is 10 % lower than the reference rod. Furthermore, reducing the clad thickness of the large assembly does not affect the plenum gas pressure appreciably.

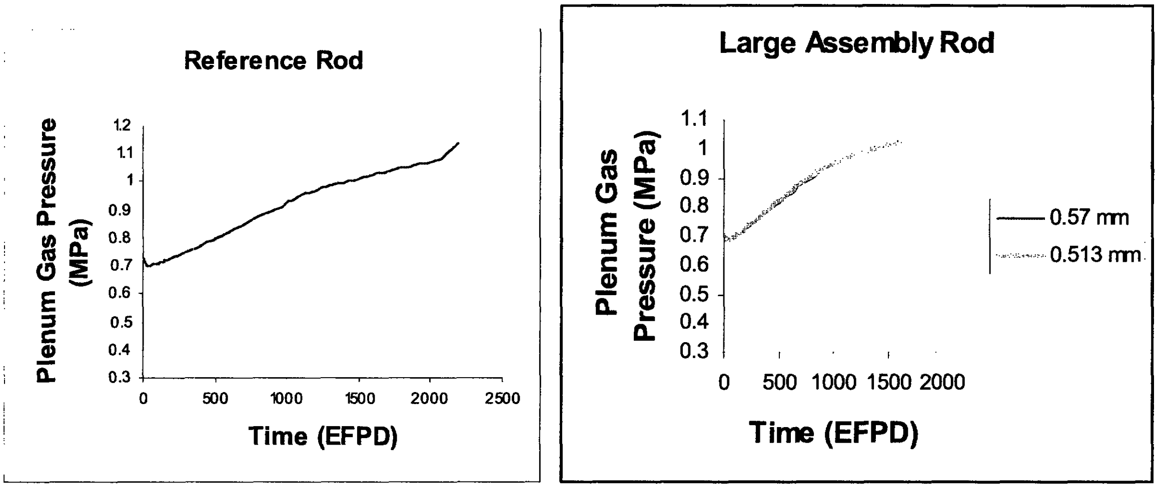

Figure-10.8: Plenum Gas Pressure for the Reference and Large Assembly Rods

10.3.4. Fission Gas Release

Fission gas release (Figure-10.9) at the end of cycle is 0.5 % for the reference rod and 0.35 % for the large assembly rod. The difference is related to the lower discharge burnup of the large assembly and its lower fuel temperature. Fission gas release normally shows strong dependence on power history. The absolute value of the fission gas release is found to be lower than current practices due to the simplified power history (Figure-10.1 & Figure-10.2).

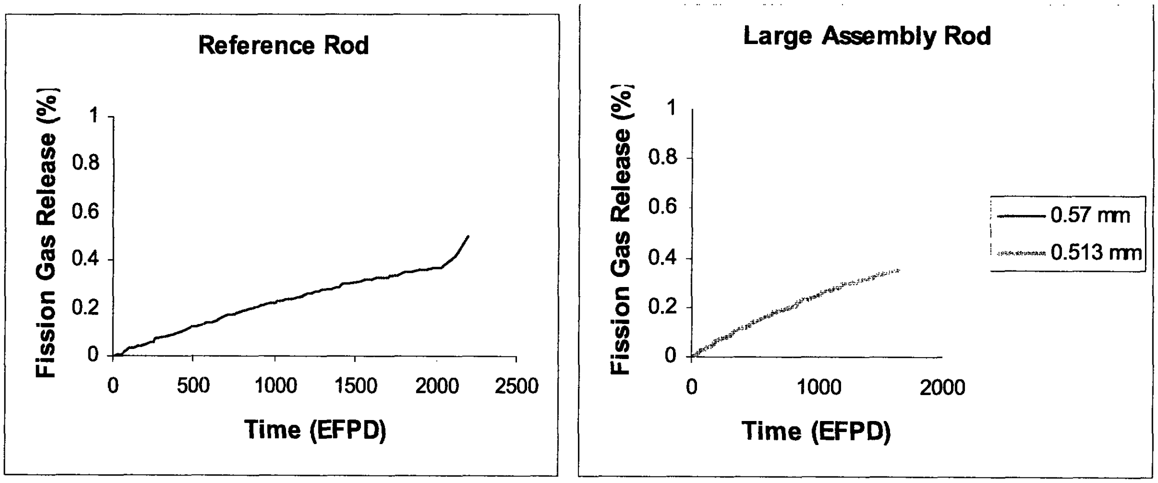

Figure-10.9: Fission Gas Release as a Function of Time for the Reference and Large Assembly Rods

10.3.5. Peak Node Clad Hoop Stress

Since the internal pressure is low at the beginning of cycle, the hoop stress is compressive due to the high external coolant pressure.

Figure-10.10 shows the variation of the peak node hoop stress as a function of time. Due to higher specific power (higher burnup), contact occurs earlier in large assembly rod. Obviously, the 10 % reduced clad thickness tends to further increase the clad hoop stress for the large assembly.

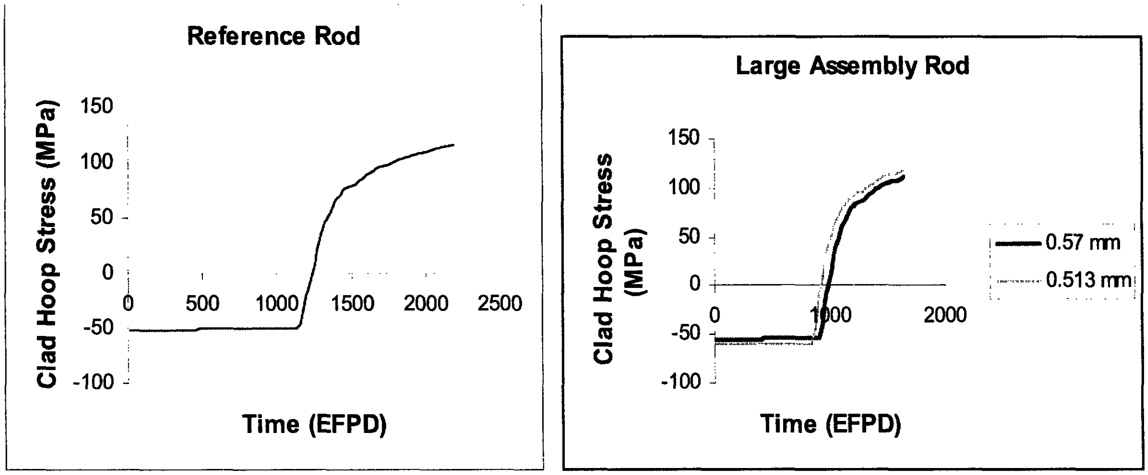

Figure-10.10: Peak Node Clad Hoop Stress as a Function of Time for the Reference and Large Assembly Rods.

10.3.6. Peak Node Pellet Clad Contact Pressure

Peak pellet-clad contact for the large rod with nominal clad thickness occurs sooner than the reference rod (Figure-10.11). As a consequence, the time to contact is directly proportional to specific power (burnup), which is the expected trend. Pellet-clad contact for the large assembly rod with 10 % reduced clad thickness occurs even sooner due to higher hoop stress.

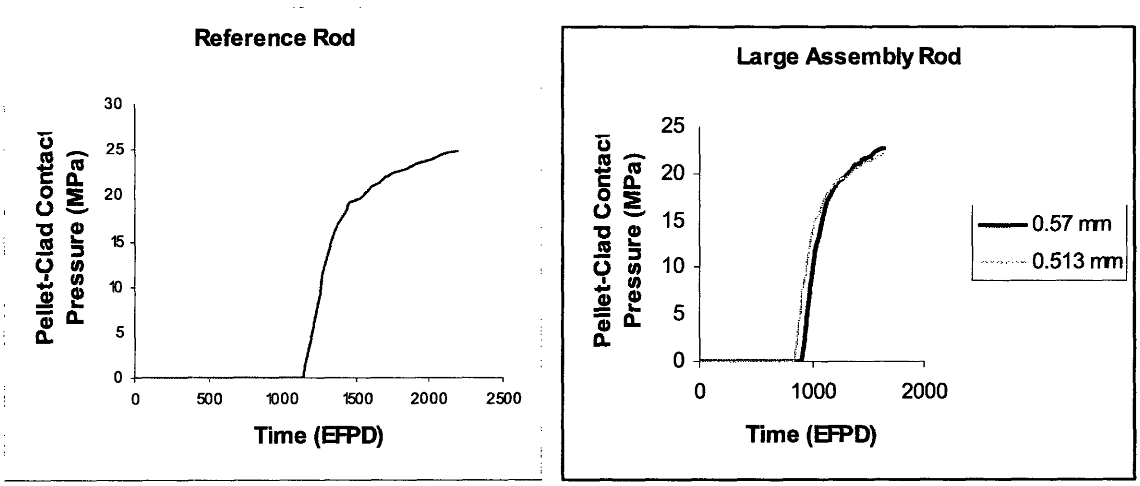

Figure-10.11: Pellet-Clad Contact Pressure for the Reference and Large Assembly Rods

10.3.7. Peak Node Clad Hoop Strain

Figure-10.12 shows the peak clad hoop strain as a function of time for the reference and the large assembly rods. Before pellet-clad contact, the clad hoop strain increases in negative direction. With pellet-clad contact, the hoop strain decreases. Note that the clad hoop strain remains well below the NRC-recommended 1% limit throughout the cycle.

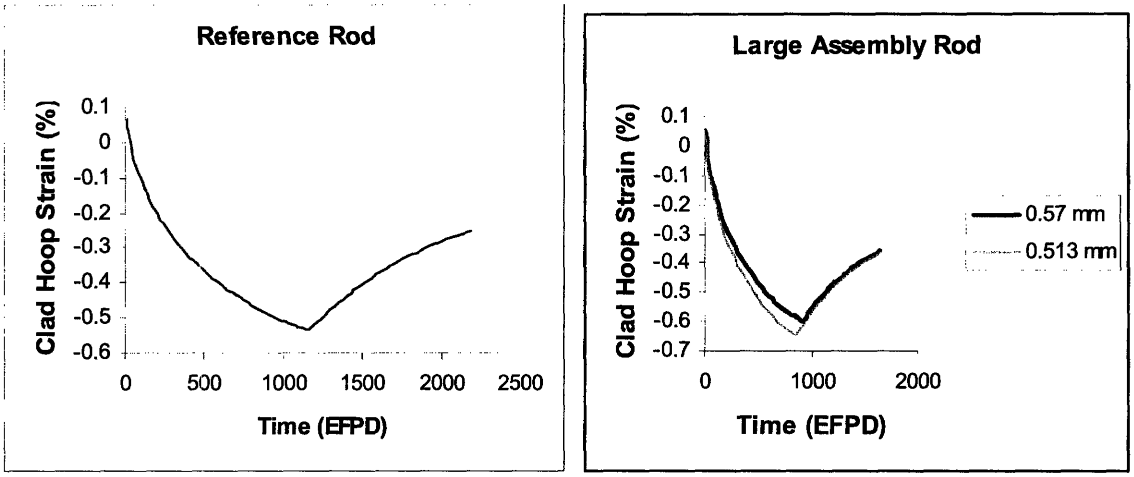

Figure-10.12: Peak Node Hoop Stress for the Reference and Large Assembly Rods.

10.3.8. Peak Node Gap Conductance

The gap conductance mainly follows the fuel pellet radius variation (Figure-10.5, 10.6 and 10.7). A rapid increase in fuel conductance is observed with pellet clad contact (Fig. 10.13).

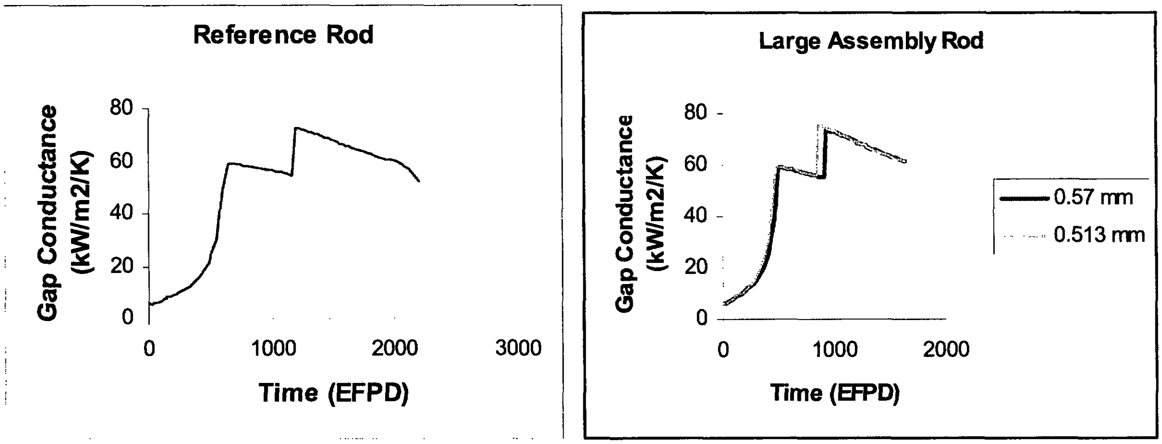

Figure-10.13: Variation of the Peak Node Gap Conductance as a Function of Time for the Reference and the Large Assembly

10.3.9. Peak Node ZrO_2 Thickness on the Clad Outer Surface

As can be seen in Figure-10.14, the oxide thickness on the clad increases smoothly. The end of life oxide thicknesses are given in Table-10.2 as a percent of the as-manufactured clad thickness. Reducing the large assembly clad thickness by 10 % results in a higher percentage of oxide film at the end of life.

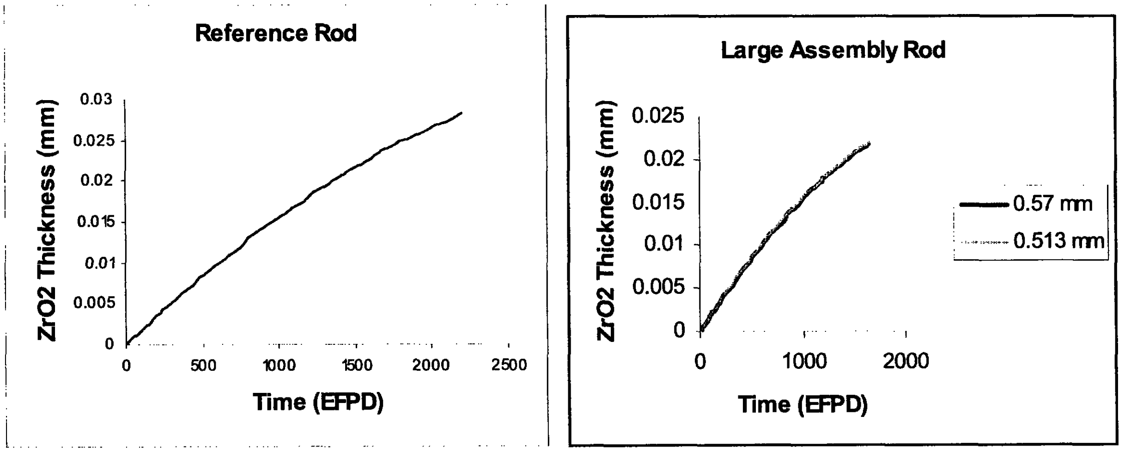

Figure-10.14: Peak Node ZrO_2 Thickness as a Function of Time for the Reference and Large Assembly Rods

Table-10.2: Percent Oxide Thickness at the End of Life for the Reference and the Large Assembly Rods

Rod Type	The oxide thickness (%)
Reference Rod	4
Large Assembly Rod with the Nominal Clad Thickness	3.8
Large Assembly Rod with 10 % Reduced Clad Thickness	4.3

10.3.10. Peak Node Hydrogen Formation

A fraction of the hydrogen liberated by the metal water corrosion reaction is absorbed locally by the cladding. The resulting hydrogen concentration in the clad is shown in Figure-10.15. Table-10.3 shows the end of life values of the clad hydrogen concentration. The reference and large assembly rod with nominal thickness have close end of life hydrogen concentration; whereas, the large assembly rod with 10 % reduced thickness has 7% higher hydrogen concentration than the reference rod. As a consequence, 10 % reduction in clad thickness may cause a reduction in ductility of the large assembly clad, which is undesirable.

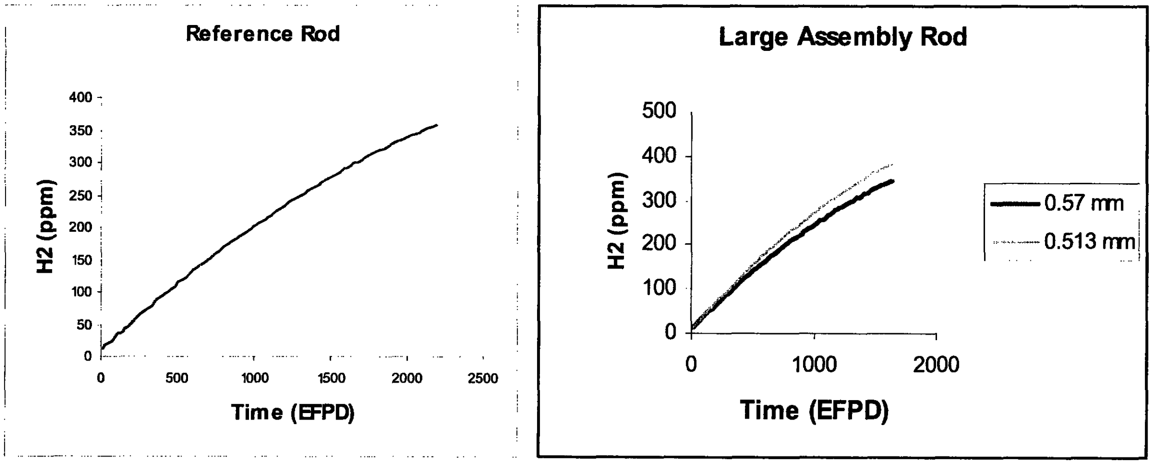

Figure-10.15: Variation of the Hydrogen Concentration as a Function of Time for the Reference and Large Assembly Rods

Table-10.3 Hydrogen Concentration at the End of Life for the Reference and the Large Assembly Rods

Rod Type	Hydrogen Concentration (ppm)
Reference Rod	359
Large Assembly Rod with the Nominal Clad Thickness	346
Large Assembly Rod with 10 % Reduced Clad Thickness	385

10.4 Conclusions

The thermo-mechanical analysis of the fuel pin performed with the FRAPCON code has shown that the reference and the large assembly fuel rod with nominal thickness exhibit very similar behavior.

Reducing the clad thickness of the large assembly fuel rod may cause an earlier pellet clad contact due to higher hoop stress. Moreover, the percentage of the oxide thickness on the clad outer surface as well as the hydrogen concentration becomes higher than the reference case, which is undesirable. The vibration ratio of the new design with 10 % reduced clad thickness is also 8 % higher. The subchannel analysis was repeated for the design with 10 % reduced clad thickness and showed that 21 % power uprate (vs. 20% for the large assembly with nominal clad thickness) is possible. It is concluded that reducing the clad thickness gives only marginal power density increase, but could compromise the thermo-mechanical behavior of the clad. Thus, this option was discarded.

11. CONCEPTUAL MECHANICAL DESIGN FOR THE LARGE BWR ASSEMBLY

In traditional BWR fuel assemblies the main structural element is the assembly duct, to which the fuel rod spacers and the tie plates are fastened. This approach may not work well for the new much heavier and larger assembly design, as the duct perimeter is larger, but the thickness is the same. So a different approach should be implemented. The 25 water rods in each assembly (Figure-11.1), fastened to the lower and upper tie plates, become the main structural element of the fuel assembly. The fuel rod spacers are fastened to the water rods which prevents lateral motion of the fuel rods. The fuel rods are fastened to the lower tie plate, but not to the upper tie plate, to prevent excessive stresses from differential axial expansion of the fuel and water rods, which operate at different temperatures. The assembly duct is fastened to the lower tie plate, and its lateral motion is prevented by dimples on the fuel rod spacers, and axial sliding keys on the upper tie plate. The fuel assembly handle, which is used to raise, shuffle and lower the fuel during refueling, is fastened to the upper rim of the assembly duct. The water rods extend below the lower tie plate, to receive the finger-type control rods. A schematic view of the fuel assembly cross-section is shown in Figure-11.3.

The new fuel assembly is supported laterally by the core plate and top fuel guide plate. Vertical support is provided by a fuel assembly support duct (control rod guide tube), which ultimately sits on the bottom of the RPV. Note that this approach is also used to support 2x2 clusters of fuel assemblies in current BWR plants [23] (Figure-11.2). The thick duct is properly perforated and orificed to obtain the desired coolant flow into the assembly. The control rods are supported laterally by ring spacers fastened to the fuel assembly support duct. Refueling could be conducted according to the following steps:

- With the reactor at cold shutdown conditions, the control rods are extracted from the fuel assembly to be shuffled, while all other control rods remain inserted to maintain sub criticality
- The fuel assembly is disengaged from the fuel assembly support duct

- The fuel assembly is lifted and taken away by the refueling machine
- The new fuel assembly is brought in and lowered in position by the refueling machine
- The control rods are re-inserted

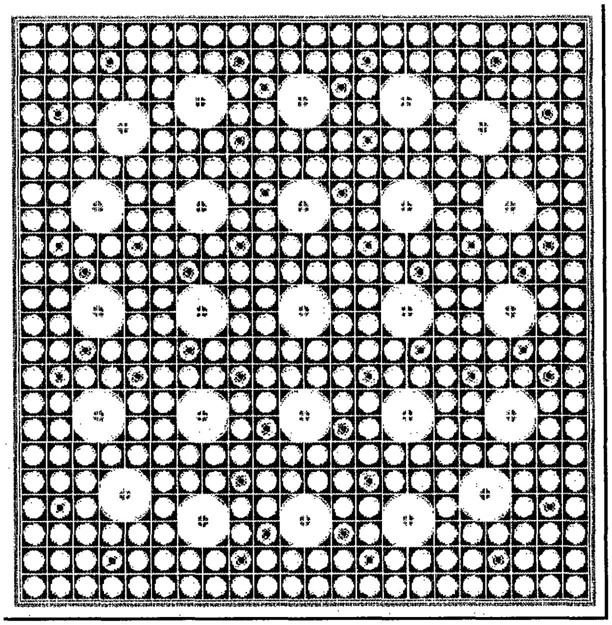

Figure-11.1: The Large Assembly

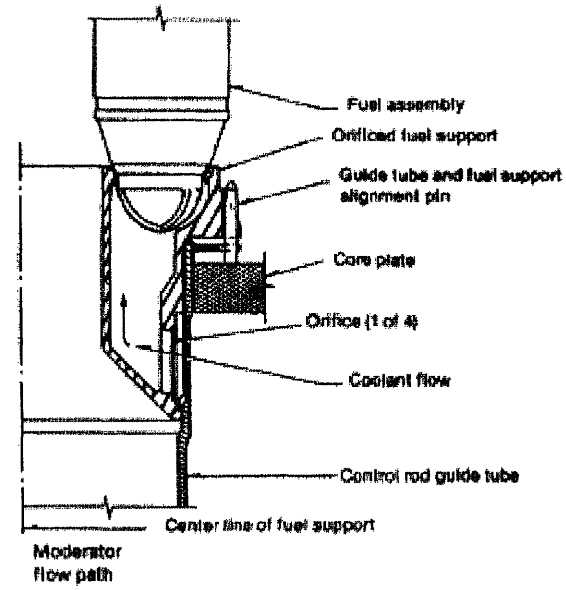

Figure-11.2: Bottom Fuel Support Pieces of a Typical BWR Assembly [23]

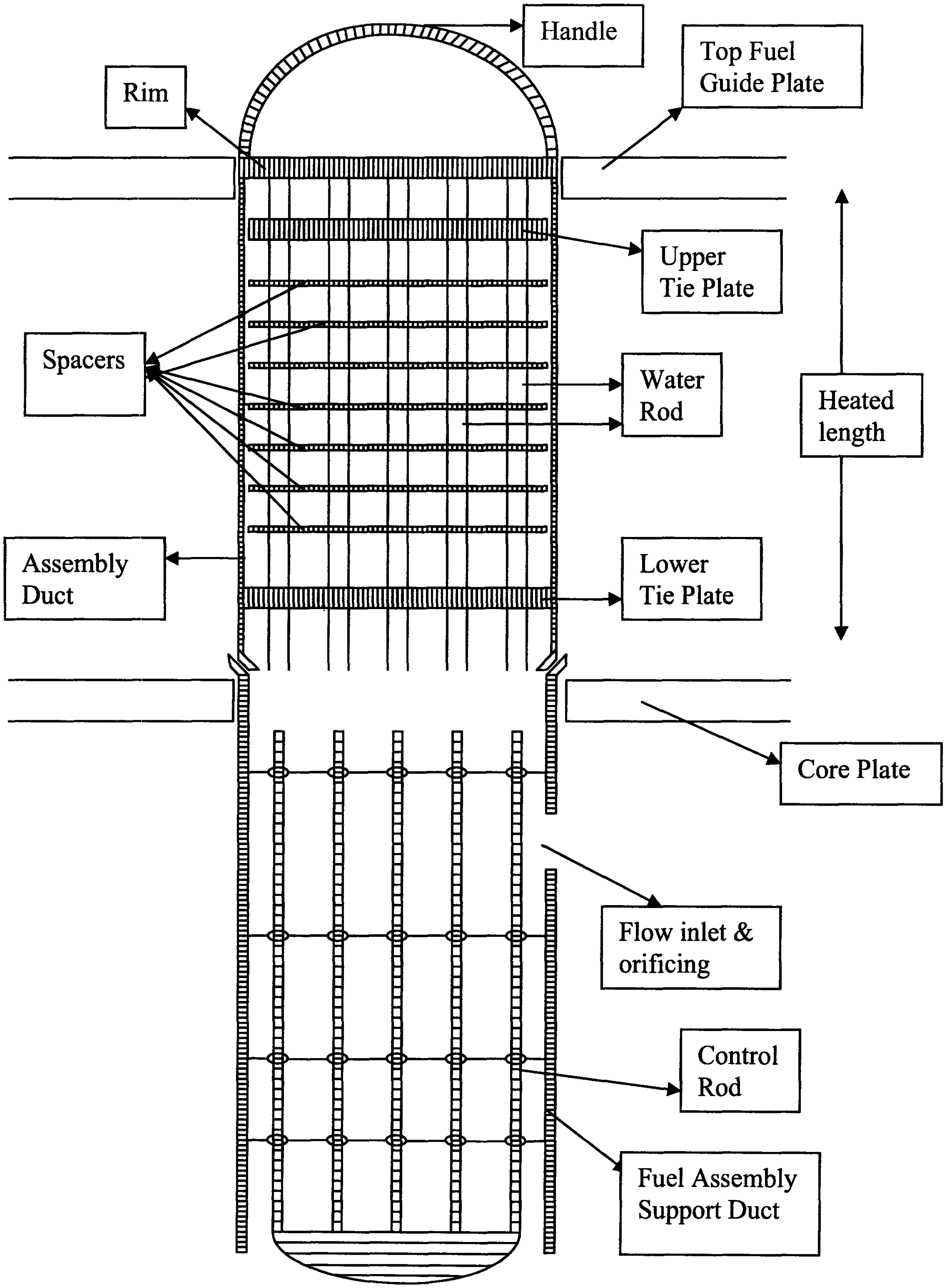

Figure-11.3: Fuel Assembly Components (Fuel Rods are not shown and the figure is not scaled)

11.1. Spacer Design

Traditional grid spacer design used in light water reactors is the most promising candidate for the large assembly. The fuel rods are supported by the dimples and the springs on the spacers, as shown in Figure-11.4. In the large assembly concept each spacer is circumferentially welded to the water rods.

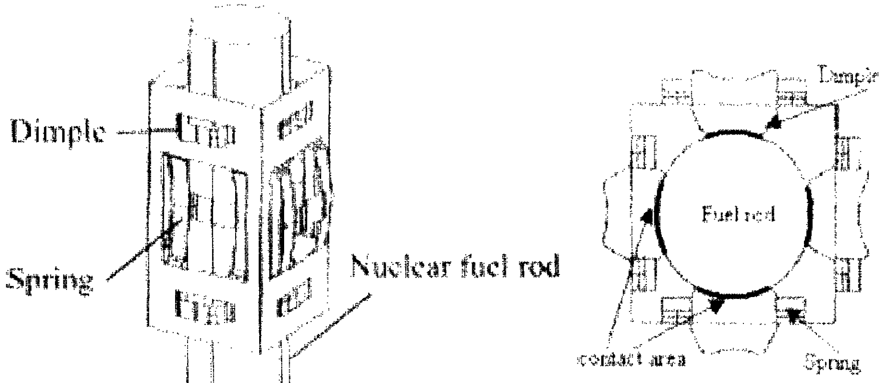

Contact between a nuclear fuel rod and a spring

Figure-11.4: Unit Spacer Grid Structure [24]

11.2. Upper Tie Plate

Upper tie plate is circumferentially welded to the water rods (Figure-11.5). Dimples between the upper tie plate and the assembly duct eliminate lateral movements whereas axial movements are allowed, thus effectively forming an axial sliding key.

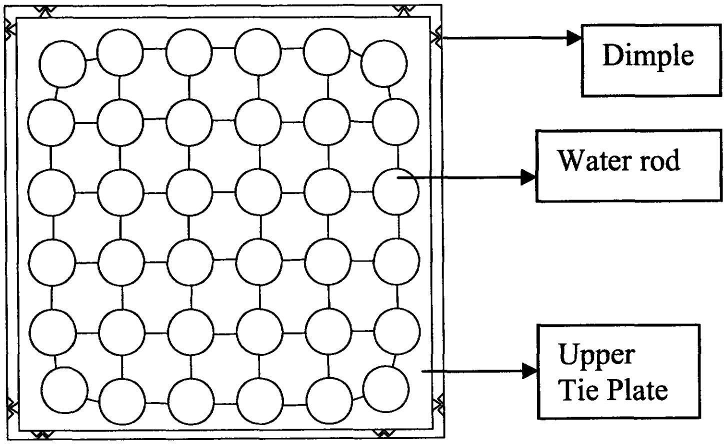

Figure-11.5: The Upper Tie Plate

11.3. Lower Tie Plate

All water rods, fuel rods and assembly duct are fastened to the lower tie plate (Figure-11.6).

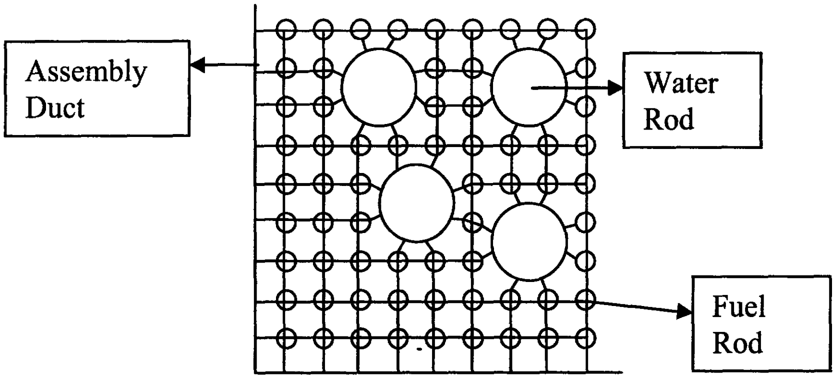

Figure-11.6: The Lower Tie Plate (Lower left corner of the Large Assembly)

11.4. Independent Review of Structural Design of the Large Fuel Assembly

The structural design described in the sections above was reviewed by a nuclear fuel expert [25]. A summary of the comments are provided as follows:

1- Using the water rods as the main structural element of the fuel assembly is a viable approach, as it was successfully used in Combustion Engineering PWR fuel assemblies in the past.

2- The high weight of the new assembly will force replacement of some components of the refueling machine system at existing plants. The expense is quantified in the range of $5-10M per plant.

3- The small fuel pins should not pose particular vibration challenges, provided the typical number of spacers is used (i.e., one spacer per foot). Note that the fuel pin size is not very different from that of fuel pins in current 10x10 assemblies.

4- The 10-mm inter-assembly gap should be sufficient to prevent contact due to bowing/swelling of the duct, especially since the control rods are no longer in the gap. However, distortion of the water rods within the fuel assembly may prevent the thin control rods to get properly inserted. This is an issue also in PWRs.

5- The somewhat higher pressure drop in the core may exacerbate assembly lift-off concerns, which can be accommodated by a redesign of the upper core plate. The upper core plate will have to be replaced anyway due to the change in fuel assembly geometry.

6- Thin stainless steel sleeves should be used in the water rod section below the active region. This is to prevent fretting erosion when the control rods are sitting there during normal operation. Such sleeves (made of high-chrome stainless steel) are currently used also in the PWR control rod guide tubes.

7- The approach to provide vertical support for the fuel assemblies is already used in current BWRs for 2x2 clusters of fuel assemblies.

12- COMPARISON BETWEEN MIT LARGE FUEL ASSEMBLY AND ABWR-II ASSEMBLY

The next generation Advanced Boiling Water Reactor-II (ABWR-II) has been under development in Japan for more than a decade by TEPCO, three BWR vendors, i.e., Hitachi, Toshiba and GE, and a BWR fuel vendor, GNF. Recently, a comparative study between typical 9×9 assembly and ABWR-II assembly has been performed [26]. In this chapter, the main features of ABWR-II and MIT Large Fuel Assemblies are compared.

12.1. ABWR-II Design

Main Design Objectives

- Achieve 15 % power density uprate while keeping the same safety margin as the current core design
- Achieve enough flexibility for future high burnup and longer cycle operation
- Reduce the number of fuel assemblies to simplify and shorten refueling outages

To meet the above requirements, a 1.5 times larger fuel bundle design with a K-Lattice control rod pattern was selected (Figure-12.1). This design has a large area inside the channel box and has potential for increasing the number of fuel rods to support power density uprating. The size of the K-lattice control rods was selected to ensure sufficient cold shutdown margin [27].

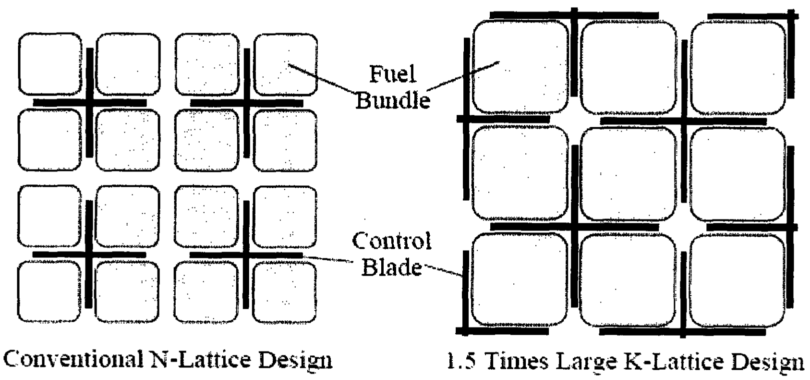

Figure-12.1: Comparison of the Traditional and ABWR-II Control Rod Pattern [27]

12.2. A Comparison of the MIT Fuel Assembly (MIT FA) and the ABWR-II Fuel Assembly (ABWR-II FA)

Table-1 shows the main design parameters for the ABWR-II and MIT Fuel Assemblies. The ABWR-II assembly data are obtained from Reference [26].

Table-12.1: Comparison of the Major Design Specifications between ABWR-II and MIT FA

Item	ABWR-II	MIT Large Assembly
Average Core Power Density (kW/l)	58.1	60.6
Specific Power (kW/kg)	26.1	29.9
Fuel Bundle Pitch (cm)	23.3	30.48
Active Core Height (cm)	371	371
Fuel Bundle Outer Width (cm)	21.4	29.48
Number of Fuel Rods per Assembly	224	384
Fuel Rod Outer Diameter (cm)	1.03	0.96
Void Coefficient with respect to reference 9×9 assembly	24 % higher	25 % higher
H/HM with respect to 9×9 assembly	20 % lower	Same

- The MIT FA and ABWR-II FA have higher power density than traditional reference FA, but the MIT FA power density is somewhat higher (+20% vs. +15%)
- The MIT FA has finger-type CRs, while ABWR-II has large cruciform CRs with K-type lattice to maintain acceptable shutdown margin.
- Retrofit of existing plants with MIT FAs should be simpler than with ABWR-II FAs because the number and location of the control rods are not changed.
- The higher specific power of the MIT FA design should result in somewhat lower fuel cost.
- The MIT FA maintains the same H/HM of the traditional FA while the ABWR-II FA has a harder spectrum due to the increased heavy metal inventory. The harder spectrum will result in higher fluence on the structural components.
- Both FA concepts have higher void reactivity coefficient, but for different reasons. That is, in the MIT FA the higher void reactivity coefficient is due to the larger coolant flow area, while in the ABWR-II FA the larger void reactivity coefficient is due to the harder spectrum. A more negative void coefficient results in lower

margin for thermalhydraulic stability for both the ABWR-II FA concept [28] and the MIT FA concept (see Chapter 6).

- The ABWR-II FA uses Spectral Shift Rods (SSRs) [26] for reactivity control, while the MIT FA does not (but could, if proven advantageous)
- The MIT FA is heavier than the ABWR-II FA.
- The ABWR-II FA has internal partitions, while the MIT FA does not. Partitions impart robustness to the FA. In the MIT FA the water rods are the main structural element, not the FA duct, so partitions in principle are not needed (see Chapter 11). However, mechanical design and manufacturability of the MIT FA should be verified.

In summary, the MIT FA and the ABWR-II FA are quite different designs, though they offer similar potential benefits in terms of power density uprate, and present similar shortcomings in terms of thermal-hydraulic stability. We note that perhaps the MIT FA is a somewhat simpler design as it maintains the number and location of the control rods, and does not require the use of Spectral Shift Rods.

13. CONCLUSIONS

Table-13.1 shows the important design and operating features of the most promising large assembly and the reference assembly.

Table-13.1 Comparison between Reference and the Most Promising Large Assembly

Parameters	**9×9 Assembly**	**The Large Assembly**
Core Power Density (kW/l)	50.5	60.6
Fuel Pellet OD (mm)	9.55	8.29
Fuel Pin OD (mm)	11.18	9.60
Clad Thickness (mm)	0.71	0.57
Fuel Pin Pitch (mm)	14.27	13.05
Active Fuel rod height (mm)	3707.9	3707.9
Total Fuel Rod height (mm)	4178.7	4178.7
Part Length Rod Height (mm)	2436	2436
Fuel Pins / Water Rods per Fuel Assembly	74/2	384/25
Number of Part Length Rods	8	12
Inner/Outer diameter of the water rods	23.37/24.89	25.64/27.16
Duct Thickness (mm)	2.54	2.54
Clearance between duct and peripheral fuel rods (mm)	3.53	3.0
Clearance between water rods and fuel rods (mm)	1.79	2.26
Assembly Outer Dimension (mm)	137.54	294.8
Inter-Assembly Gap (mm)	14.86	10.0
Average Linear Power (kW/m)	16.46	14.82
MCHFR (fresh assembly)	1.23	1.23
MCHFR (once burned assembly)	1.35	1.35
Pressure Drop (kPa)	160	187
Average enrichment (wt%)	4.31	4.02
Average Discharge Burnup (GWd/t)	55.84	49.75
Refueling scheme	4 batches	3 batches
Number of rods with gadolinia	8	44
Gadolinia concentration (wt%)	5	6
Hydrogen to Heavy Metal Ratio	4.53	4.55
Void Coefficient (pcm/% void)	-144	-180
Fuel Temperature Coefficient (pcm/K)	-1.7	-2.3
Single Channel Stability	0.12	0.12
Core-wide Decay Ratio	0.31	0.36
Vibration Ratio	0.006	0.013
Approximate Assembly Weight (kg)	281	1068

The main conclusion of this study is that 20 % power uprate is feasible with the large fuel assembly design. To maintain the reference dryout margin:

- The fuel rod surface area has been increased by 14.5 %
- The active flow area has been increased by 12.4 %, the bypass flow area has been reduced by 8.5 %.
- The flow distribution within the fuel assembly must allow for better peripheral flow by adjusting the clearance between the assembly duct and the peripheral rods, and between the water rods and the fuel rods. Furthermore, part length rods must be used effectively to reduce the steam quality in subchannels of high power and/or low flow.
- Fuel composition must be optimized to obtain satisfactory power peaking factors.

- However, the feedback coefficients in the new design are more negative. The void coefficient is 25 % more negative; whereas the fuel temperature coefficient is 35 % more negative than the reference case. The decay ratio of the new system is 16 % higher than the reference case, so the margin to two-phase instabilities is somewhat reduced. Also, the vibration ratio for the smaller fuel pins used in the large assembly is higher than the reference. Another area of potential concern is the high weight of the new fuel assembly, which may be beyond the capability of the refueling machines at current plants. The pressure drop in the uprated core is somewhat higher than in the reference core, so larger pumps will be needed. The thermo-mechanical performance of the large assembly fuel rod (e.g., fuel temperature, fission gas release, hoop stress and strain, clad oxidation) is similar to that of the reference rod. The conceptual mechanical design of the large fuel assembly suggested that the water rods and lower tie plate can be used as the main structural element of the assembly, with horizontal support being provided by the top fuel guide and core plate assembly, and vertical support being provided by the fuel support duct, which also supports the finger-type control rods.

14. RECOMMENDATIONS FOR FUTURE WORK

1- Abnormal events such as the Loss Of Coolant Accident (LOCA), the Loss Of Flow Accident (LOFA), the Loss of Heat Sink and the Anticipated Transients Without Scram (ATWS) should be analyzed for the large assembly concept to complete the thermal margin evaluation.

2- Expected cost of the fuel should be evaluated. Note that three batch refueling (33 % reload batch) is adopted for the large assembly core to satisfy 60 MWd/kg discharge burnup limit. The discharge burnup can be increased further by decreasing the reload batch size while staying within the burnup limit [1].

3- Currently, BWRs are using 10×10 fuel assemblies (Table-1.1). A comparison between the 10×10 assembly and the large assembly should be performed.

4- Thermalhydraulic stability analysis should be extended to BWR power flow operation range.

APPENDIX-A: Comparison of Critical Power Experiments to Correlations

To select the dryout correlation used in this project, the critical power experiments performed by the Nuclear Power Engineering Center (NUPEC) were analyzed [29]. VIPRE was used to test the Hench-Gillis critical quality correlation and the EPRI-Columbia critical heat flux correlation.

The NUPEC experiments were performed for an electrically heated 9x9 BWR fuel assembly with the following geometry and operating conditions:

Operating Pressure: 7.2 MPa
Inlet Subcooling: from 25 kJ/kg to 126 kJ/kg
Flow rate: from 30 to 60 t/h
Heated rod diameter: 3587.5mm
Pitch: 14.27 mm
Number of full length heated rods: 66 (length= 3.5875 m)
Number of part length fuel heated rods: 8 (length=2.242 m).
The axial power profile for the full-length heated rods is shown in Figure A.1.
The axial profile for the part-length heated rods is the same up to the length of the rods and then drops to zero.

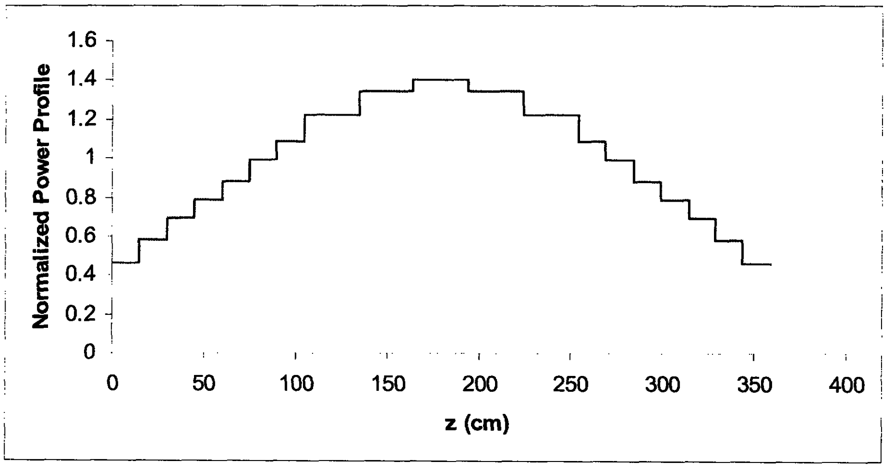

Figure A.1: Axial Power Profile of Each Rod

A.1. Hench-Gillis Correlation

The Hench-Gillis (EPRI-2) correlation is as follows:

$$x_c = \frac{AZ}{B+Z}(2\text{-}J) + F_p$$

where $A = 0.50G^{-0.43}$

$B = 165 + 115G^{2.3}$

with G= mass flux, Mlbm/hr-ft^2

$$Z = \frac{\text{boiling heat transfer area}}{\text{bundle flow area}} = \frac{\pi D_r n L_B}{A_f}$$

with D_r = rod diameter

n = number of active rods in the bundle

L_b = boiling length

Pressure correction factor

$$F_p = 0.006 - 0.0157\left(\frac{P\text{-}800}{1000}\right) - 0.0714\left(\frac{P\text{-}800}{1000}\right)^2$$

The J-factor accounts for the local peaking in the bundle, and is defined as follows:

for corner rods-

$$J = J_1 - \frac{0.19}{G}(J_1 - 1)^2$$

for side rods-

$$J = J_1 - \frac{0.19}{G}(J_1 - 1)^2 - \left(\frac{0.07}{G+0.25} - 0.05\right)$$

for central rods-

$$J = J_1 - \frac{0.19}{G}(J_1 - 1)^2 - \left(\frac{0.14}{G+0.25} - 0.10\right)$$

J_1 is a weighted factor depending on the relative power factors, f_n, of the rods surrounding a given rod. Rods are weighted differently if they are in the same row (column) as a rod, or diagonally adjacent. The J_1 factors are calculated as follows;

for corner rods-

$$J_1 = \frac{1}{16}[12.5f_p + 1.5\sum_{i=1}^{2} f_i + 0.5f_j] - \frac{nP(2S+D\text{-}P)}{64A}[4f_p + \sum_{i=1}^{2} f_i]$$

for side rods-

$$J_1 = \frac{1}{16}[11.0f_p + 1.5\sum_{i-1}^{2} f_i + f_k + 0.5\sum_{j-1}^{2} f_j] - \frac{nP(2S+D\text{-}P)}{64A}[2f_p + \sum_{i-1}^{2} f_i]$$

for central rods-

$$J_1 = \frac{1}{4}[2.5f_p + 0.25\sum_{i-1}^{4} f_i + 0.125\sum_{j-1}^{4} f_j]$$

where f_p = radial power factor for a given rod

f_i = radial power factor of rod adjacent to rod p in the same row or column

(not including the rod adjacent to rod p in the same column, if p is a side rod)

f_j = radial power factor of rod adjacent to rod p on a diagonal line is the matrix

f_k = radial power factor of the rod adjacent to rod p and opposite the wall when p is a side rod.

(The weighted summations of the rod power factors for corner and central rods do not include a k-rod.)

n = number of rods and water tubes in the fuel bundle

P = rod pitch

S = rod-to-wall gap

A = total flow area in the bundle

D = fuel pin diameter

The Hench-Gillis (EPRI-2) is a critical quality or power ratio (CPR) correlation. The correlation uses the bundle average mass flux, power profile and quality axial distribution. The effect of local non-uniformities is accounted for via the so-called J1 factors. The maximum J1 factor is used by the correlation to calculate the critical power.

Because the 9×9 assembly has part length rods, some modifications have been performed to capture the effect of part length fuel rods. The "Compressed Geometry" option of VIPRE has been used to account for those modifications.

For use in a single-channel approach, the power profile has to be modified to account for the presence of the part length rods. Using the energy balance it is easy to demonstrate that the power per unit length is:

$$Q'(z)=\begin{Bmatrix} \dfrac{N_L+N_P}{N_L+f_p\times N_P}\dfrac{\dot{Q}}{L}P(z) \;\; \text{for } z<L_{part} \\ \dfrac{N_L}{N_L+f_p\times N_P}\dfrac{\dot{Q}}{L}P(z) \; \text{for } z>L_{part} \end{Bmatrix}$$

where

N_L = # of full lenth rods;
N_P =# of part lenth rods;
P(z)= Power profile from Figure A.1;
$\dot{Q}$= Bundle Power ;
$f_p=\frac{1}{L}\int_0^{L_{part}} P(z)dz$

The resulting bundle average power profile is shown in Figure A.2. The local power peaking factors used in the NUPEC experiments are shown in Figure A.3.

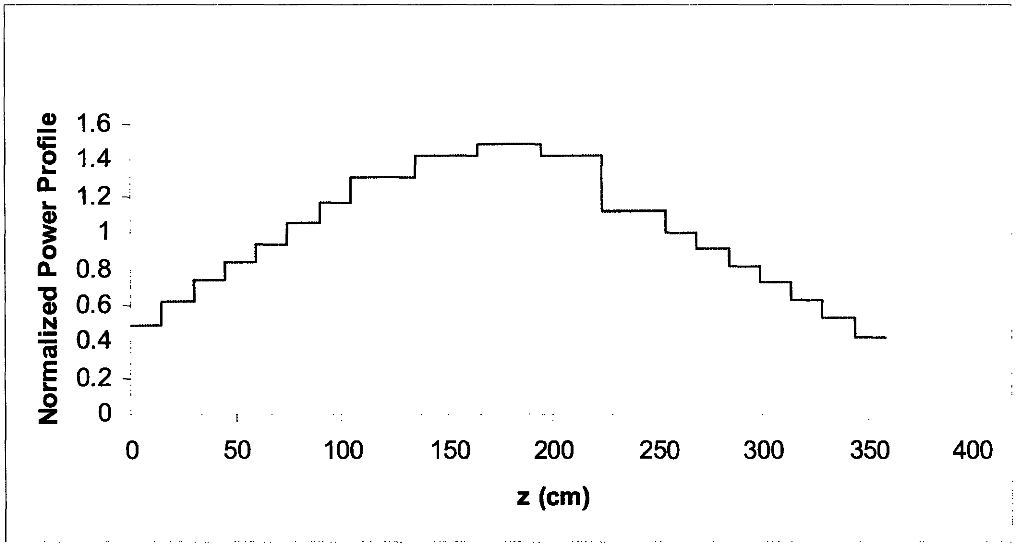

Figure A.2: Bundle Average Axial Power Profile

1.20	1.20	1.20	1.38	1.38	1.38	1.20	1.20	1.20
1.20	0.77	1.05	0.49	0.77	1.20	0.49	0.77	1.20
1.20	1.05	0.49	1.05	0.49	1.20	1.05	0.49	1.20
1.38	0.49	1.05	1.05	0	0	0.49	1.05	1.20
1.38	0.77	0.49	0	0	0	1.20	0.77	1.20
1.38	1.20	1.20	0	0	1.20	0.49	1.05	1.20
1.20	0.49	1.05	0.49	1.20	0.49	1.05	0.49	1.20
1.20	0.77	0.49	1.05	0.77	1.05	0.49	0.77	1.20
1.20	1.20	1.20	1.20	1.20	1.20	1.20	1.20	1.20

Figure A.3: Local Power Peaking Factors

The flow area and thus the mass flux are also modified in the upper part of the bundle to capture the effect of the fewer rods.

The results of the comparison between the experiments and the Hench-Gillis correlation predictions are shown in Tables A.1 and A.2. The Hench-Gillis correlation systematically underpredicts the critical power with an average error of nearly 22 % over the range of flow rates and inlet subcooling considered. Therefore, it is too conservative.

Table A.1: Comparison between experimental and predicted critical power with the Hench Gillis Correlation at low inlet subcooling

A- Inlet Subcooling: 25 kJ/kg

Flow rate (t/h)	Predicted Critical Power (MW)	Experimental Critical Power (MW)	% Relative Error
30	4.975	6.400	22.3
40	5.555	7.300	23.9
50	5.935	8.200	27.6
60	6.179	8.700	29.0

Table A.2: Comparison between experimental and predicted critical power via Hench Gillis Correlation at high inlet subcooling

B- Inlet Subcooling: 126 kJ/kg

Flow rate (t/h)	Predicted Critical Power (MW)	Experimental Critical Power (MW)	% Relative Error
30	5.580	7.200	22.5
40	6.316	8.000	21.1
50	6.849	8.700	21.3
60	7.197	9.300	22.6

A.2 Subchannel Analysis for Critical Power Calculation with EPRI-Columbia Correlation

EPRI-Columbia Correlation is as follows:

$$q''_{CHF} = \frac{AF_A - x_{in}}{C(F_C + F_g) + \left[\frac{x - x_{in}}{q''_L}\right]}$$

where $A = P_1 P_r^{P_2} G^{[P_6 + P_7 P_r]}$

$C = P_3 P_r^{P_4} G^{[P_6 + P_8 P_r]}$

$q''_L =$ local heat flux (MBtu/hr-ft^2)

$x =$ local equilibrium quality

$x_{in} =$ inlet quality; $[(h_{inlet} - h_f)/h_{fg}]$

$G =$ local mass velocity, Mlbm/hr-ft^2

$P_r =$ critical pressure ratio; system pressure/critical pressure

$F_A = G^{0.1}$ (Cold Wall Correction Factor)

$F_C = 1.183G^{0.1}$ (Cold Wall Correction Factor)

$F_g = 1.3 - 0.3C_g$

$C_g =$ Grid loss coefficient

Optimized Constants:

$P_1 = 0.5328$ $P_5 = -0.3040$
$P_2 = 0.1212$ $P_6 = 0.4843$
$P_3 = 1.6151$ $P_7 = -0.3285$
$P_4 = 1.4066$ $P_8 = -2.0749$

Unlike the Hench-Gillis correlation, the EPRI-Columbia correlation is a critical heat flux correlation that accounts for the local effects directly if used in concert with a subchannel analysis. Therefore, a subchannel analysis has been performed to obtain the critical power.

1- The exact axial power profiles for full length fuel rods as well as part length fuel rods are modeled.

2- Part length fuel rods are modeled via the "Axial Variation Card", i.e., the flow area, gap and wetted perimeter of the subchannels corresponding to the part length rods are modified in the upper region of the core, to simulate the absence of rods there.
3- The local power peaking factors are entered for each rod. (Figure A.3.)
4- The cold wall correction factor and grid loss coefficient are accounted for. The grid loss coefficient is assumed to be 1.2.
5- As the VIPRE manual recommends, the non-uniform axial neutron flux correction factor, while available, is not used with the EPRI-Columbia correlation.

The results of the comparison between the experiments and the EPRI-Columbia correlation predictions are shown in Tables A.3 and A.4. The EPRI-Columbia also under-predicts the critical power, but with a significantly lower error of about 5-15%.

Table A.3: Comparison between experimental and predicted critical power via EPRI-Columbia Correlation at low inlet subcooling

A- Inlet Subcooling: 25 kJ/kg

Flow rate (t/h)	Predicted Critical Power (MW)	Experimental Critical Power (MW)	% Relative Error
30	5.419	6.400	15.3
40	6.445	7.300	11.7
50	7.225	8.200	11.9
60	7.837	8.700	9.92

Table A.4: Comparison between experimental and predicted critical power via EPRI-Columbia Correlation at high inlet subcooling

B- Inlet Subcooling: 126 kJ/kg

Flow rate (t/h)	Predicted Critical Power (MW)	Experimental Critical Power (MW)	% Relative Error
30	6.046	7.200	16.0
40	7.230	8.000	9.6
50	8.207	8.700	5.7
60	8.967	9.300	3.6

Because of its more accurate and yet conservative results the EPRI-Columbia correlation combined with the subchannel analysis was selected to evaluate the thermalhydraulic performance of the large fuel assembly concept explored in this project. Note that NUPEC analysis also concluded that the EPRI-Columbia correlation yielded the most accurate prediction of the experimental data [29].

APPENDIX-B: The Evaluation and Modifications to the Stability Code

B.1. Modifications to the Stability Code

The original stability code [6] is modified to account for non-uniform power profiles and pressure loss coefficients within the core region. A comparison with a separately developed modified BWR stability work was made [30]

B.1.1. Non-Uniform Power Profile Capability

First, the algorithm to calculate steady state parameters such as axial coolant, clad, gap and fuel temperature, coolant flow quality, coolant velocity and density distributions are modified such that the axially average heat flux is weighted with the given normalized power profile.

In addition to steady state calculations, transfer functions and input perturbations are also modified. The characteristic equation for the core region can be written as follows:

$$\delta\Delta p_{core} = \Gamma_{core}\delta w_{in} + \pi_{core}\delta q_o''' + H_{core}\delta h_{in}$$

Where;

$\delta\Delta p_{core}$: Total core pressure drop perturbation

δw_{in} : Inlet flow perturbation

$\delta q_o'''$: Heat generation perturbation

δh_{in} : Inlet enthalpy perturbation

$$\Gamma_{core} = \frac{\delta\Delta p_{core}}{\delta w_{in}}$$

$$\pi_{core} = \frac{\delta\Delta p_{core}}{\delta q_o'''}$$

$$H_{core} = \frac{\delta\Delta p_{core}}{\delta h_{in}}$$

The average heat flux terms within the transfer functions ($\Gamma_{core}, \pi_{core}, H_{core}$) are weighted with the given normalized power profile. Furthermore, heat generation perturbation ($\delta q_o'''$), which is originally a unit step function, is also weighted with the normalized power profile.

Finally, the neutronic feedback algorithm for in-phase stability is modified for the coolant void and fuel temperature coefficients. Neutronic feedback is modeled via the point kinetics model. Given the perturbation, each axial node causes a certain magnitude of oscillation contributing to the overall reactivity with the following weighting factor:

$$W_n = \frac{P_n^2}{\sum_{n=1}^{N} P_n^2} \qquad \text{where;} \qquad P_n \text{ is the power produced at node "n".}$$

To account for the non-uniformities, average power is weighted with the normalized power profile for each node. As a result, weighting factor becomes:

$$W_n = \frac{P_{ave}^2 \times ppf^2(n)}{\sum_{n=1}^{N} P_{ave}^2 \times ppf^2(n)}$$

where;

P_{ave} : Average Power

$ppf(n)$: Axial power peaking factor of the node "n".

Total reactivity resulting from the given oscillation is the sum of contributions of the each node oscillations.

$$\rho_{void} = C_{void} \sum_{n=1}^{N} W_n \delta\rho_{void}^n$$

$$\rho_f = C_f \sum_{n=1}^{N} W_n \delta\rho_f^n$$

ρ_{void}: Total reactivity due to coolant void oscillation

C_{void}: Coolant void reactivity coefficient (reactivity/(void fraction oscillation))

W_n: Weighting factor of node "n"

$\delta\rho_{void}^n$: Void oscillation of node "n"

ρ_f : Total reactivity due to fuel temperature oscillation

C_f : Fuel temperature coefficient (reactivity/(Fuel Temperature oscillation))

$\delta\rho_f^n$: Fuel temperature oscillation of node "n"

B.1.2. Spacer and Tie Plate Pressure Loss Modeling

Pressure drop resulting from a pressure loss coefficient is modeled as:

$\Delta P_{form} = K\frac{\rho_l V_l^2}{2}$ for the single phase region

$\Delta P_{form} = \phi_{lo}^2 K\frac{G^2}{2\rho_l}$ for the two phase region

$\phi_{lo}^2 = 2\frac{\rho_l}{\rho_m}$ [6]

G: Coolant axial mass flux

ρ_m : Coolant mixture density

ρ_l : Liquid density

K : Pressure loss coefficient

V_m : Coolant axial mixture velocity

V_l : Single phase region coolant velocity

Perturbation of the pressure drop equation yields the following:

$\delta\Delta P_{form} = K\rho_l V_l \delta V_l$ (For the single phase region)

$\delta\Delta P_{form} = 2K\rho_m V_m \delta V_m + K V_m^2 \delta\rho_m$ (For the two phase region)

Resulting pressure drop perturbations are included for the corresponding axial locations.

B.2. The Evaluation of the Stability Code

To gain confidence in the performance of the single channel and in-phase stability codes, a simple parametric study has been conducted and the results are compared with the expected trends. The reference core is adopted for in-phase stability; whereas reference hot channel is used for single channel stability to analyze the effect of the power profile, inlet orificing coefficient, inlet enthalpy. Furthermore, the effect of neutronic feedback coefficients is examined for in-phase stability analysis. Finally, note that number of nodes in single phase region is 200 and in two phase region is 500 for all calculations. Increasing the node number further is found to have a negligible effect [6].

B.2.1. The Effect of the Power Profile on the Decay Ratio

Various power profiles have been modeled varying the parameter n in the following equation:

$P=P_0\sin(\pi(z/L)^{1/n})$

P_0 = Normalization constant

L= Heated Length

P= Axial Power profile

The higher n, the more bottom peaked the power profile is. As can be seen in Table-B.1 and Table-B.2, the decay ratio increases as the length of the single phase region decreases. The uniform power profile appears to have the lowest stability margin because it has the shortest single-phase length. Moreover, single channel decay ratio is more susceptible to the power profile.

Table-B.1: The Effect of Power Profile on Single Channel Decay Ratio

Power Profile	Decay Ratio	Hot Channel Single phase length (m)
N=1	0.07	0.82
N=2	0.19	0.43
N=3	0.28	0.29

Table-B.2: The Effect of Power Profile on In-phase Decay Ratio

Power Profile	Decay Ratio	Hot Channel Single phase length (m)	Average Channel Single Phase Length (m)	Low Channel Single Phase Length (m)
N=1	0.28	0.88	1.04	0.97
N=2	0.34	0.47	0.60	0.55
N=3	0.35	0.33	0.43	0.39

B.2.2. The Effect of Inlet Orificing Coefficient on the Decay Ratio

Table-B.3 shows the effect of inlet orificing coefficient on the single channel decay ratio. Single channel decay ratio rapidly decreases with increasing inlet orificing coefficient.

Table-B.3 The Effect of Inlet Orificing Coefficient on Single Channel Decay Ratio (Uniform Power Profile)

Hot channel Orificing Coefficient	Decay Ratio
20	0.15
30	0.11
40	0.08

To analyze the effect of inlet orificing coefficient on the in-phase stability margin, the orificing coefficients of the hot, average power and low power channels are increased simultaneously such that all channels maintain the same pressure drop. Because the hot and average power channels are modeled as having the same orificing coefficients, a difference in pressure drop of the channels up to 2 % is allowed. The reference power profile is adopted in this calculation. As can be seen in Table-B.4, increasing the orificing coefficient is not a very effective approach to reduce the in-phase decay ratio.

Table-B.4: The Effect of Inlet Orificing Coefficient on In-phase Decay Ratio (Uniform Power Profile)

Hot channel Orificing Coefficient	Average Channel Orificing Coefficient	Low Channel Orificing Coefficient	Pressure Drop (kPa)	Decay Ratio
20	20	170	153	0.33
30	30	205	174	0.30
40	40	236	193	0.28

B.2.3. The Effect of Inlet Enthalpy Variation on the Decay Ratio

The effect of the inlet subcooling was also evaluated. It was found that at high subcooling a decrease of subcooling destabilizes the system, while at low subcooling the trend reverses (Table-B.5 and Table-B.6). This trend is explained in Tong and Tang [31] as follows: "An increase in inlet subcooling decreases the void fraction and increases the non-boiling length and its transit time. Thus an increase of inlet subcooling stabilizes two-phase boiling flow at medium or high subcoolings. At small subcoolings, an incremental change in transit time is significant in the response delay of void generation from the inlet flow and an increase in inlet subcooling destabilizes the flow."

Table-B.5: The Effect of Inlet Enthalpy Variation on Single Channel Decay Ratio (Uniform Power Profile)

Core inlet Temperature (°C)	Decay Ratio
266	0.11
270	0.14
274	0.14
278.3	0.14
282	0.13
286	0.10

Table-B.6: The Effect of Inlet Enthalpy Variation on In-phase Decay Ratio (Uniform Power Profile)

Core inlet Temperature (°C)	Decay Ratio
270	0.34
274	0.40
278.3	0.33
282	0.24

B.2.4. The effect of Void Coefficient On In-phase Decay Ratio:

As can be seen in Table-B.7, a more negative void coefficient destabilizes the system.

Table-B.7: The Effect of Void Coefficient on In-phase Decay Ratio (Uniform Power Profile)

Void Coefficient (reactivity/void fraction)	Decay Ratio
-0.12	0.27
-0.14	0.32
-0.16	0.37
-0.18	0.42
-0.20	0.48

B.2.5. The Effect of Fuel Temperature Coefficient on the Decay Ratio:

A more negative fuel temperature coefficient stabilizes the system (Table B.8) but the effect is small with respect to the void coefficient.

Table-B.8 The Effect of Fuel Temperature Coefficient on In-phase Decay Ratio (Uniform Power Profile)

Fuel Temperature Coefficient (reactivity/fuel temperature)	Decay Ratio
-1E-05	0.330
-2E-05	0.328
-3E-05	0.326
-4E-05	0.323

This simple parametric study has established that our stability code captures the essential phenomena, generates reasonable results and thus can be used with a certain degree of confidence to evaluate the dynamic stability of the new fuel assembly designs.

APPENDIX-C: Modifying Large Assembly Power Peaking Factors to Account for the Presence of the Part Length Rods

The power peaking factors calculated with 2D neutronics have to be modified to accommodate for part length rods. The following steps are adopted:

1- By using the reference axial power profile, the fraction of rod power generated in the upper part is calculated as:

$$g=\frac{\int_{L_{part}}^{L_{full}} P(z)dz}{\int_{0}^{L_{full}} P(z)dz}$$

2- Rejecting this fraction of power from each part length rod gives the power peaking factor of each part length rod. $PPF2(i)=PPF1(i)\times(1-g) \qquad i=1,N_{part}$

3- Total power rejected is calculated.

$$f=\sum_{i=0}^{N_{part}} PPF1(i)\times g$$

4- This power is shared by the full length rods according to their contribution to power generation.

$$P2(i)=P1(i)+\frac{P1(i)}{\sum_{j=0}^{N_{full}} P1(j)}\times f \qquad i=1,N_{full}$$

P(z) : Reference axial power profile

g : Fraction of rod power generated in upper section upper part of part length rods.

f : Fraction of the total power generated in upper part of part length rods

PPF1(i) : Part-length rod power peaking factor calculated with 2D neutronics

PPF2(i) : Modified part-length rod power peaking factor

P1(i): Full-length rod power peaking factor calculated with 2D neutronics

P2(i): Modified full-length rod power peaking factor

N_{part} : Number of part length rods

N_{full} : Number of full length rods

L_{full} : Heated length of the full rods

L_{part} : Heated length of the part length rods.

APPENDIX-D: Vibration Ratio Correlation

Modified Païdoussis correlation [14]:

$$\frac{y_{\max}}{d} = 15 \times \Gamma^{-4} (5 \times 10^{-4} K) \left[\frac{u^{1.6} \varepsilon^{1.8} \mathrm{Re}^{0.25}}{1+u^2} \right] \left(\frac{D_h}{d} \right)^{0.4} \left(\frac{\beta^{2/3}}{1+4\beta} \right)$$

The parameters that appear in this empirical correlation are defined as follows:

y_{max} : max peak vibration amplitude (m). The peak value is about two to three times the root mean square amplitude y_{rms}. Since our approach aims to develop a conservative analysis, this peak value is calculated.

d: rod outer diameter (m)

Γ: 4.73 for rods clamped at both ends

K: 5 for turbulent flow

$u = VL\sqrt{\frac{\rho A}{EI}}$ dimensionless velocity, where:

V is the coolant velocity (m/s), directly computed by VIPRE

L is the distance between two grid spacers. L=0.5085 m for the reference as well as the large assembly designs

ρ is the coolant density (kg/m^3), directly computed by VIPRE

$A = \pi \cdot \frac{d^2}{4}$ is the rod cross sectional area (m^2)

E is the Zircaloy Young's modulus. E=8.05E+10 Pa

I is the inertia momentum of the clad: $I = \frac{\pi}{2} \cdot \left[\left(\frac{d}{2} \right)^4 - \left(\frac{D_{in}}{2} \right)^4 \right]$ with D_{in} as the inner clad diameter (m)

$\varepsilon = \mathrm{L} / d$

$\mathrm{Re} = \frac{\rho V D_h}{\mu}$ Reynolds number, where:

D_h is the eq. diameter of the channel in which the assembly subchannels have been lumped (m)

μ is the coolant mixture viscosity: $\mu = \mu_g \cdot \alpha + \mu_l \cdot (1-\alpha)$ where α is the void fraction directly computed by VIPRE

$\beta = \dfrac{\rho A}{\rho A + m_l}$ where m_l is the mass per unit length of clad (kg).

Appendix E: Screening of Various Geometries for Fuel Assemblies with Cylindrical Rods

E.1. Objective

The objective of this task is to explore various fuel assembly geometries, to maximize the power density while maintaining the use of UO_2-fuelled, Zr-clad solid cylindrical rods.

E.2. Screening of Alternative Fuel Assembly Geometries

The Hench-Gillis dryout correlation was used here, because this screening study was performed before the EPRI-Columbia correlation was proven to be superior in reproducing the NUPEC data (see Appendix A). The Hench-Gillis correlation indicates that, for given operating pressure, the critical quality depends mostly on two parameters, i.e., the heat transfer area and the mass flux. Specifically, the critical quality increases as the heat transfer area increases and the mass flux decreases. Therefore, to "create" margin and enable higher power densities, it is necessary to increase the heat transfer area and decrease the mass flux. The first requirement drives the design towards smaller fuel pins, while the second drives it towards higher pitch-to-diameter ratios.

Constraints and Assumptions

The reference core parameters given in Tables 3.1 and 3.2 have been maintained for all explored fuel assembly configurations with cylindrical pins. In addition, note that:

- The J1 factor characterizing the local power profile within an assembly in the Hench-Gillis correlation is held constant at 1.126.

Hence, the reference core power-to-flow ratio, the radial and axial power profiles, the total moderating power (H/HM ratio) and the minimum critical power ratio are preserved during the optimization study. The thermal-hydraulic parameters are calculated with a simple energy balance compiled in FORTRAN, while the neutronic parameters are calculated with CASMO-4.

The range of parameters varied during the optimization study is given below in Table E.1.

Table E.1. The Range of Parameters of Optimization

Parameters	**Minimum**	**Maximum**
Pitch to Diameter ratio	1.1	1.6
Pin Diameter	9.0 mm	13 mm
Linear Heat rate	9 kW/m	19 kW/m

In this analysis, each interval is divided into 300 nodes and thus 300^3=27,000,000 cases are examined for each geometry. The results are described below.

E.3. Results

E.3.1. Square Lattice Results

The analyses for the square lattice focused on two approaches. In the first approach the reference 9x9 configuration with cross-shaped control rods in the fuel assembly gap is explored. However, with this approach, as the fuel pin diameter and/or pitch-to-diameter ratio are varied, the fuel assembly pitch also varies, and so does the number and location of the control rod drive mechanisms in the core. Such change of the control rod drive mechanisms number and location could not be implemented in existing plants, as the number and location of the penetrations in the RPV lower head is fixed. Therefore, we explored a second configuration in which four 9x9 assemblies and gap regions are replaced by a large square assembly (Figure E.1), while the core cell lattice pitch is preserved. The large assembly has a variable number of fuel pins and many water rods for moderation, which also serve as guide tubes for finger-type control rods. In this case, the number and location of the control rod drive mechanisms remains unchanged. Furthermore, since the cross-shaped control rods are eliminated, the inter-assembly gap can be drastically reduced, which has two benefits; first, it reduces the local peaking considerably (though this was not taken credit for in the analysis); second, it makes more room available for the fuel rods, thus affording an additional incremental power density increase. The results for both square approaches are reported in Tables E.2 and E.3.

It can be seen that the square lattices with smaller fuel pins and larger pitch-to-diameter ratios than the reference core can achieve power densities of the order of 65 kW/L, or some 30% higher than the reference core. This result holds for both square assembly designs, i.e., the 9x9 and the large design. However, the large square fuel assembly approach is preferred because of its expected lower local power peaking, its slightly higher power density, and, importantly, its control rod drive mechanism number and location, which is identical to the reference core, and thus would not require modifications of the penetrations through the RPV lower head.

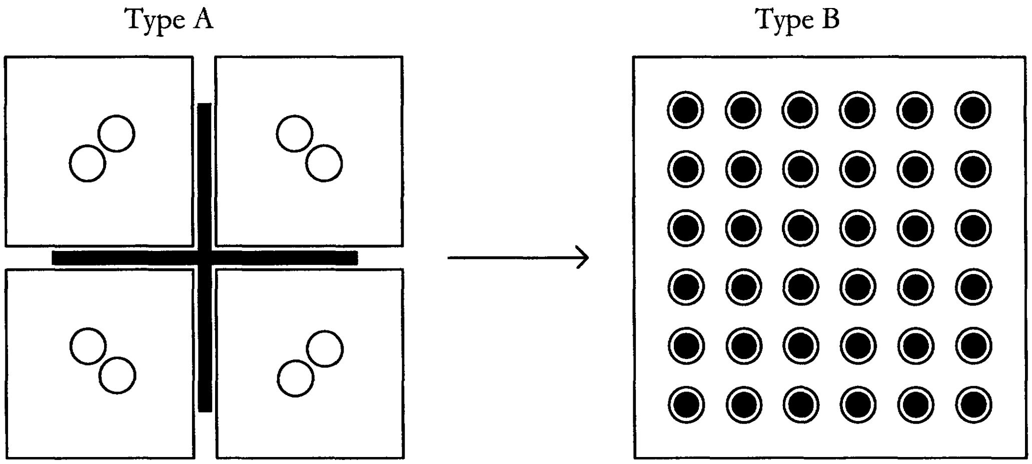

Figure E.1: Transformation to the Large Assembly

Table E.2. Results for the 9×9 assembly with two water rods (Type A)*

Pin diameter (mm)	Pellet diameter (mm)	P/D	Power density (kW/l)	Water Rod Outer diameter (mm)	k-inf CR-OUT	Void Coeff. ×(E+4)	Doppler Coeff. ×(E+4)
9.68	8.516	1.463	64.16	17.91	1.44726	-6.69	-0.151
10.28	8.78	1.433	62.18	22.8	1.44476	-6.46	-0.149
11.04	9.43	1.438	60.39	27.2	1.44730	-6.30	-0.146

* These fuel assemblies do not preserve the outer dimension of the reference 9x9 fuel assembly

The gap thickness between assemblies is held at 7 mm, and assembly duct thickness is equal to 1 mm. The H/HM ratio is maintained by adjusting the diameter of the water rods.

Table E.3. Results for the Large Square Assembly (Type B)**

Fuel Rod Array	Pin Diameter (mm)	Pellet Diameter (mm)	Power Density (kW/l)	Linear Heat Rate (kW/m)	P/D	# and outer diameter of water rods (mm)
20×20	9.68	8.516	66.5	17.22	1.53042	41-13.81
21×21	9.68	8.516	63.39	16.18	1.4585	77-13.12
22×22	9.68	8.516	60.45	15.22	1.39303	115-12.48
19×19	10.28	8.78	64.48	18.72	1.5167	41-14.59
20×20	10.28	8.78	61.29	17.52	1.44191	75-13.82
21×21	10.28	8.78	58.29	16.46	1.37414	112-13.13

** These fuel assemblies preserve the control rod drive mechanism number and location

The gap thickness between assemblies is held at 2 mm, and the assembly duct thickness is equal to 2.5 mm. The H/HM ratio is maintained by adjusting the number and diameter of the water rods.

E.3.2. Hexagonal Lattice Results

We considered small hexagonal fuel assemblies (19 fuel pins) with no water rods, and larger hexagonal fuel assemblies with a three-branched water gap in the middle, thus effectively realizing three rhombic subassemblies with 25 fuel pins each (Figure E.2). Because of obvious geometric reasons, it is not possible to maintain the number and location of the control rod drive mechanisms when a hexagonal lattice is used, so this approach can be considered only for new reactors. The results of the optimization study are reported in Tables E.4 and E.5.

Table E.4: Results for the Small Hexagonal Assembly

Pin diameter (mm)	Pellet diameter (mm)	P/D	Power density (kW/l)	Linear heat rate (kW/m)	k-inf CR-OUT	Void Coefficient ×(E+04)	Doppler Coefficient ×(E+4)
9.76	8.59	1.50	58.19	14.7	1.44409	-4.86	-0.149
10.48	8.96	1.485	57.70	16.2	1.44439	-5.01	-0.146
11.26	9.62	1.50	57.18	18.6	1.44791	-5.19	-0.144

The gap thickness between assemblies is held at 7 mm, and the assembly duct thickness is equal to 1 mm.

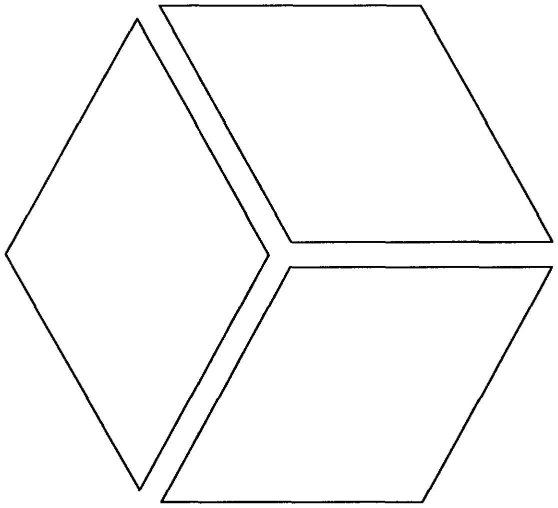

Figure E.2: Large Hexagonal Assembly

Table E.5 Results for the Large Hexagonal Assembly

Pin diameter (mm)	Pellet diameter(mm)	P/D	Power density (kW/l)	Gap thickness between rhomboids (mm)	Linear heat rate (kW/m)
9.70	8.53	1.60	61.86	5.53	15.8
10.48	8.96	1.58	61.0	5.44	17.5
11.02	9.42	1.58	60.0	6.09	19.0

The gap thickness between assemblies is held at 7 mm, and the assembly duct thickness is equal to 1 mm.

Switching to a hexagonal lattice does not seem to provide any significant benefit in terms of power density, and also warrants major modifications of the control rod drive mechanisms system. Thus, hexagonal lattices will not be further pursued.

Interestingly, the maintenance of the hydrogen-to-heavy-metal ratio in all these configurations (both square and hexagonal) does seem to preserve the reactivity quite well, as suggested by the nearly constant value of the multiplication factor, regardless of lattice geometry, pitch-to-diameter ratio and pin diameter.

E.4. Conclusions

A large number of square and hexagonal fuel assembly lattices with fuel and water rods of various diameters and pitch-to-diameter ratios have been explored in the pursuit of higher power density. The results show that large square fuel assemblies can achieve over 30% higher power density, while maintaining dryout margin, neutronic behavior and, importantly, number and location of the control rod drive mechanisms, which should facilitate retrofitting in existing plants. This geometry was deemed promising and extensively analyzed in this thesis work.

APPENDIX-F: Sensitivity Study of the Subchannel Analysis

F.1. The Effect of Turbulent Mixing on Minimum Critical Heat Flux Ratio

The Sensitivity of the turbulence mixing on MCHFR is examined by a parametric study. Mixing Flow Correlation has the following form: $W'_{ij} = \beta \times s_{ij} \times G$.

Coefficient β is given with the following correlation for each subchannel gap:

$$W'_{ij}/\mu = \frac{0.005}{2}\left[1+\left(\frac{D_{ej}}{D_{ei}}\right)^{1.5}\right]\mathrm{Re}^{0.9}\left(\frac{s_{ij}}{D}\right)^{0.106} \quad [32]$$

$$\beta = \frac{W'_{ij}}{(s_{ij} \times G)} \qquad \beta \cong 0.005 \text{ (For the Central Subchannels)}$$

W'_{ij} : Flow per unit length between subchannel i & j.

G : Axial Mass flux

s_{ij} : Gap between fuel rods

D_{ei} : Equivalent diameter of subchannel i

D_{ej} : Equivalent diameter of subchannel j

D : Fuel Rod diameter

μ : Dynamic Viscosity

Re : Reynolds Number

Variation of MCHFR as a function of β for the most promising large assembly is given in Table-F.1. The sensitivity of the MCHFR to β is modest.

F.1 The effect of Turbulent Mixing Flow Coefficient on MCHFR

β	MCHFR
0.002	1.201
0.005	1.228
0.010	1.247

F.2. The Effect of Part Length Rods on Minimum Critical Heat Flux Ratio

The effect of partial length rods on MCHFR is examined for the most promising large assembly. In the analysis without partial length rods, the fresh assembly power peaking factors given in Table-8.7 are used. Moreover, the reference axial power profile is preserved for all fuel rods. As can be seen in Table-F.2, the partial length rods improve the MCHFR by 2.4%.

Table-F.2 The Effect of Part Length Rods on MCHFR (Fresh Large Assembly)

	MCHFR
Large Assembly With Partial Length Rods	1.23
Large Assembly Without Part Length Rods	1.20

APPENDIX-G: Input Files

G-1 VIPRE-01 Input for the Subchannel Analysis of the Large Assembly

```
**********************************************************************
* MIT Large Assembly BWR with epri-1
1,0,0,                              *vipre.1
Bwr solid fuel                          *vipre.2
*
geom,72,72,90,0,0,0,    *normal geometry input  , check last 0---- BWR normal geom input
Oo  *geom.1
*
164.516,0.0,0.5,     *geom.2
*
*
1,0.05086,0.55380,0.29684,2,2,0.068,0.45,10,0.118,0.4,
2,0.07596,0.59369,0.59369,2,3,0.068,0.39,11,0.136,0.4,
3,0.03075,0.408062,0.23604,1,12,0.089,0.39,
4,0.03075,0.408062,0.23604,2,5,0.068,0.39,14,0.089,0.39,
5,0.07596,0.59369,0.59369,2,6,0.068,0.39,15,0.136,0.4,
6,0.03075,0.408062,0.23604,1,16,0.088,0.39,
7,0.03075,0.408062,0.23604,2,8,0.068,0.39,18,0.089,0.39,
8,0.07596,0.59369,0.59369,2,9,0.068,0.39,19,0.136,0.39,
9,0.03075,0.408062,0.23604,1,20,0.089,0.25,
*
10,0.10172,1.10760,0.59369,2,11,0.136,0.45,21,0.118,0.51,
11,0.15191,1.18737,1.18737,2,12,0.136,0.51,22,0.136,0.51,
12,0.16799,1.50791,1.01214,2,13,0.089,0.51,23,0.136,0.51,
13,0.06150,0.81613,0.47208,2,14,0.089,0.51,24,0.136,0.39,
14,0.16799,1.50791,1.01214,2,15,0.136,0.51,25,0.136,0.51,
15,0.15191,1.18737,1.18737,2,16,0.136,0.51,26,0.136,0.51,
16,0.16799,1.50791,1.01214,2,17,0.089,0.51,27,0.136,0.51,
17,0.06150,0.81613,0.47208,2,18,0.089,0.51,28,0.136,0.39,
18,0.16799,1.50791,1.01214,2,19,0.136,0.51,29,0.136,0.51,
19,0.15191,1.18737,1.18737,2,20,0.136,0.39,30,0.136,0.39,
20,0.08399,0.7540,0.50607,
*
21,0.10172,1.10760,0.59369,2,22,0.136,0.45,31,0.118,0.51,
22,0.15191,1.18737,1.18737,2,23,0.136,0.51,32,0.136,0.51,
23,0.15191,1.18737,1.18737,2,24,0.136,0.51,33,0.136,0.51,
24,0.15191,1.18737,1.18737,2,25,0.136,0.51,34,0.136,0.39,
25,0.15191,1.18737,1.18737,2,26,0.136,0.51,35,0.136,0.51,
26,0.15191,1.18737,1.18737,2,27,0.136,0.51,36,0.136,0.51,
27,0.15191,1.18737,1.18737,2,28,0.136,0.51,37,0.136,0.51,
28,0.15191,1.18737,1.18737,2,29,0.136,0.51,38,0.136,0.39,
```

```
29,0.15191,1.18737,1.18737,2,30,0.136,0.39,39,0.136,0.4,
30,0.07596,0.59369,0.59369,
*
31,0.10172,1.10760,0.59369,2,32,0.136,0.45,40,0.118,0.51,
32,0.15191,1.18737,1.18737,2,33,0.136,0.51,41,0.136,0.51,
33,0.16799,1.50791,1.01214,2,34,0.089,0.51,42,0.089,0.51,
34,0.06150,0.81613,0.47208,1,35,0.089,0.51,
35,0.16799,1.50791,1.01214,2,36,0.136,0.51,43,0.089,0.51,
36,0.15191,1.18737,1.18737,2,37,0.136,0.51,44,0.136,0.51,
37,0.16799,1.50791,1.01214,2,38,0.089,0.51,45,0.089,0.51,
38,0.06150,0.81613,0.47208,1,39,0.089,0.4,
39,0.08399,0.7540,0.50607,
*
40,0.10172,1.10760,0.59369,2,41,0.136,0.45,46,0.118,0.51,
41,0.15191,1.18737,1.18737,2,42,0.136,0.39,47,0.136,0.51,
42,0.06150,0.81613,0.47208,1,48,0.089,0.51,
43,0.06150,0.81613,0.47208,2,44,0.136,0.39,50,0.089,0.51,
44,0.15191,1.18737,1.18737,2,45,0.136,0.39,51,0.136,0.51,
45,0.06150,0.81613,0.47208,1,52,0.089,0.4,
*
46,0.10172,1.10760,0.59369,2,47,0.136,0.45,53,0.118,0.51,
47,0.15191,1.18737,1.18737,2,48,0.136,0.51,54,0.136,0.51,
48,0.16799,1.50791,1.01214,2,49,0.089,0.51,55,0.136,0.51,
49,0.06150,0.81613,0.47208,2,50,0.089,0.51,56,0.136,0.39,
50,0.16799,1.50791,1.01214,2,51,0.136,0.51,57,0.136,0.39,
51,0.15191,1.18737,1.18737,2,52,0.136,0.39,58,0.136,0.4,
52,0.08399,0.7540,0.50607,
*
53,0.10172,1.10760,0.59369,2,54,0.136,0.45,59,0.118,0.51,
54,0.15191,1.18737,1.18737,2,55,0.136,0.51,60,0.136,0.51,
55,0.15191,1.18737,1.18737,2,56,0.136,0.51,61,0.136,0.51,
56,0.16799,1.50791,1.01214,2,57,0.089,0.51,62,0.089,0.51,
57,0.06150,0.81613,0.47208,1,58,0.089,0.40,
58,0.08399,0.7540,0.50607,
*
59,0.10172,1.10760,0.59369,2,60,0.136,0.45,63,0.118,0.51,
60,0.15191,1.18737,1.18737,2,61,0.136,0.51,64,0.136,0.51,
61,0.15191,1.18737,1.18737,2,62,0.136,0.39,65,0.136,0.51,
62,0.06150,0.81613,0.47208,1,66,0.083,0.4,
*
63,0.10172,1.10760,0.59369,2,64,0.136,0.45,67,0.118,0.51,
64,0.15191,1.18737,1.18737,2,65,0.136,0.51,68,0.136,0.51,
65,0.15191,1.18737,1.18737,2,66,0.136,0.4,69,0.136,0.39,
66,0.08399,0.7540,0.50607,
*
67,0.10172,1.10760,0.59369,2,68,0.136,0.45,70,0.118,0.51,
68,0.15191,1.18737,1.18737,2,69,0.136,0.4,71,0.136,0.39,
69,0.07596,0.59369,0.59369,
```

```
*
70,0.10172,1.10760,0.59369,2,71,0.136,0.3,72,0.118,0.3,
71,0.07596,0.59369,0.59369,
*
72,0.03313,0.45551,0.14842,
*
*geom.4
prop,0,1,2,1  *internal EPRI functions *prop.1
*
*
rods,2,51,1,1,1,0,0,0,0,0,0 *three material types,one type of geo. *rods.1
145.98,9.268,0,0                                       *rods.2
*
26                    * rods.3
*      *rods4    first axial profile (for FLFRs)
0.0,0.0,    3.04,0.382,   9.12,0.694,   15.21,0.935,
21.29,1.106,  27.37,1.216,  33.45,1.307,   39.54,1.478,
45.62,1.518,  51.70,1.498,  57.78,1.448,  63.87,1.367,
69.95,1.287,  76.03,1.166,  82.11,1.066,  88.20,1.015,
94.28,0.975,  100.36,0.945,  106.44,0.975,  112.53,0.965,
118.61,0.915, 124.69,0.774,  130.77,0.593,  136.86,0.382,
142.94,0.121, 145.98,0.00
*
26                    * rods.3
*      *rods4    second axial profile (for PLFRs)
0.0,0.0,    3.04,0.50,   9.12,0.91,    15.21,1.221,
21.29,1.44,   27.37,1.59,   33.45,1.71,    39.54,1.93,
45.62,1.98,   51.70,1.96,   57.78,1.89,   63.87,1.79,
69.95,1.68,   76.03,1.52,   82.11,1.39,   88.20,1.33,
94.28,1.27,   95.9,1.23, 99.0,0., 106.44,0.,  112.53,0.,
118.61,0., 124.69,0.,  130.77,0.,  136.86,0.,
142.94,0., 145.98,0.00
*
******rods geometry input                        *rods.9
1,1,1.156,1,1,0.25,2,0.25,10,0.25,11,0.25,
2,1,1.056,1,2,0.25,3,0.1988,11,0.25,12,0.3012,
3,1,1.090,1,4,0.1988,5,0.25,14,0.3012,15,0.25,
4,1,0.953,1,5,0.25,6,0.1988,15,0.25,16,0.3012,
5,1,1.092,1,7,0.1988,8,0.25,18,0.3012,19,0.25,
6,1,1.121,1,8,0.25,9,0.1988,19,0.25,20,0.3012,
*
7,1,1.126,1,10,0.25,11,0.25,21,0.25,22,0.25,
8,1,0.930,1,11,0.25,12,0.25,22,0.25,23,0.25,
9,1,0.388,1,12,0.3012,13,0.1988,23,0.25,24,0.25,
10,1,0.943,1,13,0.1988,14,0.3012,24,0.25,25,0.25,
11,1,0.973,1,14,0.25,15,0.25,25,0.25,26,0.25,
12,1,0.946,1,15,0.25,16,0.25,26,0.25,27,0.25,
13,1,0.385,1,16,0.3012,17,0.1988,27,0.25,28,0.25,
```

```
14,1,1.017,1,17,0.1988,18,0.3012,28,0.25,29,0.25,
15,1,0.966,1,18,0.25,19,0.25,29,0.25,30,0.25,
16,1,1.010,1,19,0.25,20,0.125,30,0.125
*
17,1,1.120,1,21,0.25,22,0.25,31,0.25,32,0.25,
18,1,0.392,1,22,0.25,23,0.25,32,0.25,33,0.25,
19,1,0.952,1,23,0.25,24,0.25,33,0.3012,34,0.1988,
20,1,0.977,1,24,0.25,25,0.25,34,0.1988,35,0.3012,
21,1,0.383,1,25,0.25,26,0.25,35,0.25,36,0.25,
22,1,0.981,1,26,0.25,27,0.25,36,0.25,37,0.25,
23,1,0.944,1,27,0.25,28,0.25,37,0.3012,38,0.1988,
24,1,1.029,1,28,0.25,29,0.25,38,0.1988,39,0.3012,
25,1,0.378,1,29,0.25,30,0.125,39,0.125,
*
26,1,1.144,1,31,0.25,32,0.25,40,0.25,41,0.25,
27,1,1.060,1,32,0.25,33,0.3012,41,0.25,42,0.1988,
28,1,1.062,1,35,0.3012,36,0.25,43,0.1988,44,0.25,
29,1,1.063,1,36,0.25,37,0.3012,44,0.25,45,0.1988,
*
30,1,1.193,1,40,0.25,41,0.25,46,0.25,47,0.25,
31,1,1.150,1,41,0.25,42,0.1988,47,0.25,48,0.3012,
32,1,1.139,1,43,0.1988,44,0.25,50,0.3012,51,0.25,
33,1,1.160,1,44,0.25,45,0.1988,51,0.25,52,0.3012,
*
34,1,1.203,1,46,0.25,47,0.25,53,0.25,54,0.25,
35,1,0.826,2,47,0.25,48,0.25,54,0.25,55,0.25,
36,1,1.248,1,48,0.3012,49,0.1988,55,0.25,56,0.25,
37,1,1.112,1,49,0.1988,50,0.3012,56,0.3012,57,0.1988,
38,1,1.212,1,50,0.25,51,0.25,57,0.1988,58,0.3012,
39,1,1.123,1,51,0.25,52,0.125,58,0.125,
*
40,1,1.220,1,53,0.25,54,0.25,59,0.25,60,0.25,
41,1,1.070,1,54,0.25,55,0.25,60,0.25,61,0.25,
42,1,1.180,1,55,0.25,56,0.3012,61,0.25,62,0.1988,
*
43,1,1.201,1,59,0.25,60,0.25,63,0.25,64,0.25,
44,1,0.406,1,60,0.25,61,0.25,64,0.25,65,0.25
45,1,1.092,1,61,0.25,62,0.1988,65,0.25,66,0.3012,
*
46,1,1.234,1,63,0.25,64,0.25,67,0.25,68,0.25,
47,1,1.074,1,64,0.25,65,0.25,68,0.25,69,0.25,
48,1,1.160,1,65,0.25,66,0.125,69,0.125,
*
49,1,1.208,1,67,0.25,68,0.25,70,0.25,71,0.25,
50,1,0.768,2,68,0.25,69,0.125,71,0.125,
*
51,1,1.217,1,70,0.25,71,0.125,72,0.125,
*
```

```
0                                   *rods.9
*
*fuel
1,nucl,0.378,0.328,12,0.0,0.028               *rods.62
0,0,0,0,0,1056.66,0.955,0,                 *rods 63
*constant radial power in the pellet, no power in the clad
*
*water tube
*2,tube,1.038,0.978,1                             *rods.68
*3,1,0.03,1.0,                                *rods.69
*wall
*3,wall,5.415,0.0,1
*3,1,0.1,1.0,
*
1,1,409.7,clad,
662,0.076,10.05,
*********************************
*P,T
oper,1,1,0,1,2,1,0,0,0,                       *oper.1
-1.0,2.0,2.0,005,                          *oper.2
0                                       *oper.3
1035.0,533.0,20.22,78.8254,0.0
*
*Rod power got from total power divided total number of rods
0,           *no forcing functions                 *oper.12
*********************************
*correlations
corr,1,2,0,                                   *corr.1
epri,epri,epri,none,                            *corr.2
0.2,                                      *corr.3
ditb,chen,chen,epri,cond,g5.7,    *correlation for boiling curve   *corr.6
epri
1,0,1.2
*********************
mixx,0,0,1,
0.8,0.0048,0.0,
0.0089,0.0,0.0041,0.0,0.0091,0.0,0.0049,0.0,
0.0062,0.0,0.0091,0.0,0.0062,0.0,0.0091,0.0,
0.0049,0.0,0.0062,0.0,0.0091,0.0,0.0062,0.0,
0.0091,0.0,0.0049,0.0,0.0062,0.0,0.0048,0.0,
0.0041,0.0,0.0048,0.0,0.0049,0.0,0.0062,0.0,
0.0048,0.0,0.0062,0.0,0.0049,0.0,0.0048,0.0,
0.0048,0.0,0.0048,0.0,0.0049,0.0,0.0062,0.0,
0.0049,0.0,0.0062,0.0,0.0049,0.0,0.0049,0.0,
0.0049,0.0,0.0049,0.0,0.0049,0.0,0.0048,0.0,
0.0041,0.0,0.0049,0.0,0.0049,0.0,0.0049,0.0,
0.0049,0.0,0.0049,0.0,0.0049,0.0,0.0049,0.0,
0.0049,0.0,0.0049,0.0,0.0049,0.0,0.0049,0.0,
```

```
0.0049,0.0,0.0048,0.0,0.0049,0.0,0.0049,0.0,
0.0049,0.0,0.0049,0.0,0.0041,0.0,0.0049,0.0,
0.0049,0.0,0.0062,0.0,0.0062,0.0,0.0062,0.0,
0.0049,0.0,0.0062,0.0,0.0049,0.0,0.0049,0.0,
0.0062,0.0,0.0062,0.0,0.0062,0.0,0.0048,0.0,
0.0041,0.0,0.0049,0.0,0.0049,0.0,0.0062,0.0,
0.0049,0.0,0.0062,0.0,0.0049,0.0,0.0049,0.0,
0.0062,0.0,0.0048,0.0,0.0041,0.0,0.0049,0.0,
0.0049,0.0,0.0062,0.0,0.0049,0.0,0.0062,0.0,
0.0049,0.0,0.0048,0.0,0.0049,0.0,0.0049,0.0,
0.0049,0.0,0.0049,0.0,0.0041,0.0,0.0049,0.0,
0.0049,0.0,0.0049,0.0,0.0049,0.0,0.0062,0.0,
0.0062,0.0,0.0062,0.0,0.0048,0.0,0.0041,0.0,
0.0049,0.0,0.0049,0.0,0.0048,0.0,0.0049,0.0,
0.0062,0.0,0.0049,0.0,0.0041,0.0,0.0049,0.0,
0.0049,0.0,0.0049,0.0,0.0049,0.0,0.0048,0.0,
0.0041,0.0,0.0049,0.0,0.0049,0.0,0.0048,0.0,
0.0041,0.0,
*************************************************************
drag,1,0,1,                    *drag1
0.15139,-0.18,0,94.0485,-1,0,          *drag2 (Cheng&Todreas coeff for bundles)
0.5,0.5921,                    *drag5
*************************************************************
grid,0,7,                                    *grid.1
9.4609,1.203,0.3751,21.089,182.049,305.,710.0,
98,10,                                      *grid.4
1,2,3,4,5,6,7,8,9,10,11,12,13,14,15,16,                  *grid.5
17,18,19,20,21,22,23,24,25,26,27,28,29,30,31,32,
33,34,35,36,37,38,39,40,41,42,43,44,45,46,47,48,
49,50,51,52,53,54,55,56,57,58,59,60,61,62,63,64,
65,66,67,68,69,70,71,72,                     *grid.5
**
0.0,4,7.3,1,19.008,2,39.02,2,59.039,2,79.488,2,99.504,2,119.520,2
139.469,2,160.748,3
0,
*************************************************************
axlv,          1,          1,          1    *axlv.1
*Channel flow area axial variations to account for PLFR
*NCI,NLEV
  6,   4   *axlv.2
*IMP
47,?
54,55,68,69,71
105.17, 1.0,?*axlv.4
105.20, 1.185,?
106.0, 1.185,?
164.517,1.185
  1,   4   *axlv.2
```

```
48,
*AXJ, AFACT
105.17, 1.0,?*axlv.4
105.20, 1.201,?
106.0, 1.201,?
164.517,1.201
0* terminates input for axlv.2-4
  6,    4   *axlv.2
*IMP
47,?
54,55,68,69,71
105.17, 1.0,?*axlv.4
105.20, 0.75,?
106.0, 0.75,?
164.517,0.75
  1,    4   *axlv.2
48,
*AXJ, AFACT
105.17, 1.0,?*axlv.4
105.20, 0.763,?
106.0, 0.763,?
164.517,0.763
0* terminates input for axlv.2-4
  6,    4   *axlv.3
*IMP
80,81,83,92,114,115,
105.17, 1.0,?*axlv.4
105.20, 2.39,?
106.0, 2.39,?
164.517,2.39
0* terminates input for axlv.2-4
*********************************************
 endd
*
*end of data input
0
```

G-2 CASMO-4 Input for the Large Assembly

```
TIT * MIT Large Assembly FUEL BUNDLE
***** STATE POINT PARAMETERS *****
TFU=821 TMO=560 VOI=45.1
MOD 0.7566
SIM 'GE11' 4.02 6. 44 44
***** OPERATING PARAMETERS *****
***** MATERIAL COMPOSITIONS *****
MI1 0.7912/1001=11.19 8000=88.81
* Effective moderator density within water rods
FUE 1 10.4/4.6
FUE 2 10.1/4.0 64016=6.
FUE 3 10.4/2.65
FUE 4 10.4/3.15
FUE 5 10.4/4.0
FUE 6 10.4/3.75
LFU
0
1 1
1 1 2
0 1 1 0
0 2 5 0 0
5 1 1 5 5 6
1 1 2 5 6 6 0
0 5 5 0 0 4 0 0
0 2 5 0 0 5 5 5 1
5 5 2 6 6 6 5 2 5 4
5 5 5 6 6 6 5 5 6 4 3
***** GEOMETRY SPECIFICATION *****
BWR 22 1.3053 28.972 0.254 0.5 0.5 1.3 8/0.3
PIN 1 0.4145 0.423 0.48 * Fuel rod
PIN 2 1.2202 1.30/'MI1' 'BOX'//4.0 * Water rod
* modified for 1.2818 1.358
LPI
2
1 1
1 1 1
2 1 1 2
2 1 1 2 2
1 1 1 1 1 1
1 1 1 1 1 1 2
2 1 1 2 2 1 2 2
2 1 1 2 2 1 1 1 1
1 1 1 1 1 1 1 1 1 1
1 1 1 1 1 1 1 1 1 1 1
DEP -16.58 -33.16 -49.75
```

```
PDE 60.6 'KWL'
STA
END
```

G-3 MCODE Input for 3D Burnup Calculation of the Large Assembly

```
$ TITLE line
TTL Large Assembly (One assembly Model)
$ CTRL command initial-inp
MCD 1 /home/karahan/bin/mcnp.exe b1.inp srctp1
$ ORIGEN-COMMAND ORIGEN-LIBRARY-PATH decay-lib gammalib
ORG /usr/local/bin/origen22/origen22 /usr/local/bin/origen22/LIBS DECAY.LIB
GXUO2BRM.LIB
$ total# CELL-ID TYPE IHM(g) VOL(cm3) ORG-XS-LIB
CEL 92 2000 99 27979.576 3052.007 BWRUE.LIB
     2001 8 37367.460 4076.035 BWRUE.LIB
     2002 98 13272.881 1447.803 BWRUE.LIB
     2003 89 13272.881 1447.803 BWRUE.LIB
     2004 80 13272.881 1447.803 BWRUE.LIB
     2005 71 13272.881 1447.803 BWRUE.LIB
     2006 62 13272.881 1447.803 BWRUE.LIB
     2007 53 13272.881 1447.803 BWRUE.LIB
     2008 44 10857.128 1184.293 BWRUE.LIB
     2009 35 15688.577 1711.307 BWRUE.LIB
     2010 26 13272.881 1447.803 BWRUE.LIB
     2011 17 13272.881 1447.803 BWRUE.LIB
     2012 93 663.644 72.3902  BWRUE.LIB
     2013 84 663.644 72.3902  BWRUE.LIB
     2014 75 663.644 72.3902 BWRUE.LIB
     2015 66 663.644 72.3902 BWRUE.LIB
     2016 57 663.644 72.3902 BWRUE.LIB
     2017 48 663.644 72.3902 BWRUE.LIB
     2018 39 542.856 59.2147 BWRUE.LIB
     2019 30 784.429 85.5653 BWRUE.LIB
     2020 21 663.644 72.3902 BWRUE.LIB
     2021 12 663.644 72.3902 BWRUE.LIB
     2022 92 3318.220 361.951 BWRUE.LIB
     2023 83 3318.220 361.951 BWRUE.LIB
     2024 74 3318.220 361.951 BWRUE.LIB
     2025 65 3318.220 361.951 BWRUE.LIB
     2026 56 3318.220 361.951 BWRUE.LIB
     2027 47 3318.220 361.951 BWRUE.LIB
     2028 38 2714.282 296.073 BWRUE.LIB
     2029 29 3137.715 342.261 BWRUE.LIB
     2030 20 2654.576 289.561 BWRUE.LIB
     2031 11 2654.576 289.561 BWRUE.LIB
     2032 91 26545.758 2895.606 BWRUE.LIB
     2033 82 26545.758 2895.606 BWRUE.LIB
     2034 73 26545.758 2895.606 BWRUE.LIB
     2035 64 26545.758 2895.606 BWRUE.LIB
     2036 55 26545.758 2895.606 BWRUE.LIB
```

```
2037 46 26545.758 2895.606 BWRUE.LIB
2038 37 21714.257 2368.587 BWRUE.LIB
2039 28 31377.155 3422.614 BWRUE.LIB
2040 19 26545.758 2895.606 BWRUE.LIB
2041 10 26545.758 2895.606 BWRUE.LIB
2042 90 12609.237 1375.413 BWRUE.LIB
2043 81 12609.237 1375.413 BWRUE.LIB
2044 72 12609.237 1375.413 BWRUE.LIB
2045 63 12609.237 1375.413 BWRUE.LIB
2046 54 12609.237 1375.413 BWRUE.LIB
2047 45 12609.237 1375.413 BWRUE.LIB
2048 36 10314.274 1125.079 BWRUE.LIB
2049 27 13335.291 1454.611 BWRUE.LIB
2050 18 11281.948 1230.633 BWRUE.LIB
2051 9 11281.948 1230.633 BWRUE.LIB
2052 97 1666.041 199.0729 BWRUE.LIB
2053 96 1666.041 199.0729 BWRUE.LIB
2054 95 1666.041 199.0729 BWRUE.LIB
2055 94 1666.041 199.0729 BWRUE.LIB
2056 88 1666.041 199.0729 BWRUE.LIB
2057 87 1666.041 199.0729 BWRUE.LIB
2058 86 1666.041 199.0729 BWRUE.LIB
2059 85 1666.041 199.0729 BWRUE.LIB
2060 79 1666.041 199.0729 BWRUE.LIB
2061 78 1666.041 199.0729 BWRUE.LIB
2062 77 1666.041 199.0729 BWRUE.LIB
2063 76 1666.041 199.0729 BWRUE.LIB
2064 70 1666.041 199.0729 BWRUE.LIB
2065 69 1666.041 199.0729 BWRUE.LIB
2066 68 1666.041 199.0729 BWRUE.LIB
2067 67 1666.041 199.0729 BWRUE.LIB
2068 61 1666.041 199.0729 BWRUE.LIB
2069 60 1666.041 199.0729 BWRUE.LIB
2070 59 1666.041 199.0729 BWRUE.LIB
2071 58 1666.041 199.0729 BWRUE.LIB
2072 52 1666.041 199.0729 BWRUE.LIB
2073 51 1666.041 199.0729 BWRUE.LIB
2074 50 1666.041 199.0729 BWRUE.LIB
2075 49 1666.041 199.0729 BWRUE.LIB
2076 43 1362.811 162.840 BWRUE.LIB
2077 42 1362.811 162.840 BWRUE.LIB
2078 41 1362.811 162.840 BWRUE.LIB
2079 40 1362.811 162.840 BWRUE.LIB
2080 34 1969.268 235.305 BWRUE.LIB
2081 33 1969.268 235.305 BWRUE.LIB
2082 32 1969.268 235.305 BWRUE.LIB
2083 31 1969.268 235.305 BWRUE.LIB
2084 25 1666.041 199.0729 BWRUE.LIB
```

```
    2085 24 1666.041 199.0729 BWRUE.LIB
    2086 23 1666.041 199.0729 BWRUE.LIB
    2087 22 1666.041 199.0729 BWRUE.LIB
    2088 16 1666.041 199.0729 BWRUE.LIB
    2089 15 1666.041 199.0729 BWRUE.LIB
    2090 14 1666.041 199.0729 BWRUE.LIB
    2091 13 1666.041 199.0729 BWRUE.LIB
$ TOTAL VOLUME (cm3)
VOL 344474.4388
$ power density, opt: WGU=W/gIHM, KWL=kW/(liter core)
PDE 60.6 KWL
$ NORMALIZATION option, 1=FLUX, 2=POWER
NOR 2
$ Predictor-Corrector option, 1=ON, 0=OFF
COR 0
$ opt E=MWd/kg, D=EFPD
$ 1 2 3 4 5 6 7 8 10 12 14 15 16 17 18 19 20 21 22 23 24 24 25 26
DEP E 0 0.1 1.0 2.0 3.0 4.0 6.0 8.0 10.0 12.0 14.0 15 16.58 18.0 20.0 22 24 26 28 30 32 33.17
36.0 39.0 42.0 45.0 48.0 49.75
NMD 3 20 20 20 20 20 20 20 20 20 20 20 20 20 20 20 20 20 20 20 20 20 20 20 20 20 20 20
STA 0 $ starting point
END 27 $ ending point
```

G-4 In-phase Stability Input for the Large Assembly

Stability code consists of many files. Only the main input file is given below.

```
%Matlab script for calculating the Decay Ratios of the BWR in-phase stability
%
%%%%%%%%%%%%%%%%%% Beginning of the input file

%water properties at the saturation state
P=7.136*1.0e6;%Pa, system pressure
vf=0.00135629; %kg/m^3, liquid specific volume
vg=0.0267941; %kg/m^3, vapor sepcific volume
hf=1274.63;%KJ/kg, liquid specific enthalpy
hg=2770.84;%KJ/kg, vapor specific enthalpy
Cpf=5.42992;%kJ/kg, liquid specific heat
kf=569.741e-3;%J/kg, liquid heat conductivity
Prf=0.864884;% liquid Prandtl number
dviscf=0.0000907488; % liquid dynamic viscocity
dviscg=0.00001902;% vapor dynamic viscocity
xigmaf=0.0173297;%N/m surface tension
Tf=560.2;%K, saturation temperature

%assembly and fuel variables
d_pin=0.0096;%m, pin diameter
d_pellet=0.829e-2;%m, pellet diameter
N_assm=191;%total assembly number
N_pin=384;% number of the pins per assembly
L=3.70789;%m, active length of the core
L_tot=4.178706;%m, total length of the core
d_assm=0.28972;%m, assembly inner side
hgap=5.661;%kW/m^2-K, gap gas conductance
denfuel=10421*0.95;%kg/m^3, fuel density,95% of the theoretical density

%core power and flow
Qcore=3987.6e3;%kW
mcore=16442.04;%kg/s, core flow rate
%feedwater
mfw=2226.605;%feedwater flow rate
hfw=975.6;

%1. Core channel groups parameters
%high power channel group parameters
kin_h=21.089;%high power channel group inlet orifice
assem_h=37;%high power channel group assembly number
mhigh=75.9866; %kg/s, high power channel group flow rate per assembly
Fpr_h=1.3;%high power channel factor relative to the core average power
```

```
%middle power channel parameters
kin_m=21.089;
assem_m=125;
m_m=81.2120;
Fpr_m=1.004;%middle power channel factor relative to the core average power

%low power channel parameters
kin_l=214.0;
assem_l=29;
mlow=40.5914;
Fpr_l=0.6;%low power channel factor relative to the core average power
%%%%%%End of Channel groups parameters

%2.upper plenum
Aup_ex=3.9328;%upper plenum exit area equals riser area
Aup=17.709;%upper plenum area
Lup=1.524;%length

%3.riser
De_rs=0.15405;%m, riser equivalent diameter
A_rs=3.9328;%riser area equals the exit of upper plenum
L_rs=2.718;

%4. steam separator
De_sep=0.2267;%m, equivalent diameter of the steam separator
L_sep=2.266;
A_sep=8.5164;%m^2, flow area
Ksep=5.3232;%equivalent loss coefficient of the steam separator for a typical BWR

%5. downcomer parameters
%RPV parameters
Drpv=6.375;%m, inside diameter of RPV
Trpv=0.16;%m, RPV wall thickness
denv=7.8e3;%kg/m^3, density of the RPV wall
Cpv=0.58;%kJ/kg, Specific heat of the RPV wall

%first part Downcomer parameters
Ldc1=2.1980;
Adc1=22.176;
De_dc1=0.6433;

%Second part Downcomer parameters
Ldc2=1.5943;
Adc2=8.551;
De_dc2=0.8508;

%jet pump part Downcomer parameters
```

```
Mra=1.96;%M ratio of the recirculation loop
Njet=20;%number of the jet pump
Asuction_jet=0.04;%suction flow area per jet pump
Ksuction=0.35;%suction loss coefficient
Athroat_jet=0.0354;%m^2, throat area per jet pump
Lthroat=2.5766;%m, throat length
De_throat=0.21224;%equivalent diameter of throat
Dediff1_in=0.21224;%upper part diffuser inlet diameter
Dediff1_out=0.2535;%upper part diffuser outlet diameter
Ldiff1=0.3053;%upper part diffuser length
Dediff2_in=0.2535;%low part diffuser inlet diameter
Dediff2_out=0.4826;
Ldiff2=1.8865;
Adis_jet=0.183;%m^2, discharge part area per jet pump
Ldis=0.2432;%discharge part length
De_dis=0.4826;%equivalent diameter of discharge part
Kdis=1.0;%form loss coefficient of discharge part


%%%%%%%%%%neutronic parameters
Ctem=-2.3e-5;%temperature coefficient
Cvoid1=-0.143;%coefficient in quadratic void coefficient calculation
Cvoid2=0.12005;
Cvoid3=-0.1755;

T_neu=2.3e-5;%time constant

betaf=0.0067;% six groups delayed neutron fraction
betaf1=betaf*0.033;
betaf2=betaf*0.219;
betaf3=betaf*0.196;
betaf4=betaf*0.395;
betaf5=betaf*0.115;
betaf6=betaf*0.042;
lamdaf1=0.0124;% six groups decay constant
lamdaf2=0.0305;
lamdaf3=0.111;
lamdaf4=0.301;
lamdaf5=1.14;
lamdaf6=3.01;
%%%%%%%%end of neutronics variables value assignment
%inlet conditions
hin=1227.55;%kJ/kg, inlet enthalpy
Tin=551.45;%K, inlet temperature
%input the initial guess of the dominate root
root_re=-1.0;
root_im=5.5;
%%%%%%%%%%%%%%%end of the input file
```

G-5 FRAPCON-3 Input for the Large Assembly Rod

```
* GOESINS:
FILE05='nullfile', STATUS='UNKNOWN', FORM='FORMATTED',
         CARRIAGE CONTROL='NONE'
*
* GOESOUTS:
FILE06='outgeA1',    STATUS='UNKNOWN', CARRIAGE CONTROL='LIST'
FILE66='stripf.gea', STATUS='UNKNOWN', FORM='FORMATTED',
        CARRIAGE CONTROL='LIST'
/**************************************************************************
    Large Assembly Rod
 $frpcn
    im=68,      na=12,      nr=17,
    ngasr = 15,
 $end
 $frpcon
    cpl = 11.24, crdt = 0.0, thkcld = 0.0224, thkgap = 0.0033,
    dco = 0.378, pitch = 0.5139,
    den = 95., dspg = 0.332,fa = 1.,
    dspgw = 0.04, enrch = 4.02, fgpav = 43.51, hdish = 0.0,
    hplt = 0.5, icm = 2,
    icor = 2, idxgas = 1, iplant =-3, iq = 0, jdlpr = 0,
    totl = 12.17, roughc = 1.97e-5, roughf = 8.3e-5, vs = 100.0,
    nunits = 1, rsntr = 150.,
    imox=0, nplot=1,
    p2(1) = 1035.0, tw(1) = 533, go(1) = 13.102e5,
    flux=   1.95e16,1.95e16,2.20e16,2.40e16,2.50e16,2.60e16,2.80e16,
            2.95e16,3.08e16,3.17e16,3.21e16,3.15e16,2.95e16,
    jn = 26,
    jst =   68*1,
    qf(1) = 0.8059,0.8288,0.8723,0.9124,0.9489,0.9818,1.0108,1.0359,1.057,
            1.0739,1.0866,1.0952,1.099,1.099,1.095,1.0866,1.0738,1.057,
            1.0359,1.0107,0.9818,0.9489,0.9124,0.8723,0.8288,0.8059,
    x(1) =  0.00,0.25,0.76,1.27,1.77,2.28,2.79,3.30,3.80,4.31,4.82,5.32,5.83,
       6.34,6.84,7.35,7.86,8.36,8.87,9.38,9.88,10.39,10.90,11.41,11.91,12.17,
    ProblemTime =  5.484, 10.869, 26.165, 44.025, 60.09, 88.556, 99.584, 108.59,
                  121.21, 125.44, 144.8, 168.36, 186.89, 204.57, 220.56, 279.46,
                  309.79, 340.08, 372.92, 409.1, 425.95, 462.52, 481.52, 507.62,
                  540.42, 566.52, 598.5, 625.46, 647.33, 673.4, 817.37, 840.93,
                  850.21, 867.89, 901.56, 911.66, 933.55, 955.43, 973.94, 1010.28,
                  1033.73, 1052.23, 1071.59, 1092.6, 1113.68, 1136.41, 1157.46,
                  1176.82, 1195.35, 1205.46, 1214.71, 1226.51, 1289.64, 1293.01,
                  1311.51, 1333.41, 1348.54, 1370.45, 1391.49, 1407.48, 1427.7,
                  1438.64, 1476.5, 1514.4, 1552.29, 1590.1, 1628.0, 1643.6,
    qmpy =  6.762, 6.747, 6.705, 6.656, 6.611, 6.533, 6.503, 6.478, 6.444,
            6.432, 6.379, 6.314, 6.263, 6.214, 6.170, 6.009, 5.925, 5.842, 5.752,
            5.652, 5.606, 5.505, 5.453, 5.382, 5.291, 5.219, 5.132, 5.058, 4.998,
            4.926, 4.530, 4.465, 4.440, 4.391, 4.299, 4.271, 4.211, 4.150, 4.099,
            4.000, 3.935, 3.884, 3.831, 3.773, 3.715, 3.653, 3.595, 3.542, 3.491,
            3.463, 3.438, 3.405, 3.232, 3.223, 3.172, 3.111, 3.070, 3.010, 2.952,
            2.908, 2.853, 2.822, 2.718, 2.614, 2.510, 2.406, 2.302, 2.259,
    slim = .05,
 $end
```

References

1. C. Brown, K. Hartley and J. Hulsman, "Extended Power Uprates and 2-yr Cycles For BWRs—Where Do We Go From Here?," Nuclear Technology, Volume 151, 2005.

2. "Licensing Topical Report Constant Pressure Power Uprate," GE Nuclear Energy, NEDO-33004 Rev. 3, 2003.

3. R. T. Lahey and F. J. Moody, "The Thermal-hydraulics of a Boiling Water Nuclear Reactor", American Nuclear Society, 1993.

4. M. Ruddick, "An Experimental investigation of the Heat Transfer at High Rates between a Tube and Water with Conditions at or Neat Boiling," Ph.D. Thesis, University of London, 1953.

5. J. M. Cuta, et al., "VIPRE-01 A Thermal-Hydraulic Code for reactor Cores," Volumes 1-3, EPRI, NP-2511CCM, 1985.

6. J. Zhao, et al., "Stability Analysis of Supercritical Water Cooled Reactors," Ph.D. Thesis, The Department of Nuclear Science and Engineering, Massachusetts Institute of Technology, MIT-ANP-TR-108, 2005.

7. D. Knott, B. H. Forssen and M. Edenius, "CASMO-4, A Fuel Assembly Burnup Program, Methodology," Studsvik/SOA-95/2, Studsvik of America, Inc., 1995.

8. J. F. Briesmeister (Editor), "MCNP--A general Monte Carlo N-particle transport code," Los Alamos National Laboratory Report LA-12625-M, Los Alamos, NM, 1993.

9. A. G. Croff, "A User's Manual for the ORIGEN2 Computer Code," ORNL/TM-7175, Oak Ridge National Laboratory, July 1980.

10. Z. Hu, "Design Strategies for Optimizing High Burnup Fuel in Pressurized Water Reactors," Ph. D. Thesis, Department of Nuclear Science and Engineering, Massachusetts Institute of Technology, 2003.

11. G. A. Berna, et. al, "FRAPCON-3 : A Computer Code for the Calculation of Steady State, Thermal-Mechanical Behavior of Oxide Fuel Rods for High Burnup, Volume 2," NUREG/CR-6534, PNNL-11513, prepared for the U.S. Nuclear Regulatory Commission by Pacific Northwest Laboratory, Richland, Washington, 1997.

12. Y. Long, "Modeling the Performance of High Burnup Thoria and Urania PWR Fuel," Ph.D. Thesis, Department of Nuclear Science of Engineering, Massachusetts Institute of Technology, 2002.

13. Nine Mile Point Unit 2, Updated Safety Analysis Report (USAR), Rev.16, October 2004.

14. P. Ferroni and N. E. Todreas, "Steady State Thermal Hydraulic Analysis of Hydride Fueled BWRs," Center of Advanced Nuclear Engineering Systems (CANES), MIT-NFC-PR-079, May, 2006.

15. M. Fratoni, "Burnable Poisons in Hydride Fuel Core," University of California Berkeley, Internal Report, November, 2005.

16. J. Zhao, H. C. No and M. S. Kazimi, "Mechanical Analysis of High Power Internally Cooled Annular Fuel," Journal of Nuclear Technology, Volume 146, American Nuclear Society, May, 2004.

17. A. Preumont, "On the Vibrational Behavior of Pressurized Water Reactor Fuel Rods," Nuclear Technology, Volume 58, September, 1982.

18. M. J. Driscoll, T. J. Downer and E. E. Pilat, "The Linear Reactivity Model for Nuclear Fuel Management," American Nuclear Society, 1990.

19. S. M. Bowman and O. W. Hermann, "Scale-4 Analysis of Pressurized Water Reactor Critical Configurations: Volume 3-Surry Unit 1 Cycle 2," ORNL/TM-12294/V3, USA, 1995.

20. J. Duderstadt and L. J. Hamilton, "Nuclear Reactor Analysis," John Wiley & Sons, 1976.

21. K. Une, M. Imamura, M. Amaya, Y, Koeri, "Fuel Oxidation and Irradiation Behaviors of Defective BWR Fuel Rods," Journal of Nuclear Materials, Volume 223, Page 40-50, 1995.

22. Http://www.pnl.gov/frapcon3/

23. V. N. Shah and P. E. Macdonald, "Aging and Life Extension of Major Light Water Reactor Components," Elsevier, 1993.

24. K. Park, B. Kang, K. Song and G. Park, "Design of a Spacer Grid Using Axiomatic Design," Journal of Nuclear Science and Technology, Volume 40, December, 2003.

25. G. Dooley, DCS SYSTEMS INC., Personal Communication to Prof. Jacopo Buongiorno, NOVEMBER 8, 2006.

26. M. Moriwaki, M. Chaki, M. Aoyama, H. Okada, H. Kitamura and K. Hiraiwa, "Large Bundle Design and its Development for ABWR-II," Proceedings of ICAPP'04, Paper 4069, 2004.

27. IAEA TECDOC-1391, "Status of Advanced Light Water Designs 2004," International Atomic Energy Agency, 2004.

28. M. Chaki, H. Soneda, S. Mizokami, H. Kitamura, K. Hiraiwa, T. Fukahori, J. G. Andersen, "Evaluation of Stability and Transient Characteristics of ABWR-II Large Bundle Core and SSR Influence for Transient Phenomena by TRACG Code," Proceedings of ICAPP'04, Paper 4050, 2004.

29. M. Kimatura, et al., "BWR 9×9 Type Fuel Assembly Critical Power Tests at High-Pressure Conditions," 6th International Conference on Nuclear Engineering ICONE, Paper 6410, May, 1998.

30. Rui Hu, Department of Nuclear Science and Engineering, Massachusetts Institute of Technology, Personal Communication to Aydın Karahan, November, 2006.

31. L. S. Tong, and Y. S. Tang, "Boiling Heat Transfer and Two Phase Flow," Taylor and Francis, 1997.

32. N. E. Todreas and M. S. Kazimi, "Nuclear Systems II, Elements of Thermalhydraulic Design," Taylor and Francis, 1990.